NASA/CP—2004-213207

2004 Photon Correlation and Scattering Conference

August 2004

The NASA STI Program Office . . . in Profile

Since its founding, NASA has been dedicated to the advancement of aeronautics and space science. The NASA Scientific and Technical Information (STI) Program Office plays a key part in helping NASA maintain this important role.

The NASA STI Program Office is operated by Langley Research Center, the Lead Center for NASA's scientific and technical information. The NASA STI Program Office provides access to the NASA STI Database, the largest collection of aeronautical and space science STI in the world. The Program Office is also NASA's institutional mechanism for disseminating the results of its research and development activities. These results are published by NASA in the NASA STI Report Series, which includes the following report types:

- TECHNICAL PUBLICATION. Reports of completed research or a major significant phase of research that present the results of NASA programs and include extensive data or theoretical analysis. Includes compilations of significant scientific and technical data and information deemed to be of continuing reference value. NASA's counterpart of peer-reviewed formal professional papers but has less stringent limitations on manuscript length and extent of graphic presentations.

- TECHNICAL MEMORANDUM. Scientific and technical findings that are preliminary or of specialized interest, e.g., quick release reports, working papers, and bibliographies that contain minimal annotation. Does not contain extensive analysis.

- CONTRACTOR REPORT. Scientific and technical findings by NASA-sponsored contractors and grantees.

- CONFERENCE PUBLICATION. Collected papers from scientific and technical conferences, symposia, seminars, or other meetings sponsored or cosponsored by NASA.

- SPECIAL PUBLICATION. Scientific, technical, or historical information from NASA programs, projects, and missions, often concerned with subjects having substantial public interest.

- TECHNICAL TRANSLATION. English-language translations of foreign scientific and technical material pertinent to NASA's mission.

Specialized services that complement the STI Program Office's diverse offerings include creating custom thesauri, building customized databases, organizing and publishing research results . . . even providing videos.

For more information about the NASA STI Program Office, see the following:

- Access the NASA STI Program Home Page at ***http://www.sti.nasa.gov***

- E-mail your question via the Internet to help@sti.nasa.gov

- Fax your question to the NASA Access Help Desk at 301–621–0134

- Telephone the NASA Access Help Desk at 301–621–0390

- Write to:
  NASA Access Help Desk
  NASA Center for AeroSpace Information
  7121 Standard Drive
  Hanover, MD 21076

NASA/CP—2004-213207

2004 Photon Correlation and Scattering Conference

Proceedings of the 2004 Photon Correlation and Scattering Conference
cosponsored by ESA, OSA, NASA Glenn Research Center, NCMR,
the University of Amsterdam, and the Van der Waals-Zeeman Institute
Amsterdam, The Netherlands
August 16–18, 2004

National Aeronautics and
Space Administration

Glenn Research Center

August 2004

Acknowledgments

Conference Chairs

Aristide Dogariu, University of Central Florida/CREOL, U.S.A., Chair
William Meyer, NCMR/NASA Glenn Research Center, U.S.A., Chair
Anthony Smart, U.S.A., Chair
Gerard Wegdam, University of Amsterdam, The Netherlands, Chair

Technical Program Committee

Mikhail Anisimov, University of Maryland, U.S.A.
Robert Brown, Queens University, Belfast, U.K.
David Cannell, University of California at Santa Barbara, U.S.A.
Paul Chaikin, Princeton University, U.S.A.
Jan Dhont, IFF Institute, Germany
Barbara Frisken, Simon Fraser University, Canada
Marzio Giglio, University di Milano, Italy
Dominique Langevin, Laboratoire de Physique des Solides, France
J. Adin Mann, Case Western Reserve University, U.S.A.
Roberto Piazza, Politecnico di Milano, Italy
E. Roy Pike, King's College, London, U.K.
Raj Rajagopalan, National University of Singapore
David Weitz, Harvard University, U.S.A.
Simone Wiegand, IFF Institute: Soft Matter, Germany

Available from

NASA Center for Aerospace Information
7121 Standard Drive
Hanover, MD 21076

National Technical Information Service
5285 Port Royal Road
Springfield, VA 22100

Available electronically at http://gltrs.grc.nasa.gov

Table of Contents

Monday, August 16, 2004

Session 1 (Chair: Gerard Wegdam)
9:00 a.m.

Introduction and Colloidal Systems

MA1 9:00 Conference Opening Plenary Address: Colloids, Candies, DNA: Packing, Pushing, and Pasting
Paul Chaikin (Invited), U.S.A.

With an aim toward colloidal architecture of dynamic microstructures, we have fabricated non-spherical colloids, modeled their packing properties with M&M's, manipulated them with AC electric fields and laser tweezers, and reversibly stuck them together with DNA.

MA2 9:50 Nano-photonics for novel photon correlation technologies
Robert G.W. Brown (Invited), U.K.

We consider recent progress in nano-photonics/ electronics, looking at how it might be used to generate new technologies for photon correlation and scattering: nano-lasers, nano-optical-fibers, nano-detectors, nano-transistors, nano-memories, nano-computers and quantum-computers, perhaps even nano-photon-correlators.

10:20 Coffee and Exhibition

Session 2 (Chair: Jan Dhont)
10:40 a.m.

Colloidal Systems

MB1 10:40 Avalanche behavior in yield stress fluids
Daniel Bonn (Invited), France

We show that above a critical stress, typical yield stress fluids (gels, clay suspensions) and soft glassy materials (the colloidal glass of Laponite) start flowing abruptly and subsequently accelerate, leading to avalanches that are remarkably similar to those of granular materials. Rheometrical tests reveal that this is associated to a bifurcation in rheological behavior: for small stresses, the viscosity increases in time: the material "ages", and eventually stops flowing. For slightly larger stresses the viscosity decreases continuously in time: the flow accelerates and we observe a "rejuvenation" of the material by the flow. We show that for the Laponite system, both the aging and the shear rejuvenation can be observed directly using Photon Correlation Spectroscopy and Diffusive Wave Spectroscopy. We propose a simple physical model capable of reproducing the rheological observations.

MB2 11:10 Aging dynamics of translational and rotational diffusion in a colloidal glass
S. Jabbari-Farouji, E. Eiser, G. Wegdam, and D. Bonn, The Netherlands

We study the dynamics of translational and rotational diffusion during the aging of the colloidal glass of Laponite using polarized and depolarized dynamic light scattering. The dynamics are qualitatively very similar between the two degrees of freedom. The short-time diffusion is independent of the time elapsed since the sample preparation. The intermediate- and long-time diffusion, on the other hand, changes over several orders of magnitude during the aging, the slowing down of the rotational diffusion being much faster than that of the translational diffusion.

MB3 11:30 Shadowgraphic study of convection onset in a colloidal suspension
R. Cerino, S. Mazzoni, A. Vailati, and M. Giglio, Italy

A shadowgraph optical setup is used to study the time evolution of Soret induced convection in a colloidal suspension. We obtain a scale invariant behavior for the solutal Nusselt number as a function of the Rayleigh number.

MB4 11:50 Reentrant melting of colloidal hard spheres near a wall
Roel P.A. Dullens and Willem K. Kegel (Invited), The Netherlands

Concentrated suspensions of colloidal hard spheres near a hard wall were studied in real space by means of time-resolved confocal scanning laser microscopy. Both structure and dynamics of these systems are dramatically different from their bulk analogues (i.e., far away from a wall). In particular, systems that are a glass (a solid phase without long range positional order) in the bulk show significant hexagonal order near a wall. The hexagonal order is observed to first increase with volume fraction of the colloids, reach a constant value, and subsequently decrease. When hexagonal order decreases, the mobility of the particles starts increasing with volume fraction. These observations are consistent with a reentrant melting transition. However, the behavior of static correlation functions indicate that the in-plane structure near a wall is hexatic rather than crystalline, reflecting the two-dimensional character of dense matter near walls.

12:20 Catered Lunch and Exhibition

PCS Revealed: A Session for Accompanying Guests

Session 3 (Chair: Dave Weitz)
13:50 p.m.

Colloidal Systems

MC1 13:50 DLS and FCS on tracer spheres in concentrated rod dispersions
K. Kang, J. Gapinski, M.P. Lettinga, J. Buitenhuis, G. Meier, Jan K.G. Dhont (Invited), and A. Patkowski, Germany, Poland

Diffusion of tracer spheres in dispersions of rods is measured by dynamic light scattering (DLS) and fluorescence correlation spectroscopy (FCS), as a function of the rod concentration and the size ratio of the sphere to the rod. By comparing with DLS, FCS is shown to measure long-time diffusion only for relatively small spheres. A variational approach for the prediction of long-time self-diffusion coefficients is compared with experiments.

MC2 14:20 Effect of electrolyte concentration on the hydrodynamic radius of polymer lattices as measured with PCS
Carlos A. Rega and Robert O. Jack, U.K.

In this paper we study the effect of electrolyte concentration on the hydrodynamic radius of polymer latex particles using PCS. Our measurements show that the concentration of electrolyte on the surface charge of the particles has a significant effect on the particle size as measured using PCS.

MC3 14:40 Physics of photonic crystals: Of dreams and nightmares
Willem Vos (Invited) and Ad Lagendijk, The Netherlands

We present first evidence that photonic crystals control emission rates of embedded light sources. We analyze intrinsic disorder in two- and three-dimensional crystals and conclude that applications, especially integrated circuits, have a dim future.

15:10 Coffee and Exhibition

Session 4 (Chair: Paul Chaikin)
15:30 p.m.

Colloidal Systems

MD1 15:30 Multiple light scattering probes of fluid and solid soft materials
Frank Scheffold (Invited), Switzerland

We report on recent advances in single and multi-speckle Diffusing Waves Spectroscopy (DWS). Special emphasis is given to slowly relaxing or completely arrested systems, such as gels and glasses. For such systems, the speckle time and ensemble average of multiple scattering light are different on the timescale of a typical experiment. New developments in photon correlation spectroscopy nowadays provide efficient routes to overcome these nonergodicity problems in DWS. Here we report on the application of multispeckle DWS, spatial averaging schemes in PCS and two cell DWS (TCDWS). Based on a combination of single- and multispeckle detection schemes, it is now possible to cover "in a single shot" relaxation times from a few nanoseconds to minutes or hours. In DWS microrheology experiments, the accessible elastic properties of viscoelastic fluid or solid materials range roughly from below 1 Pa to several 100 kPa. Typical application examples are briefly discussed such as DWS from colloid and biopolymer gels and microrheology of dense surfactant solutions.

MD2 16:00 Scattering probes of the growth and elasticity of colloidal gels
David A. Weitz (Invited), U.S.A.

Dynamic light scattering is used to determine the elasticity of colloidal gels. Comparison of microgravity and Earth based data suggest new aging mechanisms. The gelation process can exhibit hallmarks of the glass transition.

17:15 Van der Waals-Zeeman, Laboratory tour departure

19:00 Conference dinner at the Artis Zoo in Amsterdam, which is within walking distance of the conference location at the Royal Academy

Tuesday, August 17, 2004

Session 5 (Chair: Marzio Giglio) 9:00 a.m.

Near Field Scattering

TuA1 9:00 Statistics of optical near-fields
A. Apostol and A. Dogariu (Invited), U.S.A.

We show that the joint probability distribution of polarization information and the complex degree of mutual polarization can be used to differentiate between different highly scattering media, which depolarize the light in a global sense.

TuA2 9:30 Near field scattering
Marco A.C. Potenza, Doriano Brogioli, Alberto Vailati, and Marzio Giglio, Italy

We present a novel scattering technique based on the statistical analysis of the random intensity distribution in the near field of the light scattered by a sample.

TuA3 9:50 Mechanism of giant enhancement of hyper-Rayleigh scattering in silver nanostructures
E.M. Kim, S.S. Elovikov, D.A. Muzychenko, and O.A. Aktsipetrov, Russia

Hyper-Rayleigh scattering in optical second harmonic generation was experimentally observed in silver island films. A combined analysis of the nonlinear scattering patterns in combination with the analysis of the results of atomic-force microscopy revealed the fractal nature of the films. Mechanism of giant enhancement in ultra- dispersed metal systems was observed with the help of dielectric wedge coating a semiconductor substrate layer.

TuA4 10:10 Giant third-harmonic generation in silver nanoparticles: New type of hyper-Rayleigh scattering
O.A. Aktsipetrov, S.S. Elovikov, E.M. Kim, M.A. Bader, and G. Marowsky, Russia

Surface-enhanced third-harmonic generation (THG) is observed in silver island films. THG intensity is enhanced by two orders of magnitude and the enhancement is attributed to the resonant local surface plasmon excitation. Diffuse and depolarized THG is associated with third-order hyper-Rayleigh scattering in random ensemble of silver nanoparticles.

TuA5 10:30 A near-field microwave microscope and electron spin resonance detection
J. Adin Mann and Massood Tabib-Azar, U.S.A.

Microwave photons can image a surface using near-field geometry. Spatial resolution is on the nanometer length scale. Moreover, it is possible to detect electron spin resonance splitting caused by a small permanent magnet positioned close to the surface containing a free radical moiety.

10:50 Coffee Break and Exhibition

Session 6 (Chair: Anthony Smart) 11:10 a.m.

Fluctuations in Fluids

TuB1 11:10 Smectic membranes in motion: The limits of x-ray photon correlation spectroscopy
Wim H. de Jeu (Invited), The Netherlands

In the first part, I shall summarize results we reported recently of low-dimensional fluctuations in smectic liquid crystal membranes in the range of 10 ns to 10 ms using both x-ray photon correlation spectroscopy (XPCS) and neutron spin echo (NSE). XPCS probes surface tension-dominated relaxation times. In this regime, fluctuations with long wavelengths reveal an oscillatory damping, while fluctuations with a shorter wavelength show a simple exponential decay. NSE reveals a new regime determined by bulk elasticity, in which the fast relaxation times decrease with the wave vector.

In the second part, I will discuss several practical aspects and limitations we encountered during our XPCS studies. Coherence effects differ from the situation in classical dynamic light scattering and can influence the time dependence of the correlation function. Variation of the detector slits as well as the variation of the projected coherence length on the membrane induces a change in the correlation time. Finally heterodyne detection occurring at the specular ridge and homodyne detection at off-specular positions, will be discussed.

Wednesday, August 18, 2004

Session 7 (Chair: Aristide Dogariu) 9:00 a.m.

Photon Scattering

WA1 9:00 Correlation spectroscopy with coherent x-rays
Gehard Grubel (Invited), Germany

X-ray photon correlation spectroscopy (XPCS) is a novel technique for the study of slow dynamics in disordered materials. It overcomes limitations of visible light scattering techniques such as multiple scattering or limitations in Q-range by using coherent x-ray from third generation synchrotron radiation sources. Applications to the static and dynamic behavior of complex fluids and to slow dynamics in hard condensed matter systems are reviewed.

WA2 9:30 Using diffusing-wave spectroscopy to study intermittent dynamics
Régis Sarcia and Pascal Herbraud, France

A new scheme of diffusing-wave spectroscopy is used to study the intermittent dynamics that occurs when a concentrated suspension flocculates. Crackling events are detected and their statistical properties analyzed.

WA3 9:50 Diffusing-wave spectroscopy as a probe for neuronal activity
Georg Maret (Invited), Germany

We use near-IR diffusing-wave spectroscopy (DWS) to investigate functional activation of human brain cortex. Stimulation of motor cortical areas leads to significant, hemisphere-dependent increases of the cortical diffusion coefficient. Possible origins of the observed behavior are discussed.

10:20 Coffee and Exhibition

Session 8 (Chair: Roy Pike) 10:40 a.m.

Photon Scattering

WB1 10:40 A fuzzy simultaneous measurement of two polarization vector components
Scott Roger Shepard, U.S.A.

We derive a measurement associated with the angular momentum lowering operator, which describes a simultaneous (yet, reliable) measurement of two non commuting spin vector components. Correlations between two such detectors are also discussed.

WB2 11:00 Fractal structure of biotissues polarization properties
O.V. Angelsky, Ye.G. Ushenko, Yu. A. Ushenko, and A.G. Ushenko, Ukraine

The interconnection between geometry of biotissue structure with their polarization properties has been studied. It has been shown that fractal character of polarization properties of physiologically normal biotissue transforms into a multifractal for a pathologically changed one.

WB3 11:20 2–D stokes-correlometry of biotissues images in pre-clinic diagnostics of their pre-cancer states
O.V. Angelsky, Ye.G. Ushenko, Yu. A. Ushenko, and A.G. Ushenko, Ukraine

This research is directed to combine the possibilities of polarization-sensitive OCT (PSOCT) of biotissue (BT) with correlation method of analysis of 2–D parameters of Stokes vector of object fields for early diagnostics of pretumour changes of connective tissue (CT).

11:40 Lunch and Exhibition (lunch not included with registration fee)

Session 9 (Chair: Robert Brown) 13:30 p.m.

Correlation in Optical Fields

WC1 13:30 Higher-order correlations in speckle fields
J. Ellis and A. Dogariu (Invited), U.S.A.

We show that the joint probability distribution of polarization information and the complex degree of mutual polarization can be used to differentiate between different highly scattering media, which depolarize the light in a global sense.

WC2 13:50 Coupling of correlated entangled photons into single-mode optical fibers
R. Andrews, E.R. Pike, and Sarben Sarkar, Trinidad and U.K.

We present a multimode theory that describes the coupling of single photons generated by collinear Type-I parametric down-conversion into single-mode optical fibers. An expression for the fiber diameter that maximizes the coupling has been obtained.

TuB2 11:40 GRADFLEX, Fluctuations in Microgravity
A. Vailati (Invited), R. Cerbino, S. Mazzoni, M. Giglio, G. Nikolaenko, D.S. Cannell, W.V. Meyer, and A.E. Smart, Italy and U.S.A.

We present the results of experimental investigations of gradient driven fluctuations induced in a liquid mixture with a concentration gradient and in a single-component fluid with a temperature gradient. We also describe the experimental apparatus being developed to carry out similar measurement under microgravity conditions.

TuB3 12:10 Dynamics of gradient driven fluctuations in a free diffusion process
Fabrizio Croccolo, Doriano Brogioli, Alberto Vailati, David S. Cannell and Marzio Giglio, Italy, and U.S.A.

We measure fluctuations' dynamics in a free diffusion process applying a new processing to shadowgraph images to get temporal correlation functions. These functions appeared as decaying exponentials with characteristic time t depending on q vector.

TuB4 12:30 Surface response functions for a thin-film between fluids with infinite boundaries and for a fluid-fluid interface between finite boundaries
William V. Meyer, J. Adin Mann, and Gerald H. Wegdam, U.S.A. and The Netherlands

A simplified surface response function is presented for interfaces with a thin-film between two fluids of infinite extent; and the newly derived results of the surface response function of a fluid-fluid interface between finite boundaries is presented.

12:50 Catered Lunch

13:40 Group photograph for Applied Optics, Kit Meader, official PCS2004 photographer, location to be announced

14:00 Group Canal Tour of Amsterdam or Van Gogh Museum Tour (2 hours, payment included in registration)

WC3 14:10 Spatial properties of a superposed speckle field and its application to the fabrication of random laser media
Takashi Okamoto, Hiroyuki Gotou, Tatsuya Yonemori, and Yasuaki Kawabta, Japan

The statistical properties of a three-dimensional laser speckle field produced by three scattered waves superposed with one another are studied theoretically. It is shown that the spatial anisotropy of intensity distributions still remains even when the three speckle fields are interfered with one another. Superposed fractal speckles and their binarized intensity are also investigated in terms of spatial self-similarity. A new method for fabricating random laser media with the use of photopolymers is proposed, and a preliminary experiment is performed.

14:30 Coffee and Exhibition

Session 10 (Chair: William Meyer) 14:50 p.m.

Correlation in Optical Fields

WD1 14:50 On the prospects of diagnostic of wave dislocation obtained in light
O.V. Angelsky, A.P. Maksimyak, and P.P. Maksimyak, Ukraine

The possibility of application of edge and screw dislocations of the field, obtained in polychromatic light for diagnostics of different phase-inhomogeneous structures, including nanostructures has been considered.

WD2 15:10 The role of caustics in formation of network of amplitude zeros for partially developed speckle field
O.V. Angelsky, A.P. Maksimyak, and P.P. Maksimyak, S.G. Hanson, and Yu.A. Ushenko, Ukraine and Denmark

The topology of a partially developed speckle field is studied using interference techniques. It has been shown that formation of interference forklets in the field gives evidence of changes in the field topology, being the diagnostic sign of transition from a planar Fraunhofer diffraction pattern to a three-dimensional pattern of a diffraction catastrophe.

15:30 Closing Remarks

Poster Session

WE1 *Alexander D. Arkhelyuk, Ukraine*

Estimation of optical-geometrical parameters of nonspherical particles in polarized light

WE2 *Sandor Balog, Juan Jose Saenz, and Frank Scheffold, Switzerland*

A PCS study of correlations and fluctuations in the laser speckle pattern

WE3 *M.S. Dioujeva and V.V. Klyubin, Russia*

Measurement of the Dispersity of Multicomponent Mixtures of Monodisperse Latexes by the Dynamic Light Scattering Method

WE4 *M.S. Gavrylyak, V.S. Lomanets, and P.P. Maksimyak, Ukraine*

The investigation of chaos in the field of optical radiation scattered by liquid crystals

WE5 *Frank Molster, Europe*

ESA Research Announcement of Opportunity in Life and Physical Sciences

Session 1
Introduction and Colloidal Systems

MA 9:00–10:20
Tinbergen Room

Gerard Wegdam, *Chair*

Colloids, Candies, DNA: Packing, Pushing, and Pasting

Paul Chaikin
Princeton University, USA

With an aim toward colloidal architecture of dynamic microstructures, we have fabricated non-spherical colloids, modeled their packing properties with M&M's, manipulated them with AC electric fields and laser tweezers and reversibly stuck them together with DNA.

Nano-Photonics for Novel Photon Correlation Technologies

Robert G.W. Brown
Room 118N, Lanyon North
Queen's University Belfast
Belfast, BT7 1NN
U.K.
Email: r.brown@qub.ac.uk

Summary

Recent experimental realisation of a variety of nano-photonic and nano-electronic components creates many possibilities for new technologies that might be used in photon correlation and scattering experiments.

The laser source can be shrunk to a nano-wire p-n junction, emitting from the UV to near-IR, yet output powers of mW levels can be obtained.

The optics can be shrunk into nano-structured photonic-band-gap optical fibers, capable of being constructed to operate with single-mode performance from the UV to the near-IR - and with expanded single-mode volume to yield real flexibility in optical design and power handling.

Like the laser, the detector can be shrunk to a nano-wire p-n junction – to detect single-photons (or more) with remarkably little noise.

Already one can start to imagine complete photon-correlation opto-electronic structures about the same size as the macromolecules they are to be used to observe, perhaps even embedded in the solutions under study?

But perhaps the most intriguing aspect of the current nano-technology revolution is the impact it might have on photon-correlation processing electronics. We already have various nano-transistors, even single-electron nano-transistors operating at room temperature. Nano-memory storage elements of a variety of structures have been demonstrated recently. The electronic elements of a traditional design of photon-correlator could be transformed in the near future.

Even more intriguing is that the basic structure of the photon-correlator itself might be altered radically by the availability of nano-electronic structures such as carbon nanotubes (CNTs). XOR functions and quantum computing architectures using CNTs have already been experimentally demonstrated. In the very near future they might be configured to provide novel photon-correlation capabilities with extraordinary computing speeds, in remarkably small volumes.

This lecture - partly review - partly novel experimental design - will address all the above topics and attempt to point the way to some novel and advantageous photon-correlation technology possibilities we might realise during the next few years.

Session 2
Colloidal Systems

MB 10:40–12:20
Tinbergen Room

Jan Dhont, *Chair*

Avalanche Behavior in Yield Stress Fluids

Daniel Bonn
Laboratoire de Physique Statistique
Ecole Normale Supérieure
24 Rue Lhomond
F-75231 Paris cedex 05
http://www.lps.ens.fr/recherche/films-aux-interfaces/interests.html
Phone: +33-(0)1-44 32 38 02
Fax: +33-(0)1-44 32 34 33

We show that above a critical stress, typical yield stress fluids (gels, clay suspensions) and soft glassy materials (the colloidal glass of Laponite) start flowing abruptly and subsequently accelerate, leading to avalanches that are remarkably similar to those of granular materials. Rheometrical tests reveal that this is associated to a bifurcation in rheological behavior: for small stresses, the viscosity increases in time: the material "ages", and eventually stops flowing. For slightly larger stresses the viscosity decreases continuously in time: the flow accelerates and we observe a "rejuvenation" of the material by the flow. We show that for the Laponite system, both the aging and the shear rejuvenation can be observed directly using Photon Correlation Spectroscopy and Diffusive Wave Spectroscopy. We propose a simple physical model capable of reproducing the rheological observations.

Aging Dynamics of Translational and Rotational Diffusion in a Colloidal Glass

S. Jabbari-Farouji, E. Eiser, G. Wegdam and D. Bonn
Van der Waals-Zeeman Institute, Valckenierstraat 65, 1018 XE, Amsterdam
E-mail: sjabbari@science.uva.nl

We study the dynamics of translational and rotational diffusion during the aging of the colloidal glass of Laponite using polarized and depolarized dynamic light scattering. The dynamics are qualitatively very similar between the two degrees of freedom. The short-time diffusion is independent of the time elapsed since the sample preparation. The intermediate- and long-time diffusion, on the other hand, changes over several orders of magnitude during the aging, the slowing down of the rotational diffusion being much faster than that of the translational diffusion.

Shadowgraphic Study of Convection Onset in a Colloidal Suspension

R. Cerbino, S. Mazzoni, A. Vailati and M. Giglio
Istituto Nazionale per la Fisica della Materia and Dipartimento di Fisica
Via Celoria 16, 20133 Milano (Italy)
E-mail: roberto.cerbino@fisica.unimi.it, Phone: +39 02 503 17211, Fax: +39 02 503 17712

Abstract: A shadowgraph optical setup is used to study the time evolution of Soret induced convection in a colloidal suspension. We obtain a scale invariant behavior for the solutal Nusselt number as a function of the Rayleigh number.

In a typical Rayleigh-Bénard experiment a horizontal slab of a fluid is contained between a top and bottom plates maintained at two different temperatures (higher temperature at the bottom plate). The order parameter of the system is the Rayleigh number *Ra* and when *Ra* exceeds 1708 the configuration becomes gravitationally unstable and a macroscopic convective flow takes place inside the enclosure: the warm fluid near the bottom plate rises toward the top plate, where eventually cools and begins to sink back to the warm bottom plate.

When the temperature difference between the plates becomes large, the process becomes boundary layer dominated. As soon as the temperature difference is applied two thin conductive boundary layers grow near the isothermal plates until they are eventually destabilized by ascending and descending thermal plumes. For low values of the Prandtl number $\mathrm{Pr} = \nu/\kappa$ (the ratio of the momentum diffusivity over the temperature one) the transition to turbulence takes place for Rayleigh numbers of the order of 10^5. This is due to the relatively high value of the thermal diffusivity κ that favors a chaotic diffusive mixing of plumes. On the contrary, for high values of Pr, a plume can cross the entire layer height without being distorted in shape by heat diffusion and the transition to turbulence takes place at much higher Rayleigh numbers.

One of the most interesting information in convecting systems is given by the Nusselt number *Nu*: the enhancement of the heat flux beyond the conductive value due to convection across the layer. For high Rayleigh numbers ($Ra > 10^7$) [1] it is expected a scaling law in the form:

$$Nu \propto Ra^{p}$$

the numerical value for the exponent p depending on Pr.

Boundary layer convection takes also place in binary mixtures at large Rayleigh numbers, where the concentration differences induced by the Soret effect play the same role of temperature ones. The sudden imposition of a temperature gradient between the plates induces a steady mass flow by means of the Soret effect. Near one impermeable plate mass starts gathering (and getting depleted near the opposite one) and two thin concentration boundary layers are instantaneously formed. Again the boundary layers are rapidly destabilized by concentration plumes. A formal analogy between thermal and solutal convection has been proved [2] providing the mapping of the relevant parameters into equivalent ones with concentration playing the role of temperature: the usual (thermal) Rayleigh number and Prandtl numbers are mirrored by the solutal Rayleigh number Ra_s and the Schmidt number $Sc = \nu/D$ (the ratio of the momentum diffusivity over the concentration one).

In this work we present experimental results on the transient regime of a Soret driven boundary layer convective instability at high solutal Rayleigh numbers. The sample is a diluted aqueous colloidal suspension of silica spheres with an unusually large negative Soret coefficient S_T. The mass diffusion coefficient D is so low is so low that the mixture has a virtually infinite Schmidt number. The experiment is conducted by heating from above so to be sure that the traditional Rayleigh-Bénard instability is not possible, and very high solutal Rayleigh numbers can be easily reached. The study is conducted by using a quantitative Shadowgraph technique to visualize directly the pattern of solutal refractive index modulations in the cell without renouncing to characterize the convective flow within the cell. The root mean square of the shadowgraph intensity signal gives an information equivalent to the turbidity of usual light scattering experiments. In such a way it is possible to estimate the amplitude of the convective flow as a function of time. As is evident in Fig. 1, this latter exhibits a fast onset followed by a set of damped oscillations that lead to a steady state value.

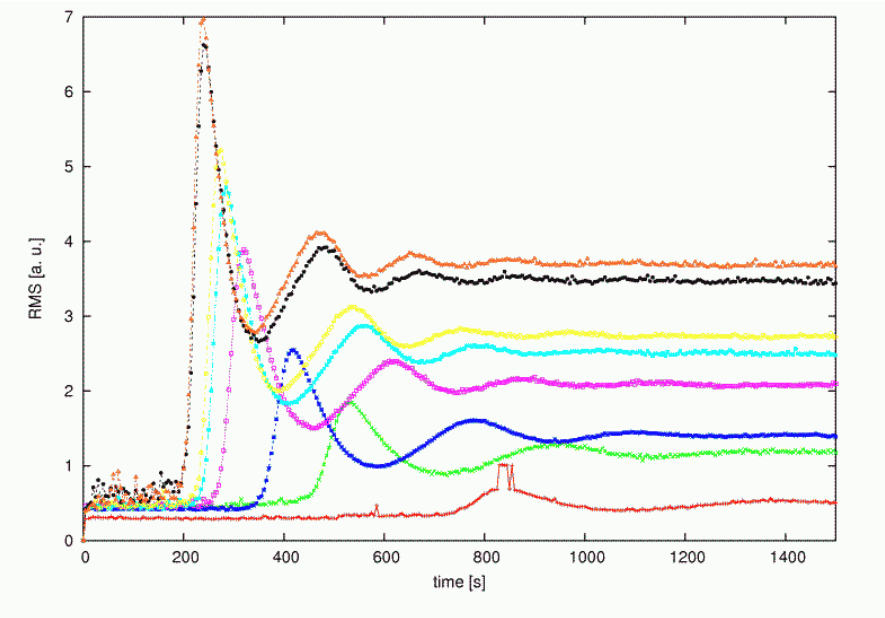

Figure 1: Root mean square of the shadowgraph signal as a function of time for different values of the solutal Rayleigh number. The curves taken at higher Rayleigh numbers are characterized by smaller latency times and larger steady state values.

The characteristic onset time τ_p and oscillation period τ_{osc} show power law behavior

$$\tau_p \propto Ra_s^{-\alpha}$$
$$\tau_{osc} \propto Ra_s^{-\beta}$$

over a range $10^6 < Ra_s < 10^9$ covered by varying the sample height and temperature difference. From the reported behavior for τ_p is possible to determine a scaling relation for the Nusselt number on the base of two issues. First, the initial growth of the boundary layer thickness δ is assumed to be essentially diffusive ($\delta(t) \propto \sqrt{Dt}$), yielding a relation between the steady state boundary layer thickness and Ra_s:

$$\delta \propto Ra_s^{\alpha/2}$$

Second, if convection is induced by applying a constant mass flow at the boundaries (as in our case), the *actual* solutal Rayleigh number is related with Ra_s by $Ra_{act} = Ra_s\delta$ [3], considering the fact that the concentration gradient is bounded within the boundary layers of thickness δ instead of being developed through the whole sample thickness. Considering these two issues and recalling that $Nu \propto 1/\delta$ [1] we obtain

$$Nu \propto Ra_{act}^{\alpha/2-\alpha}$$

The scaling exponent found is $p = 0.37$, compatible with the upper bounding exponent 0.4 predicted in [4] for convection at infinite Prandtl numbers.

References:

[1] E.D. Siggia, "High Rayleigh number convection," Annu. Rev. Fluid Mech. **26**, 137-168 (1994).
[2] V. Degiorgio, "Dynamics of Convective Instabilities in a Horizontal Liquid Layer," Phys. Rev. Lett. **41**, 1293-1296 (1978).
[3] J. Otero et al., "Bounds on Rayleigh-Bénard convection with an imposed heat flux," J. Fluid. Mech. **473**, 191-199 (2002).
[4] C.R. Doering and P. Constantin, "On upper bounds for infinite Prandtl number convection with or without rotation," J. Math. Phys., **42**, 784-795 (2001).

Reentrant Melting of Colloidal Hard Spheres Near a Wall

Roel P.A. Dullens and Willem K. Kegel
Van't Hoff Laboratory, Utrecht University
Padualaan 8, 3584 CH Utrecht, The Netherlands
Phone: +31302532873; E-mail: W.K.Kegel@chem.uu.nl

Concentrated suspensions of colloidal hard spheres near a hard wall were studied in real space by means of time-resolved confocal scanning laser microscopy. Both structure and dynamics of these systems are dramatically different from their bulk analogues (i.e., far away from a wall). In particular, systems that are a glass (a solid phase without long-range positional order) in the bulk show significant hexagonal order near a wall. The hexagonal order is observed to first increase with volume fraction of the colloids, reach a constant value and subsequently decrease. When hexagonal order decreases, the mobility of the particles starts increasing with volume fraction. These observations are consistent with a reentrant melting transition. However, the behavior of static correlation functions indicate that the in-plane structure near a wall is hexatic rather than crystalline, reflecting the two dimensional character of dense matter near walls.

Reference: R.P.A. Dullens and W.K. Kegel, Phys. Rev. Lett. **92**, 195702, (2004).

Session 3
Colloidal Systems

MC 13:50–15:10
Tinbergen Room

Dave Weitz, *Chair*

DLS and FCS on Tracer Spheres in Concentrated Rod Dispersions

K. Kang [1], J. Gapinski [2], M.P. Lettinga [1], J. Buitenhuis [1],
G. Meier [1], Jan K.G. Dhont [1], A. Patkowski [2]

[1] Forschungszentrum Jülich
Institute für Festkörper Forschung (IFF), Weiche Materie
D-52425 Jülich, Germany

[2] A. Mickiewicz University
Umultowska 85, Poznan, 61-614 Poland

Abstract

Diffusion of tracer spheres in dispersions of rods is measured by dynamic light scattering (DLS) and fluorescence correlation spectroscopy (FCS), as a function of the rod concentration and the size ratio of the sphere to the rod. By comparing with DLS, FCS is shown to measure long-time diffusion only for relatively small spheres. A variational approach for the prediction of long-time self diffusion coefficients is compared with experiments.

1 Introduction

In *Fluorescence Correlation Spectroscopy* (FCS) a single laser beam is strongly focussed, and the fluorescent intensity from a region around the focal point (the so-called "confocal volume") is probed. The detected intensity distribution within the confocal volume is well described by a Gaussian profile,

$$I_0(\mathbf{r}) \ \sim \ \exp\{-(x^2+y^2)/2\sigma_1^2\} \ \exp\{-z^2/2\sigma_2^2\} \ , \tag{1}$$

where σ_1 and σ_2 measure the width of the confocal volume in the plane perpendicular to the propagation of the beam and its height along the propagation direction, respectively. Typically, $\sigma_1 \approx 100-300$ nm , and $\sigma_2 \approx 200-600$ nm. The fluorescent intensity auto-correlation function $C_f(t)$ can be shown to be equal to (see for example refs.[1,2]),

$$C_f(t) \ \sim \ \left[1+\frac{D_s^l\, t}{\sigma_1^2}\right]^{-1} \ \left[1+\frac{D_s^l\, t}{\sigma_2^2}\right]^{-1/2} . \tag{2}$$

where k_j is the j-component of $\mathbf{k}$. The fluorescent intensity auto-correlation function thus decays algebraically with time, with two characteristic time constants $\sigma_{1,2}^2/D_s^l$. The geometrical constants $\sigma_{1,2}$ can be determined from a measurement of a dilute system where D_s^l is equal to the Einstein diffusion constant, that can be obtained independently from dynamic light scattering.

The assumption in eq.(2) is that the tracer sphere reaches its long-time limiting diffusive behaviour long before it diffuses over distances comparable to the size of the confocal volume. As will be seen in the experimental section, this is not always the case.

It should be mentioned that the geometrical parameters $\sigma_{1,2}$ can deviate from the actual confocal volume dimensions in eq.(1) when the tracer sphere is not small in comparison to the actual size of the

confocal volume. In the present paper we are interested only in ratios of diffusion coefficients, so that the "effective dimension" of the confocal volume is not needed.

Dynamic Light Scattering (DLS) measures self diffusion when the intensity of the tracer spheres dominates and the spheres do not mutually interact. The measured normalized electric field auto-correlation function $g_1(k,t)$ is then equal to,

$$g_1(k,t) \; = < \exp\{i\,\mathbf{k}\cdot(\mathbf{r}(t)-\mathbf{r}(0))\} > \,, \tag{3}$$

where $\mathbf{k}$ is the scattered wavevector and $\mathbf{r}(t)$ is position of a tracer sphere at time t. Expansion with respect to small wavevectors leads to,

$$g_1(k,t) \; - \; \exp\left\{-\tfrac{1}{6}\,W(t)\,k^2 + "\mathcal{O}(k^4)"\right\} \,, \tag{4}$$

where $W(t) = <|\,\mathbf{r}(t)-\mathbf{r}(0)\,|^2>$ is the mean-squared displacement. Hence, plotting $-6\ln\{g_1(k,t)\}/k^2$ for a given time as a function of k^2, and extrapolating to $k=0$, yields $W(t)$ for the particular time under consideration. The long-time self-diffusion coefficient D_s^l then follows from $dW(t)/dt = 6\,D_s^l$, where the slope of $W(t)$ versus time should be evaluated at long times, that is, times that are large in comparison to microstructural relaxation times of the rods.

Experimental data at low rod concentration are compared with a *theoretical prediction based on a variational solution of the Smoluchowski equation*. A more detailed discussion for a similar approach for self diffusion of rods can be found in [3]. For low volume fractions φ of rods, the long-time self diffusion coefficient D_s^l of a sphere can be written as,

$$D_s^l \;=\; D_0\,\left[\,1-\alpha\,\varphi+\mathcal{O}(\varphi^2)\,\right] \,, \tag{5}$$

where $D_0 = k_B T/6\pi\eta\,a$ is Einstein's diffusion coefficient of a freely diffusing sphere with radius a in the pure solvent with shear viscosity η. The variational approach renders numerical values for α as a function of the rod aspect ratio (L is the length and D the thickness of the rods), L/D and the ratio of the length of the rod and the diameter $2a$ of the sphere $L/2a$. The basic idea of the variational approach is as follows. As noted by Batchelor [4], the long-time self diffusion coefficient can be written as $D_s^l = k_B T/\gamma$, where the friction coefficient γ includes both interactions of the sphere with solvent molecules *and* the rods. Hence, a weak constant force $\mathbf{F}^{ext}$ is exerted on the sphere, until the sphere attains a stationary ensemble averaged velocity $<\mathbf{v}>$, from which the friction coefficient follows as,

$$\mathbf{F}^{ext} \;=\; \gamma \;<\mathbf{v}> \;. \tag{6}$$

The calculation of the long-time self diffusion coefficients thus amounts to calculate the ensemble averaged stationary velocity of the sphere due to a constant, weak external force. Two ingredients are thus needed for the calculation of the long-time self diffusion coefficient : a microscopic expression for the velocity and an explicit expression for the probability density function with respect to which the ensemble average can be calculated. The latter is obtained by a variational principle.

2 Results

The rod solution consisted of fd-virus dispersions in 20 mM TRIS buffer (usually with 100 mM NaCl added). The length of an fd-virus particle is 880 nm, its thickness is 6 nm and its persistence length is 2200 nm. The spheres we used are silica spheres with a radius varying between 35 nm and 500 nm, and the protein BSA which has a radius of about 3 nm.

As an example, Fig.1 shows diffusion coefficients as a function of fd concentration as measured by DSL and FCS, for a silica tracer sphere with a radius of 210 nm. Long- and short-time diffusion coefficients

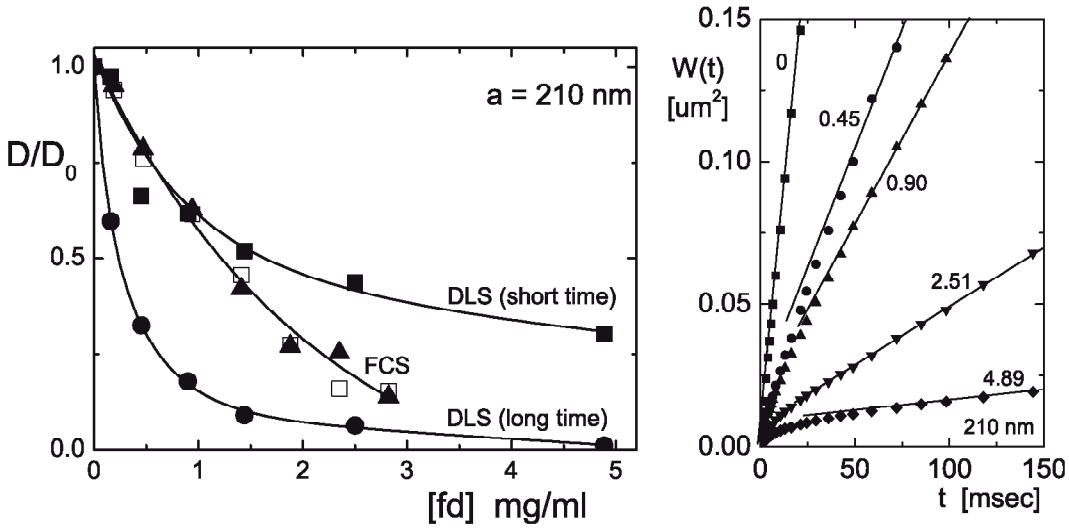

Figure 1: Left figure : Diffusion coefficients as measured by DLS and FCS for 210 nm tracer spheres. Open symbols refer to low salt concentration (20 mM TRIS buffer), solid symbols to high salt concentration (20 mM TRIS buffer + 100 mM NaCl). Right figure : The mean squared displacement $W(t)$ as determined from DLS experiments for various fd-concentrations, as indicated in the figure (in units of mg/ml).

are determined from mean squared displacements as obtained by DLS (see right figure in Fig.1). As can be seen, FCS measures short time diffusion for low fd concentrations and long time diffusion for high fd concentration. The reason for this can be recognized from the right figure in Fig.1 : for lower fd concentrations, the long-time limit is reached for displacements which are comparable or larger than the linear dimensions of the confocal volume. For intermediate fd concentrations, short-time or diffusion on an intermediate time scale is probed by FCS. The microscopic origin of this behaviour of diffusion coefficients as measured by FCS will be discussed.

The fd-concentration dependence of the long-time self diffusion coefficient of a sphere was found to strongly depend on the size ratio of the sphere and that of fd-virus. Results will be presented on long time diffusion, with a comparison to theory for small fd-virus concentrations.

References

1) S.T. Hess, S. Huang, A.A. Heikal and W.W. Webb, Biochemistry **41**, 697 (2002)

2) S.R. Aragón and R. Pecora, J. Chem. Phys. **64**, 1791 (1976), Biopolymers **14**, 119 (1975)

3) J.K.G. Dhont, M.P.B. van Bruggen, W.J. Briels, Macromolecules **32**, 3809 (1999)

4) G.K. Batchelor, J. Fluid Mech. **131**, 155 (1983)

Effect of Electrolyte Concentration on the Hydrodynamic Radius of Polymer Lattices as Measured With PCS

Carlos A. Rega and Robert O. Jack
Malvern Instruments Ltd, Enigma Business Park, Grovewood Rd, Malvern,
WR14 1XZ, Worcs. England
E-mail: carlos.rega@malvern.co.uk

Abstract: In this paper we study the effect of electrolyte concentration on the hydrodynamic radius of polymer latex particles using PCS. Our measurements show that the concentration of electrolyte on the surface charge of the particles has a significant effect on the particle size as measured using PCS.

1. Introduction

In a PCS measurement the size of a suspended particle is calculated from the fluctuations of scattered light, using the Stokes-Einstein equation, which relates the diffusion coefficient of a particle to its hydrodynamic radius[1]. In colloidal systems, such as polymer lattices in the presence of electrolyte, the hydrodynamic radius is not a characteristic of the particle, but of the system itself. In such systems the hydrodynamic radius of the particle includes the effect of the double layer which arises from the particles surface charge [2,3]. In this work we present the results of PCS measurements on some model latex systems which show the effect of electrolyte concentration in the value of the hydrodynamic radius obtained from the measurements.

References

[1] B.J. Berne and R. Pecora, *Dynamic light scattering with applications to chemistry, biology and physics* (John Wiley and Sons, 1976).
[2] R.J. Hunter, *Zeta potential in colloid science. Principles and applications* (Academic Press, 1981).
[3] R.J. Hunter, *Introduction to modern colloid science* (Oxford University Press, 1993).

Physics of Photonic Crystals: Of Dreams and Nightmares

Willem L. Vos
Complex Photonic Systems (COPS)
University of Twente, The Netherlands

We present first evidence that photonic crystals control emission rates of embedded light sources. We analyze intrinsic disorder in 2D and 3D crystals and conclude that applications, especially integrated circuits, have a dim future.

Session 4
Colloidal Systems

MD 15:30–16:30
Tinbergen Room

Paul Chaikin, *Chair*

Multiple Light Scattering Probes of Fluid and Solid Soft Materials

Frank Scheffold, Fréderic Cardinaux, Ronny Vavrin and Peter Schurtenberger
Physics Department, University of Fribourg, CH-1700 Fribourg, Switzerland
E-mail: Frank.Scheffold@unifr.ch

Abstract: We report on recent advances in single and multi-speckle Diffusing Waves Spectroscopy. Special emphasis is given to slowly relaxing or completely arrested systems, such as dense surfactant solutions or colloidal gels.

1. Introduction

To characterize the structural and dynamic properties of soft materials, information on the relevant nano- and mesoscopic length scales is required. Such information is often obtained from traditional photon correlation spectroscopy (PCS) techniques, such as static and dynamic light scattering (SLS/DLS) in the single-scattering regime. In dense systems, such as colloidal suspensions and gels, however, these powerful techniques frequently fail due to strong multiple scattering of light. Furthermore, many (dense) soft materials are viscoelastic solids, meaning that they are nonergodic. Ergodicity, however, is an important condition for the applicability of PCS [1].

Diffusing wave spectroscopy (DWS), which is photon correlation spectroscopy from turbid media, allows the study such dense complex systems [2]. It can be used to analyze the local dynamic properties by measuring the intensity fluctuations of the diffusively transmitted light. Because in the case of DWS the light is scattered from a large number of scatterers, each individual one must move only a small fraction of a wavelength for the cumulative change in optical path length to be a full wavelength. Therefore, DWS can probe motion on very short sub-wavelength scales from less than 1 nm to about 50 nm – which is quite unusual for a scattering technique. Still the problem of nonergodicity persists for the case of DWS – though it may appear only for rather solid systems since the scatterers need to be trapped on a correspondingly smaller length scale.

For solid-like systems the speckle time and ensemble average of multiply scattering light are different on the timescale of a typical experiment [3, 4]. New developments in photon correlation spectroscopy nowadays provide efficient routes to overcome these non-ergodicity problems in DWS. Here we report on the application of spatial averaging schemes in PCS and two cell DWS (TCDWS) [5-7]. Based on a combination of single- and multispeckle detection schemes, it is now possible to cover "in a single shot" relaxation times from a few nanoseconds to minutes or hours. In DWS microrheology experiments the accessible elastic properties of viscoelastic fluid or solid materials range roughly from below 1 Pa to several 100 kPa. Typical application examples are briefly discussed such as DWS from colloidal gels and microrheology of dense surfactant solutions[1].

2. Experimental Setup

A typical DWS setup is shown below. An intense laser beam (Verdi from Coherent) is scattered from a turbid sample contained in a temperature controlled water bath. The transmitted light is analyzed in a two-cell geometry (TCDWS): light transmitted diffusively from the sample cell is imaged via a lens onto a second cell (e.g. a rotating ground glass). Subsequently, the light is detected with a single-mode fiber (SMF) and analyzed digitally (digital correlator Flex02-12D and PC). In parallel a CCD camera can be used to detect the fluctuations of the scattered light. The camera can be placed either in transmission (using a beamsplitter) or in backscattering (as shown).

CCD camera based DWS allows direct access to slow relaxations or completely arrested (solid) systems. Instead of analyzing the fluctuations of the intensity at a single spatial position (one speckle spot) one analyzes a large area of the intensity pattern of the scattered light (hence multi-speckle). The main advantage of the CCD camera as a detector is the access to nonergodic samples and the significantly decreased data acquisition time since a large number of scattering experiments is performed simultaneously. The main drawback of camera based DWS is the currently still much limited time resolution of CCD cameras. Typically correlation times down to a few ms can be accessed (as compared to 10ns with a standard photo-multiplier- digital correlator setup), which is a particular problem for DWS, where fast relaxation processes are frequently found.

To overcome the problem of non-ergodicity in a traditional PCS experiment a sandwich geometry can be used in DWS. The first cell contains the sample to be investigated. The second cell, which serves to properly average the signal of the first cell only, has to be an ergodic diffuser with very slow dynamics and moderate turbidity. A combination of two-cell DWS and multi-speckle DWS, as shown in Figure 1, turns out to be a perfect combination to overcome most of the commonly encountered experimental limitations.

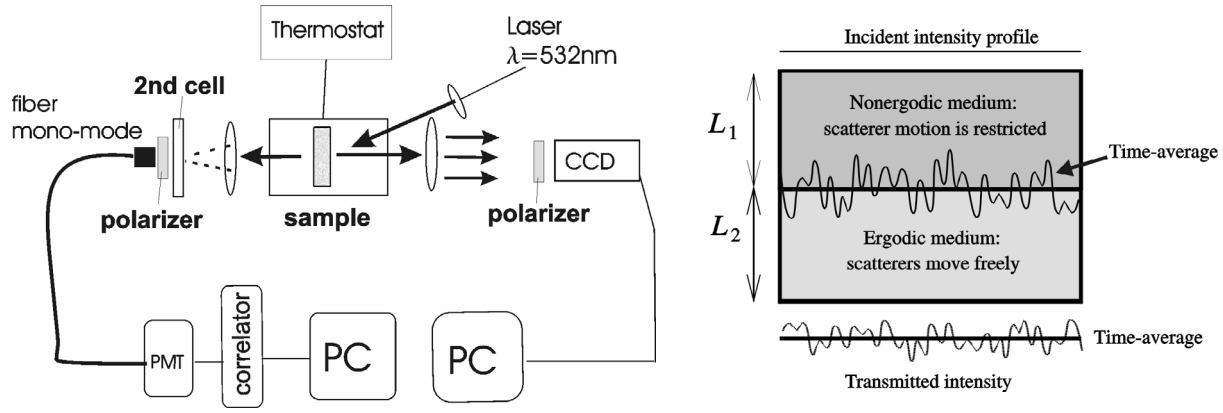

Figure 1 Left: Typical setup for DWS in transmission and backscattering with an option for both single and multi-speckle analysis. Right: schematic plot of the two-cell setup. The first cell is filled with a liquid or solid-like sample and the second cell is an ergodic system (e.g. latex spheres in glycerol or a rotating diffusor). After the first cell L_1 the time average of the transmitted light intensity depends on the position at the interface. Adding a second ergodic cell leads to an efficient average of the static speckle pattern after L_2 without obscuring the time fluctuations that stem from the scatterer motion in the first cell.

3. Applications

Here we will discuss recent advances in multiple light scattering from turbid fluid and solid-like media. In our work particular emphasis is given to dense complex fluids, such as colloidal suspensions and gels. For these systems strong multiple scattering of light is omnipresent and furthermore the systems are solid or solidify with time.

DWS based optical microrheology

As a prime example for the application of DWS technique we discuss tracer microrehology of viscoelastic materials. The underlying idea of optical microrheology is to study the thermal responses of small (colloidal) particles embedded in a material. Thereby it is possible to obtain quantitative information about the loss and storage moduli, G'(ω) and G''(ω), over an extended range of frequencies. This technique in its present form was introduced some years ago when Mason and Weitz suggested a quantitative relation between the tracer mean squared displacement and the complex shear modulus [8]. Since then DWS has been the most popular technique to study the thermal motion of the tracer particles, because it allows relatively easy access to small particle displacements over an extended range of distances [9].

The application example in figure 2 shows measurements of a concentrated aqueous solution of the surfactant Cetylpyridinium Chloride (CPy 100mM) with Sodium Salicylate (60mM) at T=30°C. Under these conditions the surfactant molecules self-assemble and form large elongated aggregates called worm-like micelles. Surfactant-free white sulfate latex (diameter 720nm) as provided by Interfacial Dynamics Corporation (IDC) were added to the sample to reach a final volume fraction of ca. 2%. Excellent agreement was found with classical oscillatory shear experiments.

Colloidal gels as a typical example for a viscoelastic solid material

For concentrated colloidal dispersions DWS is able to provide information about the dynamics during aggregation and gelation [5]. Figure 2 shows the measured autocorrelation function as a function of time before and after the sol-gel transition. A suspension of monodisperse polystyrene latex spheres (diameter ca. 20nm) is destabilized by increasing the solvent ionic-strength with a catalytic reaction. Thereby the electrostatic repulsion of the double layer is reduced and the particles aggregate due to van-der-Waals attraction. At early stages, clusters form due to particle aggregation and the decay of the correlation function shifts to higher correlation times due to the slower motion of the clusters. Gelation occurs when a single cluster fills the entire sample volume. After the sol-gel transition we observe that the correlation function does not decay to zero but remains finite. In this regime two-cell DWS is most valuable since it allows the characterization of turbid media without any mechanical movement or further processing of the data.

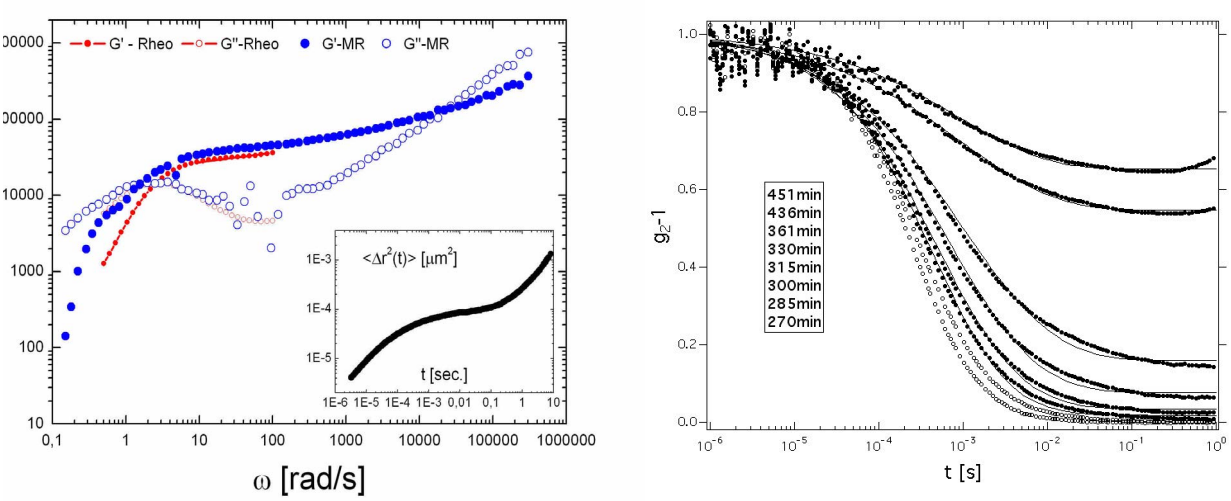

Figure 2 Left: Classical rheometry (Rheo) and optical microrheology (MR) of a highly viscoelastic micellar solution at 30°C. Inset: Mean squared displacement of the 720nm tracer particles detected by DWS. Right: Sol-Gel transition in a colloidal suspension (19 nm polystyrene spheres at 3.8% vol. fract.) for different times after destabilization (inset). The data has been obtained using two-cell DWS with a slowly rotating diffuser (ground glass plate).

3. Conclusions and Outlook

We have shown that recent developments in PCS from turbid systems now provide access to a variety of solid like systems. Currently these techniques are mainly used by specialists. However in the near future they should become a standard tool both in academic and applied research. First instruments of this generation are already commercially available (LSInstruments, www.lsinstruments.ch) and applications in industrial environments are underway. In summary we can say that it is now possible to access within minutes (or even seconds) dynamic properties of any kind of soft material provided the system is homogeneous on macroscopic length scales.

4. Acknowledgments

We thank Luca Cipelletti for his help in setting up the CCD camera based DWS and Peter Fischer for providing the concentrate surfactant solution. Discussions with Hugo Bissig and Veronique Trappe are gratefully acknowledged.

5. References

[1] Scheffold, F. and P. Schurtenberger, *Light Scattering Probes of Viscoelastic Fluids and Solids.* Soft Materials, 2003. **1**(2): p. 139-165

[2] D.A. Weitz and D.J. Pine in: Brown, W., *Dynamic light scattering : the method and some applications*. Monographs on the physics and chemistry of materials ; 49. 1993, Oxford England New York: Clarendon Press; Oxford University Press. xvi, 735.

[3] Pusey, P.N. and W. van Megen, *Dynamic Light-Scattering by Non-Ergodic Media.* Physica A, 1989. **157**(2): p. 705-741.

[4] Xue, J.Z., et al., *Nonergodicity and Light-Scattering from Polymer Gels.* Physical Review A, 1992. **46**(10): p. 6550-6563.

[5] Romer, S., F. Scheffold, and P. Schurtenberger, *Sol-gel transition of concentrated colloidal suspensions.* Physical Review Letters, 2000. **85**(23): p. 4980-4983.

[6] Scheffold, F., et al., *Diffusing-wave spectroscopy of nonergodic media.* Physical Review E, 2001. **6306**(6): p. art. no.-061404.

[7] Cardinaux, F., et al., *Microrheology of giant-micelle solutions.* Europhysics Letters, 2002. **57**(5): p. 738-744

[8] Mason, T. G., Ganesan, K., van Zanten, J. H., Wirtz, D., & Kuo, S. C. *Particle tracking microrheology of complex fluids*. Physical Review Letters, 79, 3282–3285 (1997).

[9] Harden, J.L. and V. Viasnoff, *Recent advances in DWS-based micro-rheology.* Current Opinion in Colloid & Interface Science, 2001. **6**(5-6): p. 438-445.

Scattering Probes of the Growth and Elasticity of Colloidal Gels

David A Weitz
Harvard, USA

Dynamic light scattering is used to determine the elasticity of colloidal gels. Comparison of microgravity and earth based data suggest new aging mechanisms. The gelation process can exhibit hallmarks of the glass transition.

Session 5
Near Field Scattering

TuA 9:00–10:50
Tinbergen Room

Marzio Giglio, *Chair*

Statistics of Optical Near-Fields

A. Dogariu and A. Apostol
School of Optics, CREOL,
University of Central Florida, Orlando, Florida

Abstract: We demonstrate that the second-order statistics and the spectral density in the close proximity of an optically inhomogeneous medium are quite different from the far-field properties of radiation and are determined by the statistical characteristics of the interface.

Next generation photonics-based technologies will ultimately rely on novel materials and devices. For this purpose, phenomena at subwavelength scales have been actively studied in order to advance both fundamental knowledge and experimental capabilities. Understanding the statistical properties of the radiation at subwavelength scales should be of paramount importance in the design of miniaturized optical sources, detectors, and sensors.

When optical fields interact with randomly inhomogeneous media, a speckle pattern is formed due to interference effects of the elementary wavelets originating from different scattering centers. The variations of the field amplitude and phase lead to the familiar, random appearance of speckle. For the case of infinitely extended media or at large distances from finite size media, the statistical properties of such random fields are rather well understood. However, little is known about the field distributions very close to the surface of a random medium where the presence of evanescent fields can modify the statistical properties of the field. In the proximity of an interface, the field contains both homogeneous and inhomogeneous components due to both multiple scattering in the bulk and the specific surface morphology. So far, near-field scanning techniques have been used to investigate different aspects of electromagnetic fields in close proximity of interfaces aiming primarily at extending the spatial resolution of various optical microscopies. We have systematically studied the coherence properties in the near-field of highly inhomogeneous media which are known to produce significant field fluctuations and a radiant intensity typical to incoherent sources[1].

The radiation originating from a highly scattering medium can be regarded as being produced by a stochastic source of radiation with properties described in the frame of a coherence theory. The conventional theory suggests that the fields radiated by statistically homogeneous sources correlate over spatial regions of the order of the wavelength irrespective of the distance z from the source[2]. This fundamental result has been obtained by neglecting the contribution of short-range evanescent waves and it has been successful in describing the far-field properties of thermal emission. One has to realize that this description is pertinent to coherence phenomena of radiation produced by a practically infinite source and does not account for detailed source characteristics. Note also that classical measurements of spatial coherence properties are usually performed at much larger distances z where the limited size of the source cannot be ignored.

A consistent description can be developed by considering the surface of the random medium as being equivalent to an homogeneous, planar, statistically stationary source of optical radiation. This source, located at $z = 0$, is characterized by a cross-spectral density function

$$W^{(0)}(\rho_1, \rho_2, \omega) = F^{(0)}(\rho_2 - \rho_1, \omega), \qquad (1)$$

[1] A. Apostol and A. Dogariu, Coherence properties near interfaces of random media, Phys. Rev. E. **67**, 055601 (R), (2003).

[2] W. H. Carter and E. Wolf, Coherence properties of lambertian and non-lambertian sources, J. Opt. Soc. Am.**65**, 1067, (1975).

where ρ_1 and ρ_2 are two-dimensional position vectors in the plane of the source and ω is the radiation frequency. The source generates, in the half space $z > 0$, a field with the cross-spectral density function given by

$$W(\mathbf{r}_1, \mathbf{r}_2, \omega) = k^2 \int\int_{-\infty}^{\infty} \tilde{F}(ks_x, ks_y, \omega) e^{ik(\mathbf{s}\mathbf{r}_1 - \mathbf{s}^*\mathbf{r}_2)} ds_x ds_y, \qquad (2)$$

where $\tilde{F}(ks_x, ks_y, \omega)$ is the two dimensional Fourier transform of cross spectral density at $z = 0$, $F^{(0)}(\rho_1 - \rho_2, \omega)$. In general, one can decompose the cross spectral density function in low- and high-frequency components:

$$W(\delta x, \delta y, z, \omega) = W_{\text{hom}}(\delta x, \delta y, \omega) + W_{ev}(\delta x, \delta y, z, \omega) \qquad (3)$$

which can be independently calculated. The first and second order statistics as well as the spectral density of radiation can be then evaluated as illustrated in the following. Our results show that the state of coherence in the plane of the interface affects not only the field coherence length but also the near-field spectral shift toward larger wavelengths (red shift).

The spatial coherence properties were measured near the surface of various random, highly scattering media which were illuminated in a transmission geometry. The scattering media were compact slabs of microparticles with diameters of the order of hundreds of nanometers Their scattering properties are characterized by the correlation length of the refractive index fluctuation and by the r.m.s. height of the surface which is typically a fraction of radiation's wavelength.

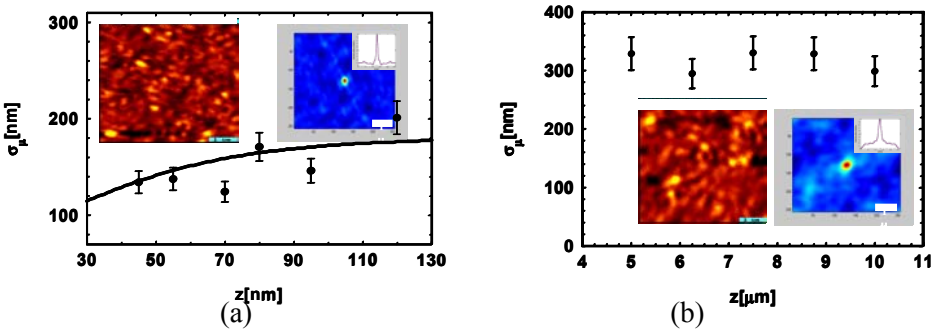

Figure 1. Near-field coherence length σ_μ as a function of the distance z from the interface for distances a) smaller and b) larger than the wavelength of light (λ=488nm). The dashed line in (a) represents the theoretical predictions of the model outlined in the text. The insets illustrate typical speckle fields and their corresponding correlation functions.

A collection mode near-field scanning optical microscope (NSOM) was used to obtain simultaneously near- or far-field optical images as well as the corresponding AFM topography. We refer here as "near-field" to images collected at distances z smaller than the wavelength, and as "far-field" for those distances z of 5-20 wavelengths from the interface. In the close vicinity of the surface of a highly inhomogeneous medium, the NSOM probe collects both the homogeneous and inhomogeneous components of the transmitted field. When the intensity is averaged over an area of 5x5 microns, a negative exponential dependence on z is observed (as shown in Fig. 2a), proving that the detected signal contains a significant contribution of inhomogeneous components. As expected, this contribution vanishes for distances z larger than the wavelength of light, where only the homogeneous components are contributing. The spatial distribution of the detected intensity resembles the typical spatial variations present in a classical speckle pattern (see the inset in Fig 1a). As opposed to the far-field situation, the field coherence length σ_μ measured in the near-field of a highly inhomogeneous medium has a significant dependence on the distance z as can be seen in Fig 1a. In addition, we found that σ_μ is always

smaller than the far-field saturation value. This is predicted by our model of an optical field radiated by a planar source generating both propagating and evanescent waves (continuous line in Fig. 1a)[3].

It is worth mentioning here that, at a given observation point in the speckle pattern, the field is a superposition of contributions originating from different locations within the bulk of the random medium and we can consider that the amplitude and the phase of the elementary phasors satisfy circular Gaussian statistics. This assumption is supported by the first-order statistics of intensities determined in both near- and far-field and illustrated in Figure 2. Using standard properties of Gaussian random variables, the field correlation function can then be expressed in terms of intensity correlation function.

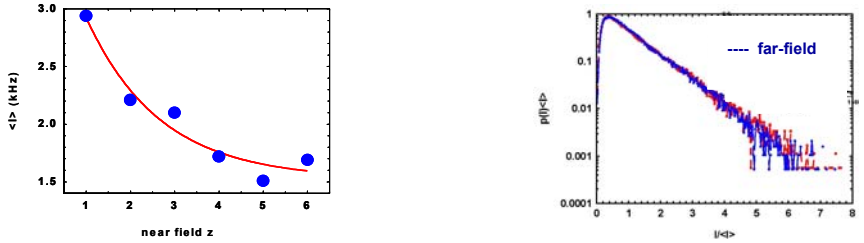

(a) (b)

Figure 2. (a) Near-field intensity as a function of the distance *z* from the interface. (b) Normalized intensity probability density function measured in the near-field (z=20nm) and in the far-field (z=5000nm).

So far, we have shown that the simple model of a planar source qualitatively describes both first- and second-order statistical properties of the field emitted at the surface of a highly random medium. This model offers also a direct relationship between the measurable statistical properties of the optical near-field and the statistical properties of an equivalent planar source of radiation which, in turn, are determined by the physical properties of the random medium.

Using the same model, one can also calculate the spectral density in the near-field of a random medium[4]. Careful analysis shows that the evanescent waves tend to shift the spectrum of light toward longer wavelengths and that this spectral shift depends on the field correlation length in the plane of the source[5].

Figure 3. Typical topography of a random medium and the experimental far-field spectrum measured at z=1500nm together with the experimentally measured and the theoretically predicted spectra for the evanescent field evaluated at z=200nm.

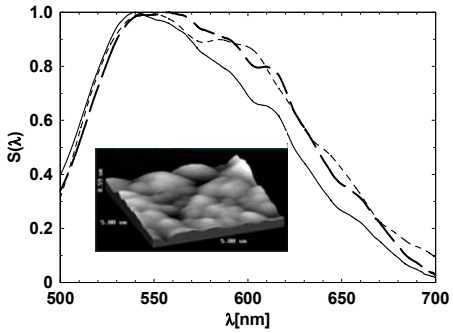

The differences between far- and near-field spectra which are determined by the high-frequency components of the spectral density and depend on the coherence properties of an equivalent planar source. This dependence can be used to determine the statistical characteristics of the interface.

[3] A. Apostol and A. Dogariu, Spatial correlations in the near-field of random media, Phys. Rev. Lett. 91, 093901, (2003)
[4] H. Roychowdhury and E. Wolf, Effects of spatial coherence on near-field spectra, Opt. Lett., 28, 170, (2003).
[5] A. Apostol, A. Dogariu, "First and second-order statistics of optical near fields", Opt. Lett., 29, 920 (2004).

Near Field Scattering

Marco A. C. Potenza, Doriano Brogioli, Alberto Vailati, and Marzio Giglio
INFM and University of Milan, via Celoria, 16I-20133 – Milano - Italy
E-mail: Marco.potenza@unimi.it

Abstract: We present a novel scattering technique based on the statistical analysis of the random intensity distribution in the near field of the light scattered by a sample.

1. Introduction

It has been recently pointed out [1] that the features of the scattered light close to a disordered sample made of randomly distributed particles, in a condition called *Near Field Scattering* (NFS), can be used to recover the information about the light scattered by the sample as the traditional low angle light scattering (LALS) does. For scatterers whose sizes are comparable or larger than the wavelength of the impinging radiation, this condition leads to the remarkable result which shows that the speckles have the same size of the scatterers, independently of both the wavelength and the distance from the sample. It is worthwhile to stress that the near field conditions we refer to, has a completely different meaning with respect to the physics related to evanescent, non-propagating, wave phenomena, that people also call as *near field*. In our case the near field begins at an appreciable distance far from the sample, much larger than the distances typically encountered in evanescent phenomena.

NFS was recently proposed as a novel technique alternative to the traditional low-angle static light scattering, which works by collecting the scattered light in the far field of the sample, and allows the recovery of the scattered angular distribution $I(q)$, being q the scattering wavevector defined as $q = (4\pi/\lambda)\sin(\theta/2)$ and θ the scattering angle. Conversely, NFS operates in proximity of the sample and requires a remarkably simple optical setup: a collimated laser beam is simply shone onto a square cell containing the sample, and the scattered light is collected by using a lens which makes an image of a plane in the near field of the sample onto a CCD sensor. Two different configurations can be adopted: a homodyne [1,2] layout in which the transmitted beam is stopped and only the scattered light can reach the sensor, and a heterodyne [3,4] layout where the transmitted beam is let to superimposes to the scattered light and the resulting interference pattern is then detected by the sensor. In both cases, due to the stochastic interference between the waves emerging from the sample, the recorded images have a speckled appearance and contain information on the scattered electric field correlation function, ultimately related to the scattered intensity distribution $I(q)$, the same quantity measured in a classical small angle light scattering instrument. The heterodyne version has been shown to be much more effective as a scattering technique. One of the most attractive features is the capability to rigorously get rid of the stray light. Furthermore, the optical layout is very simple and free from stringent alignment requirements.

2. The Near Field Scattering Condition

When observed in the far field, the statistical properties of the speckle field can be described in terms of the very famous Van Cittert-Zernike (VCZ) theorem, which relates the shape and the size of the speckles to the intensity profile of the illuminated sample. Quantitatively, if D is the diameter of the illuminated area, λ the wavelength of the light, and z the distance between the sample and the observation plane, the average speckle size d_{FF} is given by

$$d_{FF} \sim \lambda z / D \tag{1}$$

in which the suffix FF stands for "far field".

When the observation distance z is not so large and/or the scatterers are not point-like but comparable or larger than the wavelength of the impinging radiation, it may happen that a region in the observation plane receives light only from a part of the illuminated sample. Let's assume to illuminate scatterers of size a with a large and uniform laser beam of diameter D and wavelength λ. The scattered light is detected at a distance z by means of a small sensor, in a region where the stochastic interference of several scattered contributions produces a speckled field. Since each particle scatters most of the light within an angular lobe of width $\theta \sim \lambda / a$, the sensor will collect light from effective source of diameter $D^* \sim \lambda z / a$, which can be over a given range of distances smaller than D. Now, applying Eq. (1) one can estimate the size of the near field (NF) speckles d_{NF} given by

$$d_{NF} \sim \lambda z / D^* \sim a \tag{2}$$

This result, reported for the first time in Ref. [1], is rather remarkable because shows that the near field speckles have the same dimensions of the scattering particles, regardless of the distance z and wavelength λ. Thus, the near field speckles are

completely different from the far field ones, depending only on the scatterers and not on the geometry of the optical layout. Physically speaking, one can note that Eq. (2) is the result of the exact compensation between the explicit dependences on z of d_{NF} and D^*, both linear with z. The NFS condition fails when the distance z is such that diameter D^* becomes equal or larger than the beam diameter D.

3. Heterodyne Near Field Scattering

In a real experiment the sample is typically constituted by scatterers immersed in a transparent fluid. The near field speckles can then be obtained by adopting two different schemes: 1) a homodyne configuration in which the transmitted beam is stopped and only the scattered light reach the sensor and 2) a heterodyne configuration where the transmitted beam is let to interfere with the scattered field. As pointed out in the literature (see [1–4]), the heterodyne version has shown to be much better in many respects.

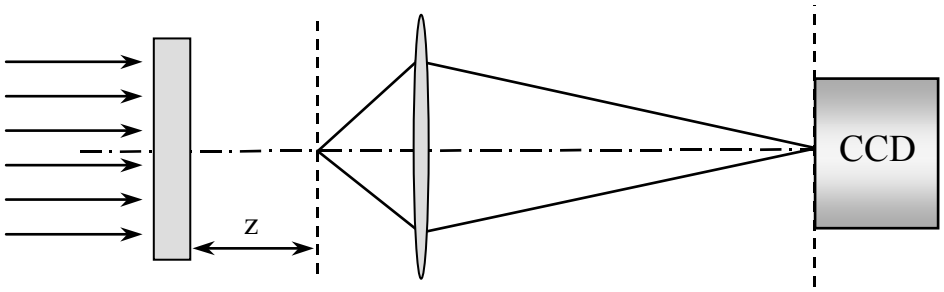

Figure 1: The heterodyne optical set-up. The sample is illuminated with a large collimated beam, the intensity distribution at distance z from the sample is imaged by the lens on the CCD sensor. Notice that, differently from the set-up of Fig. 3, the intensity distribution is the result of the interference between the transmitted beam and the scattered fields.

It makes the optical setup much easier and robust and also simplifies the data analysis. This configuration is sketched in Fig. 1.

The total intensity I reaching the sensor is the result of the interference between the transmitted field, E_T, and the scattered one E_S: Thus, at any time t we have

$$I(x,y,t) = |E_T(x,y)|^2 + E_T(x,y)E_S^*(x,y,t) + E_T^*(x,y)E_S(x,y,t) + |E_S(x,y,t)|^2 \quad (3)$$

If we assume that the amplitude of the transmitted component is much larger than the scattered one, the last, homodyne term in Eq. (10) can be neglected. Furthermore, since the terms $E^*_S(x,y,t)$ and $E_S(x,y,t)$ are zero-average, by averaging Eq. (3) over different statistical realizations of the speckle field taken at different times, one can recover the stray light background $I_T(x,y)$ associated to the transmitted beam, $I_T(x,y) = \langle I(x,y,t)\rangle_t$. Now, by subtract $I_T(x,y)$ from $I(x,y,t)$, we obtain

$$I(x,y,t) - I_T(x,y) = E_T(x,y)E_S^*(x,y,t) + E_T^*(x,y)E_S(x,y,t) \quad (4)$$

that is the scattered field $E_S(x,y,t)$. It can be shown [4] that, under the NFS conditions discussed above, and assuming the transmitted field $E_T(x,y)$ to be real, by taking the square of the Fourier transform of the right-hand side of Eq. (4) and averaging over time, one obtains the static spectrum of the scattered field $\langle E_S(x,y,t)\rangle_t$, which coincides with the scattered intensity distribution $I(q)$, as it is obtained with the traditional LALS technique.

From the experimental point of view, the main advantage introduced by the heterodyne version is by far the extreme simplicity and compactness of the optical setup that is composed of very common and commercial components. Furthermore, the optics and the sensor have to be just roughly aligned on the laser beam. These features make the technique very easy to be used.

The heterodyne configuration can thus be devised as a novel scattering technique able to provide results that mimic the traditional LALS in a new, easier and reliable way.

4. Optical Setup

We have performed the experiments by using the optical setup sketched in Fig. 1. A cw He-Ne laser (wavelength in the vacuum 6328 A, power 10 mW) has been spatially filtered, shaped and sent onto the sample with a diameter of about 10 mm (values taken at $1/e^2$). The sample was held in a rectangular quartz cell 2 mm long and with walls 1 mm thick, filled with a water suspension of calibrated colloids of various diameters (Duke Scientific Co.) and mixtures.

The data recovery has been performed by a CCD camera and, since in NFS the speckle size is comparable to the scatterer dimensions, a magnifying optics has been necessary to perform measurements of μm sized particles. After testing some microscopes, we devised a 20x Newport (NA = 0.50) as a good choice to perform measurements up to high scattering wavevectors values, the maximum transferred wavevector being about 4.5×10^6 m^{-1}.

5. Rigorous Subtraction of the Stray Light

Here we explicitly show the capability of the technique to subtract a stray light contribution that is much larger than the scattered, without the need for any blank measurement. We prepared a sample containing a monodisperse colloidal suspension of 2 μm polystyrene spheres in water. We compared the power spectra obtained by two measurements, the former obtained with the cell accurately cleaned, the latter with a fingerprint pressed on it. This procedure would dramatically affect any traditional LALS measurement, while the power spectrum obtained with NFS is as good as the one obtained with the cleaned cell. The results are presented in Fig. 2.

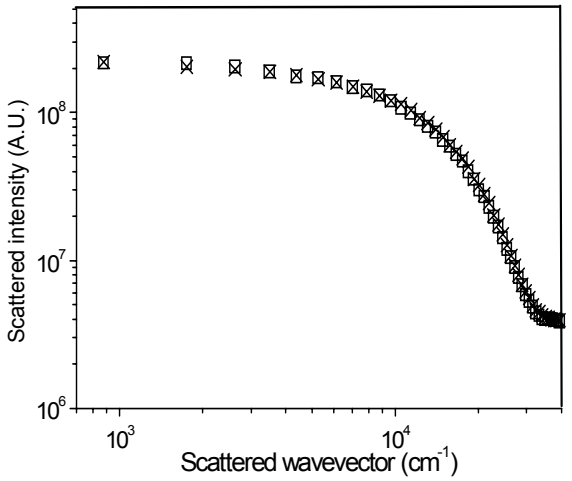

Figure 2: The results of the test for the static stray light subtraction on a sample of monodisperse 2 μm polystyrene spheres. To get this result no blank measurement is necessary. The two curves corresponds to the power spectra respectively obtained with no stray light (crosses) and when the stray light contribution was about the 17% of the impinging intensity (squares). The two curves has been superimposed as explained in the text.

Conclusions

We have briefly recalled the basics of the NFS techniques. The main advantages with respect to the traditional LALS concern the very simple and compact experimental setup, which does not need for precise alignment and mechanical stability, and also the capability to rigorously subtract the static stray light contribution. By contrast, we appreciated a limitation of the technique in performing very fast measurements, since a number of NFS frames have to be recorded.

The results show a good fit to the curves based on the MIE theory, and their smoothness suggests that a good inversion procedure can be performed with traditional algorithms.

All these features suggest that NFS could be considered as a powerful alternative to the traditional scattering techniques to obtain good particle sizing measurements.

References

[1] M. Giglio, M. Carpineti, A. Vailati, "Space intensity correlations in the near field of the scattered light: a direct measurement of the density correlation function", Phys Rev. Lett. **85,** 1416 (2000).

[2] M. Giglio, M. Carpineti, A. Vailati, D. Brogioli, "Near field intensity correlations of scattered light", Appl. Opt. **40**, 4036, 2001.

[3] The system has been patented (D. Brogioli, A. Vailati, M. Giglio, M. Potenza, PCT/IT02/00396, 2002).

[4] D. Brogioli, A. Vailati, M. Giglio, "Near Field Speckles", Appl. Phys. Lett. **81**, 4109 (2002).

Mechanism of Giant Enhancement of Hyper-Rayleigh Scattering in Silver Nanostructures

Corresponding author: E.M. Kim
Co-authors: S.S. Elovikov, D.A. Muzychenko, and O.A. Aktsipetrov
Physics Department, Moscow State University, Moscow, 119992, Russia
E-mail: evgueniay@inbox.ru
Phone: +7-0959393669
Fax: +7-0959391104

Abstract. Hyper-Rayleigh Scattering in optical second harmonic generation was experimentally observed in silver island films. A combined analysis of the nonlinear scattering patterns in combination with the analysis of the results of atomic-force microscopy revealed the fractal nature of the films. Mechanism of giant enhancement in ultradispersed metal systems was observed with the help of dielectric wedge coating a semiconductor substrate layer.

Summary

Hyper-Rayleigh scattering (HRS) in the optical second harmonic (SH) generation, which is, on the one hand, an incoherent analogue of the conventional SH generation and, on the other hand, a nonlinear analogue of the Rayleigh scattering (RS), has been intensively studied in bulk molecular systems starting with the 1970s [1-3]. Later, HRS in the SH generation in molecular systems, i.e., liquids and gases, in which the source of the incoherence was represented by the thermal fluctuations of optical and nonlinear optical parameters of the medium. HRS studies made it possible to develop correlation methods for analyzing the random inhomogeneities of the optical, structural, and morphological properties of the micron-sized and nano-sized objects, such as the microcrystal and polydomain structures of ferroelectric cerami thin films [4], the structural inhomogeneities of the magnetic [5] and ferroelectric [6] Langmuir monolayers, layer-by-layer assembled ferromagnetic films [7], Langmuir fullerene films [8], etc. Recently the surface-enhanced second harmonic generation in ultradispersed metal systems have attracted a considerable interest. The electromagnetic and the molecular-adsorption mechanisms of the surface enhancement have been proposed. In studying the electromagnetic mechanism it is preferable to use surface-enhanced second harmonic generation in the absence of adsorbate because the action of the molecular-adsorption mechanism is excluded.

In this paper, we describe an experimental observation of the HRS in the optical second harmonic (SH) generation in SIF, which serve as a convenient model of a two-dimensional random ensemble of nonlinear scatters. We perform a combined analysis of the nonlinear scattering patterns in combination with the analysis of the results o atomic-force microscopy of the films to study the fine morphological features of the samples. Mechanism of giant enhancement in ultradispersed metal systems was observed with the help of dielectric wedge coating a semiconductor substrate layer, which allowed to select properly the electromagnetic contribution. Variable wedge thickness allowed to change in a controllable way the interaction with the semiconductor substrate layer and thus to vary parameters of the surface plasmon resonance in silver islands.

The silver island films were deposited on a silicon substrate with the (001) orientation by the thermal evaporation technique. The structural properties of the films were studied by an atomic-force microscope in the constant-force regime with a lateral resolution of 30A and a resolution of 4 A along the normal to this plane. A silver island film was evaporated in high vacuum onto a silicon monoxide wedge with thickness d~0-1000 $\overset{0}{A}$. A high quality thermal silicon oxide with thickness of 100nm was grown at 1000 grad onto a standard silicon (001) wafer. A commercially available

buffered NH_4F-etch solution with the etch-speed of 5 nm/min was used to etch the silicon oxide. So we obtain the silicon monoxide wedge. Sample was prepared with 10 different oxide thicknesses ranging from 0 to 1000 $\overset{0}{A}$.

Nonlinear-optical experiments were performed using YAG:Nd^{3+} laser at 1064 nm wavelength and pulse duration of 15 ns. The output ns-OPO laser system was used as a fundamental radiation with wavelength tunable from 490 to 680 nm. The pulse radiation is of 5 ns with the energy of 24 W/cm^2 per pulse and the spot diameter of 5mm. The fundamental radiation was directed onto a sample at an angle of incidence of 45deg. and the SHG signal was selected by filters and detected by PMT.

Figure 1 shows the HRS scattering pattern in the SH generation as a function of the polar scattering angle. The plot demonstrate the appearance of a diffuse incoherent SH component due to the reflection of the laser radiation from the two-dimensional random ensemble of nonlinear scatters. The aperture of the detecting system was 2 deg. for the HRS scattering pattern at the SH. The resulting angular scattering pattern demonstrates the appearance of a broadened scattered component localized in the angular interval 32-58 deg. with the maximum in the specular direction and with a monotonic decrease down to zero outside this interval. The horizontal line separates the regular signal from the diffuse radiation according to the instrumental function of the detecting system.

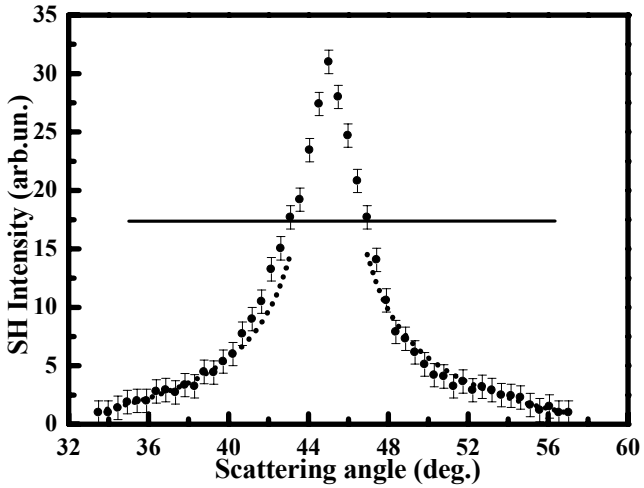

Figure 1.

Figure 2 shows a typical atomic-force microscope image of the surface of a silver island film. One can see that the islands have the form of clusters that are stuck together and have an average size of about 150nm. The system of clusters is a two-dimensional ensemble, because the longitudinal dimension of the particles is much greater than their transverse dimension.

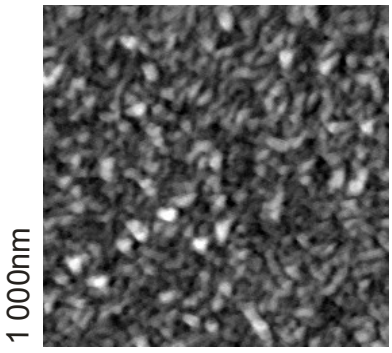

Figure 2.

To determine the correlations between the morphological and nonlinear optical properties of the silver island films from the analysis of the atomic-force microscope images, we constructed the statistical function of the structure, namely, density-density correlation function, which characterizes the correlation of the substance distribution over the sample plane:

$$F(r) = \frac{1}{S}\int n(r+r')n(r')dr'; \qquad n(\vec{r}) = \begin{cases} 1, r \in S^i \\ 0, r \notin S^i \end{cases}$$

S^i- is the space occupied by silver; $n(\vec{r})$ - is the surface density function.

Fig. 3 represents the density-density correlation function for the silver island film. At distances greater than the maximal monomer, function F(r) smoothly decreases and tends to zero. The inset shows the function F(r) on a logarithmic scale for distances greater than 250nm. This dependence was approximated by the power function $1/r^{2-D}$ with the parameter D=1.62, which is represented by the dashed line. Hence the silver cluster structure has the properties of a fractal with the dimension D=1.62.

To interpret the scattering pattern we use the assumption that the correlations of the local optical field factors and the corresponding optical susceptibilities are statistically independent:

$$\Pi\ (r) = A\Pi_{\chi}(r) + B\Pi_{L}(r) + AB\Pi_{\chi}(r)\Pi_{L}(r)$$

where $\Pi_{\chi}(r)$ is the correlation function of the nonlinear susceptibility, $\Pi_{L}(r)$ is the correlation function of the local field factor, A and B are the adjustable parameters. The contributions of quadratic susceptibility can be determined through the silver density function as $\Pi_{\chi}(r) \approx F(r) - \bar{n}^2$. The correlation function of the local optical-field factor can be related to the Fourier transform of the linear scattering pattern: $\Pi_{L}(r) \approx \int I_{\omega}(\theta)J_0[-ikr]kdk$, where $k = \omega(\sin\theta - \sin\theta_0)/c$ and J_0 is the zero-order Bessel function.

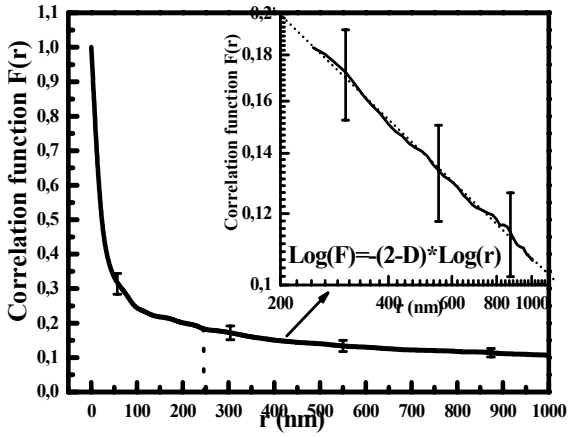

Figure 3.

The general phenomenological expression for the incoherent diffuse HRS signal in the SH generation is as follows:

$$I_{\omega} \approx \int \Pi(r)\exp\{-2i(\sin\theta - \sin\theta_0)\omega e_{II} r/c\}dr$$

The approximation by this formula provides a closer approximation of the HRS scattering pattern in the SH generation in terms of the total square deviation with the parameter D=1.62

(dashed line in Fig. 1). This means that, at large distances the fractal properties is retained with the same exponent D=1.62<2 as in the nanometer range, for which the density-density correlation was calculated.

For the surface-enhanced second harmonic generation intensity we have such equation:

$$I_{2\omega} \sim < \left| \chi^{(2)} L(2\omega) L^2(\omega) \right|^2 > I_\omega{}^2$$

Where $X^{(2)}$ – is the second order susceptibility of nanoparticle material, I_ω - the incident wave intensity, L(w), L(2w) - local field factor at the fundamental and second-harmonic wavelengths describing the local electric field enhancement due to the resonant surface plasmon excitation.

To obtain expression for local field factors we consider an idealized model of the system. We assume silver particles to be flatted spheroids of the same size, shape and orientation, with semi axes a,b. The spheroids form a flat two-dimension array placed into a homogeneous medium at distance d from a silicon substrate. Using Lorentz's mean local field approach in the electrostatic dipole limit (a,b<<d<<l2w) we obtain:

$$L_\alpha(\omega, d) = \left[L_{0\alpha}{}^{-1}(\omega) + P_\alpha(\omega) + Q_\alpha(\omega, d) \right]^{-1}$$

Position of resonances of local field factor is determined by three factors,

1) $L_{0\alpha}(\omega) = [\varepsilon_2 + N_\alpha(x)(\varepsilon_0(\omega) - \varepsilon_2)]^{-1}$ is the local field factor of a single spheroid,

2) $Q_\alpha(\omega, d) = \frac{\pi a^2 b}{6d}\left(-\frac{1}{d} + 4\pi\delta_\alpha \right) \frac{(\varepsilon_1(\omega) - \varepsilon_2)(\varepsilon_{01}(\omega) - \varepsilon_2)}{(\varepsilon_1(\omega) + \varepsilon_2)}$ - term describe the interaction of spheroids with the silicon substrate,

3) $P_\alpha(\omega) = \frac{\pi}{6} \Delta_\alpha nab(\varepsilon_0(\omega) - \varepsilon_2)$ - term describe the interaction of spheroids with each other.

$x = \frac{a}{b}, N_\alpha(x)$ - the depolarization factor,

$\varepsilon_0, \varepsilon_1(\omega), \varepsilon_2(\omega) = const$ - dielectric constants of the spheroids, the layer and the host medium.

$\alpha = \perp, \text{II}$ - the subscript corresponds to the electric field normal (parallel) to the array plane.

In this work we were experimentally determined resonances of local field factor depends on the variable wedge thickness of silicon oxide. So we were observed one of the mechanism of local field factor enhancement – interaction of silver nanoparticles with the silicon substrate.

Fig. 4 shows the second harmonic spectroscopy for different thicknesses of silicon oxide wedge (0, 70, and 100 nm) covered by silver films in interval 490 to 630 nm. One can see increasing of SH signal, wavelength shift in ultraviolet range and narrowing of the half width. Wavelength shift can be attributed to interaction between silver island films and silicon substrate.

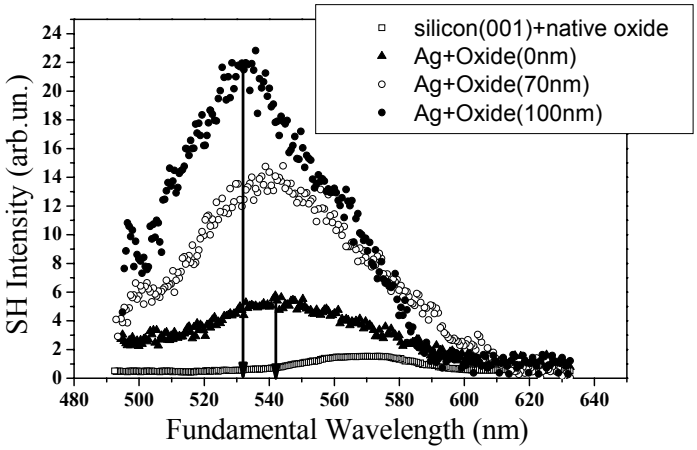

Figure 4.

In conclusion, we were observed HRS scattering pattern on SH and performed a complex analysis of the nonlinear scattering pattern in combination with the results of atomic-force microscopy, which revealed the fractal nature of the films. Mechanism of giant enhancement in silver nanoparticles was observed with the help of dielectric wedge coating a semiconductor substrate layer.

Giant Third-Harmonic Generation in Silver Nanoparticles: New Type of Hyper-Rayleigh Scattering

O.A. Aktsipetrov,[1] S.S. Elovikov,[1] E.M. Kim,[1] M.A. Bader,[2] and G. Marowsky[2]

[1] Physics Department, Moscow State University, Moscow, 119992, Russia
[2] Laser-Laboratorium Goettingen e.V. P.O. Box 2619, 37016 Goettingen, Germany

Summary

Observation of surface-enhanced nonlinear optical effects in silver island films traces back to the early1980's when surface-enhanced optical second-harmonic generation (SHG) and surface-enhanced Raman scattering where observed in the silver island films. The enhancement of the SHG intensity up to three orders of magnitude was attributed to the resonant enhancement of local field factor at the SHG wavelength mediated by local surface plasmon excitation in silver nanoparticles. Important aspect of the surface-enhanced SHG from the silver island films is the strong incoherency of the SHG radiation, which manifest itself throw the strong diffuseness and depolarization of the SHG radiation. The silver island films being 2-D random arrays of randomly shaped nanoparticles possess the spatial fluctuations of the second-order nonlinear susceptibility and local optical field factors. These result in fluctuations of quadratic nonlinear polarization, which are the sources of incoherent SHG, in other words the second-order hyper-Rayleigh scattering (HRS) at the SH wavelength. Strongly enhanced and diffuse SHG from rough silver films has been intensively studied since early 1980's.

In this paper, giant incoherent optical third-harmonic generation (THG) is observed in silver island films. The THG intensity from two-dimensional random array of silver nanoparticles is enhanced by two orders of magnitude. This enhancement is attributed to the local field resonance at third-harmonic wavelength mediated by excitation of the local surface plasmons in silver nanoparticles. Giant THG observed is strongly diffused and depolarized, which is clear manifestation of the third-order hyper-Rayleigh scattering in 2-D random ensemble of silver nanoparticles.

Silver films were prepared by thermal evaporating, at a rate of 3-4 A/s, in vacuum of 10^{-5} Torr onto substrate of silicon Si(001) wafers. Silicon wafers are used as substrate for almost ideal flatness of its surface. Silver films are characterized by mass thickness. Two types of samples are used in the nonlinear optical experiments: the silver island film samples with mass thickness of approximately 1 nm and thick homogeneous silver films with mass thickness of 40 nm. The choice of mass thickness of the silver island film samples is crucially important for observation of surface-enhanced THG as mass thickness of 1 nm corresponds to the UV resonant wavelength of local surface plasmons. Thick homogenous silver films are used as the reference samples for measurement of enhancement of the THG intensity from silver island films with respect to nonenhanced THG responses from flat metal surface.

Nonlinear-optical experiments were performed using YAG:Nd^{3+} laser at 1064 nm wavelength and pulse duration of 15 ns. The output ns-OPO laser system was used as a fundamental radiation with wavelength tunable from 490 to 680 nm. The fundamental radiation was directed onto a sample at an angle of incidence of 45deg. and the SHG signal was selected by filters and detected by PMT.

Figure 1 shows the azimuthal dependencies of the THG intensity from (1) silicon wafer (001), (2) SI film and (3) thick flat reference silver film. All these azimuthal dependences are measured in s-in, s-out geometry. One can see the isotropic component of THG intensity from silver island film on silicon wafer is strongly enhanced with respect to isotropic component of THG intensity from

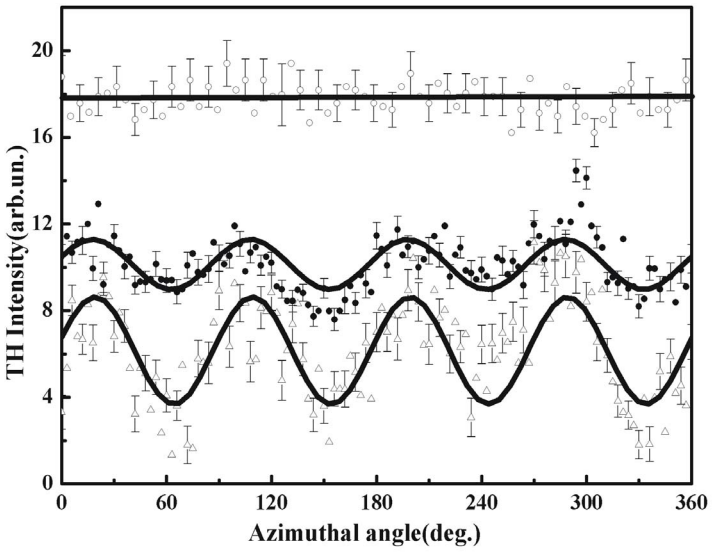

Figure 1.

silver free silicon wafer, whereas the anisotropic component of the THG intensity from island film is noticeably decreased as compared to the third-harmonic generation from silicon surface. Comparing the isotropic component of the THG signal from thick flat silver with the isotropic component of the THG signal from silicon (001) one can obtain the enhancement of THG in silver nanoparticles.

For correct measurements of the surface enhancement of the THG intensity from island films we must know the diffuseness of THG. Open symbols in Figure 2 shows scattering pattern: dependence of incoherent THG intensity on the polar scattering angle, for the third order HRS. The plot demonstrates the appearance of a diffuse THG component due to the reflection of the laser radiation from the two-dimensional random ensemble of nonlinear scatters. The aperture of the detecting system was 2 deg. for the HRS scattering pattern at the THG wavelength. The resulting angular scattering pattern demonstrates the appearance of a diffuse scattering component localized in the angular interval 41-49 deg. with the maximum in the specular direction at 45 deg. and with a monotonic decrease down to zero outside this interval. The insert in Figure 1 shows conventional (linear) Rayleigh scattering of light at the same wavelength as THG radiation. This very specular Rayleigh scattering pattern mostly originates from reflection of light from flat silicon surface. Solid symbols in Figure 1 show scattering pattern for the THG from flat silicon surface, which show spectacular peak with intensity that is noticeably smaller than the HRS intensity integrated over the total interval of HRS scattering angles.

For quantitative measurement of enhancement one has to take into account both integration of the THG signal over scattering pattern and over the thickness of silver layer where nonlinear sources are localized in island films and reference thick film. Correct integrations give the enhancement in nanoparticle silver films of more than two orders of magnitude.

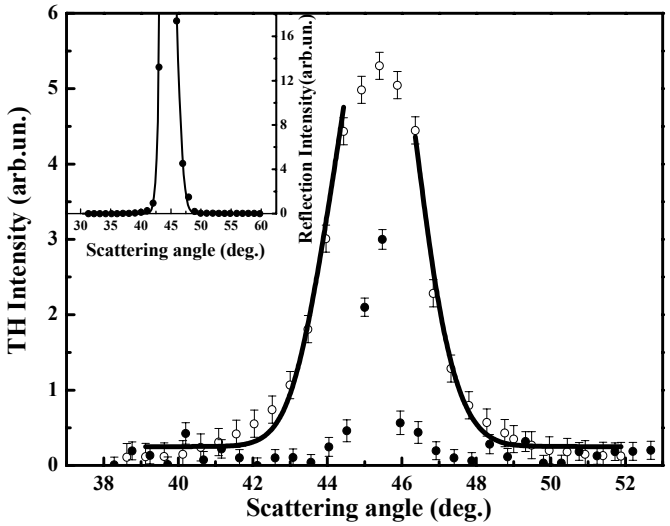

Figure 2.

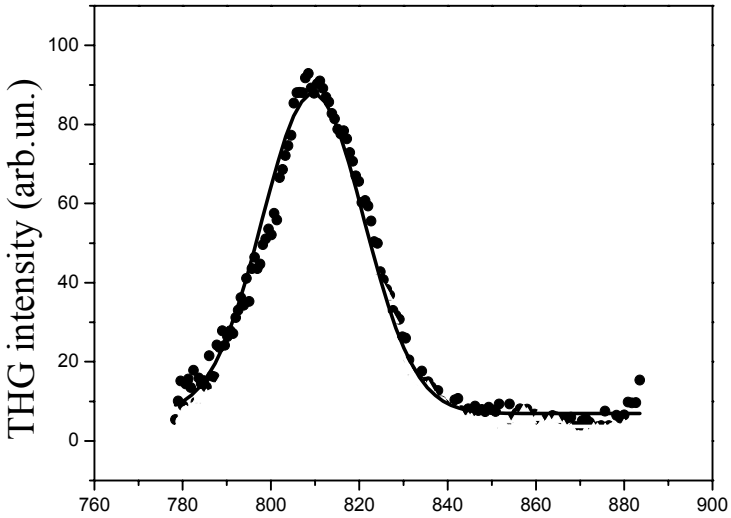

Figure 3.

Figure 3 shows spectral dependence of the THG intensity from silver nanoparticle films as a function of fundamental wavelength, which is measured with tunable output of OPO laser system. THG intensity demonstrates the sharp spectral peak centered in the vicinity of 810 nm for fundamental wavelength. This spectral peak can be attributed with excitation of local surface plasmons in the array of silver islands. This allows us to associate the mechanism of giant THG with resonant enhancement of local optical fields in random ensample of metal nanoparticles.

In conclusion, surface-enhanced optical third-harmonic generation (THG) is observed in silver island films. The THG intensity from two-dimensional (2-D) array of silver nanoparticles is enhanced by two orders of magnitude and the enhancement is attributed to the local field resonance at third-harmonic wavelength mediated by excitation of the local surface plasmons. Incoherent: diffuse and depolarized, component of the enhanced THG intensity is associated with the third-order hyper-Rayleigh scattering (HRS) in 2-D random ensemble of silver nanoparticles.

A near-field microwave microscope and electron spin resonance detection

J. Adin Mann, Jr., j.mann@case.edu
Department of Chemical Engineering

Massood Tabib-Azar, mxt7@case.edu
Department of Electrical Engineering and Computer Science
Case Western Reserve University
Cleveland OH 44106

Abstract

Microwave photons can image a surface using near-field geometry. Spatial resolution is on the nanometer length scale. Moreover, it is possible to detect electron spin resonance splitting caused by a small permanent magnet positioned close to the surface containing a free radical moiety.

1 Near-field microwave microscopy

The operation of the near-field, scanning optical microscope (NSOM) is well explained in the literature and involves the properties of evanescent waves of light-fields of wavelengths in a range around 500nm. In fact, evanescent wave effects have been generated in the common microwave bands. A recent paper from here [1] shows how to build a scanning, near-field, microwave microscope (SNMM) with probes that allow the simultaneous collection of image data from cantilever flexing (scanning force microscopy) and from an evanescent microwave wave field interacting with the surface and near-surface. SNMM has the advantage that the penetration depth of the field can be controlled, through the frequency of the microwave field and thereby probe the structure of the near-surface region. The combination of techniques is a very powerful surface structure tool with resolution on the nanometer length scale.

2 Electron spin resonance

We focus on a new application of the SNMM technology, which is based on the fact that the classical X-band and Q-band of microwave photon fields allow the resolution of electron spin spectra split by a modest magnetic field.(ESR or EPR). Many of the applications we expect to explore involve macromolecules that have been "spin labeled." The term “spin label” refers to a stabilized free

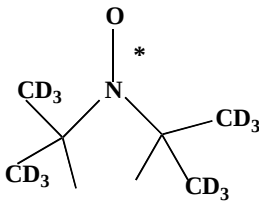

Figure 1: The stabilized free radical, nitroxide moiety, replacing H atoms with D. Also ^{14}N may be replaced by ^{15}N. T_2, the spin-spin relaxation time, is thereby longer and is a candidate for spin-nets for quantum computing. Denote this moiety by "DOXYL."

radical, Fig. 1, which for the purpose of this summary will be taken as a nitroxide moiety based on TEMPO (2,2,6,6-tetramethylpiperidinyloxy) that also can be used as a preparative reagent.

The synthetic chemistry of spin labels is very rich so that it is possible to prepare spin labels with lipids in general as well as proteins. In particular it is possible to spin label diacetylene molecules of the class of 10,12-nonacosadiynoic acid (16-8 DA) monomer, $CH_3(CH_2)_{15}$-C≡C-C≡C-$(CH_2)_8$COOH, which will form excellent Langmuir monolayers and Langmuir Blodgett (LB) multilayers and can be polymerized *in situ*. These deposited monolayers will be studied with the SNMM so as to evaluate T_1, the spin-lattice relaxation time and T_2 the spin-spin relaxation time *locally*.

Analogous spin label molecules spread as Langmuir monolayers on a tiny quartz trough that was inserted into the microwave cavity of a Varian ESR spectrometer were studied by us many years ago. Spin exchange effects were observed on these monolayers, even with the rather limited analog ESR systems available at the time. Clearly, ESR techniques are sufficiently sensitive that low surface-density monolayers can be studied.

3 Near-field microwave microscopy of free radical spins

The instrument developed in the Case Polymer Molecular Devices Laboratory for detecting electron spins involves adding a small permanent magnet to the SNMM system designed and built by Tabib-Azar [1] and his group, fig. 2.

In an early experiment, a ruby file 1mm^3 was subjected to a 0.2 Tesla field and we measured a shift, of 20 MHz from the center frequency of 4GHz with an excellent signal to noise ratio. We are experimenting with smaller samples and believe, from this data, that a very small number of spins will be detectable. An example of the effect is shown in fig 3.

Our ability to “engineer” the physical extension of decaying microwave fields by choosing appropriate waveguide substrate, tapering angle, and tip geometry enables optimization of the probe’s operation frequency and its lateral spatial resolution separately. The penetration of the electromagnetic fields inside the sample constitutes the probe’s perpendicular resolution that is determined by the skin-depth or the perpendicular decay constant, whichever is shorter. The results to date suggest that single spin resolution can be achieved in nanometer length scales.

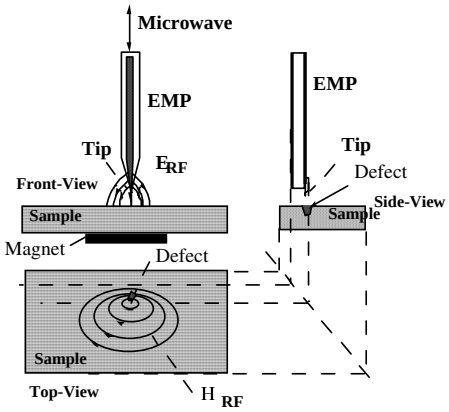

Figure 2: Schematic of the electron spin resonance sensor using the evanescent microwave probe of Reference[1]. The Magnetic field H_{dc} normal to the surface is provided by a small magnet (modulated) placed under the sample. Unpaired electron's energy levels split by an externally applied magnetic field (Zeeman effect). Absorption of energy, $\hbar\omega$, from the electromagnetic field provides the spectrum.

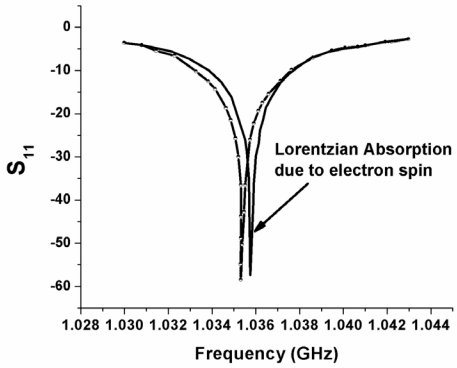

Figure 3: Modification of S_{11} spectrum detected by the evanescent microwave probe (EMP) due to electronic spin flipping transitions near the EMP tip.

4 Reference

[1] Massood Tabib-Azar and Yaqiang Wang, "Design and fabrication of scanning near-field microwave probes compatible with atomic force microscopy to image embedded nanostructures," IEEE Trans. Microwave Theory and Techniques, **52**(3), 971-979 (2004).

Session 6
Fluctuations in Fluids

TuB 11:10–12:50
Tinbergen Room

Anthony Smart, *Chair*

Smectic Membranes in Motion: The Limits of X-Ray Photon Correlation Spectroscopy

Wim H. de Jeu
FOM-Institute AMOLF
Amsterdam, The Netherlands

In the first part I shall summarize results we reported recently of low-dimensional fluctuations in smectic liquid crystal membranes [1] in the range of 10 ns to 10 μs using both x-ray photon correlation spectroscopy (XPCS) and neutron spin echo (NSE) [2]. XPCS probes surface tension-dominated relaxation times. In this regime, fluctuations with long wavelengths reveal an oscillatory damping, while fluctuations with a shorter wavelength show a simple exponential decay. NSE reveals a new regime, determined by bulk elasticity, in which the fast relaxation times decrease with the wave vector.

In the second part I will discuss several practical aspects and limitations we encountered during our XPCS studies. Coherence effects differ from the situation in classical dynamic light scattering and can influence the time dependence of the correlation function. Variation of the detector slits as well as of the projected coherence length on the membrane induces a change in the correlation a time. Finally heterodyne detection occurring at the specular ridge and homodyne detection at off-specular positions, will be discussed.

References

[1] W.H. de Jeu, B.I. Ostrovskii, A.N. Shalaginov, Rev. Mod. Phys. **75**, 181 (2003).
[2] I. Sikharulidze, B. Farago, I.P. Dolbnya, A. Madsen, W.H. de Jeu, Phys. Rev. Lett. **91**, 165504 (2003).

GRADFLEX, Fluctuations in Microgravity

A. Vailati, R. Cerbino, S. Mazzoni, and M. Giglio
Istituto Nazionale per la Fisica della Materia and Dipartimento di Fisica, Università degli Studi di Milano
Via Celoria 16, 20133 Milano, Italy, Phone: +39 02 50317223, Fax: +39 02 50317712,
E-mail: vailati@fisica.unimi.it

G. Nikolaenko and D. S. Cannell
Department of Physics, University of California at Santa Barbara, Santa Barbara, CA, USA

W. V. Meyer
NCMR / NASA Glenn Research Center, Cleveland, OH, USA

A. E. Smart
Costa Mesa, CA, USA

Abstract: We present the results of experimental investigations of gradient driven fluctuations induced in a liquid mixture with a concentration gradient and in a single-component fluid with a temperature gradient. We also describe the experimental apparatus being developed to carry out similar measurement under microgravity conditions.

The GRAdient Driven FLuctuation EXperiment (GRADFLEX) involves the investigation of fluctuations induced in simple fluids and in binary mixtures by imposing a macroscopic temperature or concentration gradient under microgravity conditions. Recent experiments have shown that giant nonequilibrium fluctuations are present during diffusion processes in liquid mixtures and in the presence of a heat flux through a fluid. These fluctuations occur at all length scales between the microscopic and a macroscopic scale set by the sample dimensions. The fluctuations are due to corrugations in the diffusing front, whose fractal properties explain the presence of fluctuations involving all length scales. The fluctuations are generated by coupling between velocity fluctuations and the macroscopic gradient (concentration or temperature) which drives the flux. The amplitude of these fluctuations diverges as q^{-4}, where q is the wave vector of the fluctuation. Long wavelength fluctuations are stabilized by gravity, which quenches the q^{-4} divergence at the smallest wave vectors.

On Earth, gravity suppresses the long wavelength fluctuation below a typical cutoff wave vector. The aim of the GRADFLEX project is to investigate these fluctuations in the absence of gravity, where the long wavelength fluctuations are no longer predicted to be stabilized by gravity, and to compare the results with those obtained on Earth. Many materials science processes (for example, crystallization and growth of materials) are performed in microgravity because of advantages expected from the absence of convection. However, the presence of nonequilibrium fluctuations could lead to the unexpected presence of large scale inhomogeneities that could impair processing under microgravity conditions.

Two prototype systems to guide the engineering of flight hardware have been developed, one in the Optics and Microgravity Laboratory at the University of Milan by the Istituto Nazionale per la Fisica della Materia (INFM) and one in the Physics Department at the University of California at Santa Barbara (UCSB). Both systems use the shadowgraph method to measure the fluctuations. The system developed at INFM is devoted to the investigation of concentration fluctuations occurring during a Soret induced mass diffusion process, while that developed at UCSB is designed to investigate fluctuations induced by a thermal gradient in a single-component fluid. The project is scheduled for flight in 2006 onboard the Russian satellite capsule FOTON M3.

The current sensitivity of the shadowgraph method is now sufficiently developed to measure the scattering from the fluctuations, both on Earth and in microgravity. Samples are contained between parallel sapphire windows to provide the necessary thermal boundary conditions. The fluctuations give rise to phase perturbations in the wavefronts of a beam of light passing through the sample, resulting in measurable intensity modulation a sufficient propagation distance beyond the sample. This intensity modulation is time-dependent, and it can be analyzed to obtain both the mean squared amplitude of the fluctuations $S(q)$, and their power spectrum $S(q,\omega)$, for wave vectors as small as 20 cm^{-1}. Thus the method is useful well below the range where small angle light scattering is typically

impossible because of stray light and other effects. The resulting data are the product of $S(q)$ and the shadowgraph transfer function $T(q) = \mathrm{Sin}^2\,(q^2 z/2k_o)$.

We will present experimental results obtained on Earth for both $S(q)$ and $S(q,\omega)$ for polystyrene diffusing in toluene (INFM), and for thermal fluctuations in carbon disuphide (CS_2) with a temperature gradient (UCSB). We will also describe our current designs for the flight qualified measuring systems. Some examples of the data we have been able to obtain for $S(q)$ and $S(q,\omega)$ for the two systems on Earth are shown below.

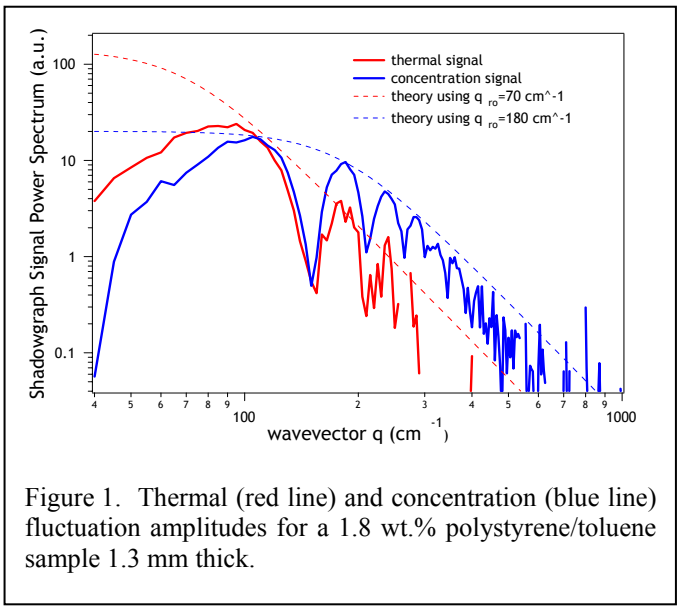

Figure 1. Thermal (red line) and concentration (blue line) fluctuation amplitudes for a 1.8 wt.% polystyrene/toluene sample 1.3 mm thick.

Figure 1 shows results for $T(q)S(q)$ for a 1.3 mm thick sample consisting of 1.8 wt.% of 9100 M_W polystyrene in toluene. The thermal and concentration fluctuations were measured separately in the following manner. A temperature gradient of 135 K/cm was applied during about 120 s, after which the thermal gradient was fully established, while the concentration gradient caused by the Soret effect had only begun to develop, because the relevant time constant is about 940 s. A set of 100 images taken at the rate of 1/s in the interval between 140 s and 240 s after beginning to establish the gradient were analyzed to obtain the results for thermal fluctuations. A similar set of images taken 6900 s after the start of the experiment were analyzed to obtain the results for the concentration fluctuations.

Theoretically, the thermal fluctuations should be quenched by gravity only below about 70 cm^{-1}, and the dashed curve for $S(q)$ shows that the data are quite consistent with this prediction. For concentration fluctuations the relevant wave vector is predicted to be about 226 cm^{-1}, while the data seem more consistent with a value of about 180 cm^{-1} as shown by the dotted curve for $S(q)$ for the concentration fluctuations.

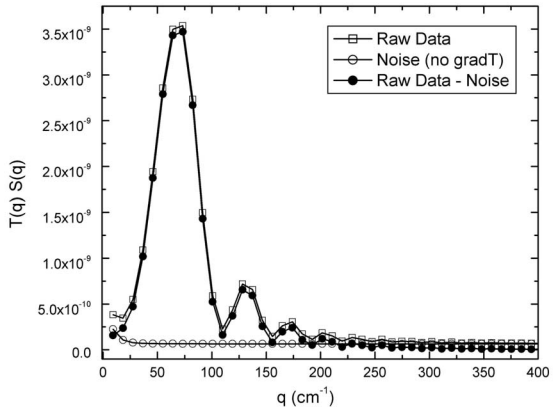

Figure 2. The spatial power spectrum of gradient driven fluctuations in a 2.7 mm thick sample of CS_2 measured using the shadowgraph method with a visualization distance of 51 cm.

Figure 2 shows results for $T(q)S(q)$ for a CS_2 sample. The data were obtained with a 23 K temperature difference applied across the 2.7 mm thick sample, which was held at a mean temperature of 32.5œC. The upper surface of the sample was hotter than the lower surface thus preventing any convective motion. Before applying the gradient we measured a background spectrum (open circles), primarily caused by camera noise, and this spectrum was subtracted from the spectrum measured with the gradient applied (open squares) to obtain the result shown by the solid circles. A total of 4000 images taken at 2 second intervals were analyzed to obtain the results shown. As can be seen, the amplitude of the fluctuations grows strongly with decreasing wave vector. Although the appearance of the data is complicated by the presence of the shadowgraph transfer function, this is not much of a problem in practice, because the data can be fit readily by the product $T(q)S(q)$.

The project is being carried out by INFM in collaboration with UCSB. The ground based research is being jointly supported by ASI and NASA. The flight hardware and flight expenses will be supported by ESA.

Dynamics of Gradient Driven Fluctuations in a Free Diffusion Process

Fabrizio Croccolo[1], Doriano Brogioli[2], Alberto Vailati[1], David S. Cannell[3] and Marzio Giglio[1]
[1]*Dipartimento di Fisica and Istituto Nazionale per la Fisica della Materia, Università di Milano, Via Celoria 16, Milano 20133, Italy*
[2]*Dipartimento di Biologia, Università di Milano, Via Celoria 26, Milano 20133, Italy*
[3]*Department of Physics and iQUEST, University of California, Santa Barbara, California 93106, USA*
e-mail: fabrizio.croccolo@fisica.unimi.it - tel.: +39-02-50317211 - fax: +39-02-50317712

Abstract: We measure fluctuations' dynamics in a free diffusion process applying a new processing to Shadowgraph images to get temporal correlation functions. These functions appeared as decaying exponentials with characteristic time τ depending on q vector.

1. Introduction

Diffusion is commonly believed to be a homogeneous process at the mesoscopic and macroscopic scale. On the contrary giant fluctuations are always tied with diffusive processes. This has been experimentally shown in a variety of samples and configurations [1-3]. A theory, based on fluctuating hydrodynamics, has been developed for the calculation of the structure factor of time dependent Gradient Driven Fluctuations (GDF) [4]. The amplitude of fluctuations diverges like q^{-4} as the wave vector q gets smaller. In the presence of gravity, this divergence is prevented for wave vectors smaller than a characteristic one, $q_{roll\text{-}off}$. Gravity stabilizes long-wavelength fluctuations.

Theory predicts that the temporal correlation function of GDF is an exponential decay with a time constant τ depending on q. τ is predicted to exhibit a slope $1/(Dq^2)$ for $q>q_{roll\text{-}off}$ showing a diffusive decay behaviour. For $q<q_{roll\text{-}off}$ τ should have a slope q^2 thus demonstrating that for these q values buoyancy force becomes faster than the diffusive process. The combination of these two slopes gives a maximum τ at $q_{roll\text{-}off}$. Dynamic measurements on GDF are commonly made by dynamic light scattering experiments, but the traditional set-up doesn't allow achieving very low scattering angles.

Shadowgraph is used as a quantitative technique to investigate the static power spectrum of GDF for its high sensitiveness at very low q vectors [3]. We present here a technique through which we get the time correlation function of the sample by analysing time dependent power spectra obtained from sequences of images grabbed with a fixed delay time. With this technique the time correlation functions of GDF are determined and evidence is given that they are decaying exponentials with characteristic time τ depending on the q vector.

2. Experimental procedure

The investigated sample is a binary mixture of water and diluted glycerol (40% w/w) undergoing a free-diffusion process due to the presence of an initial macroscopic density gradient generated by carefully layering the two fluids in the experiment cell.

The optical set-up is a typical Shadowgraph one with a superluminous diode generating a quasi-monochromatic diverging beam which is collimated by a lens to give a plane beam of about 2 cm at e^{-2}. The beam passes through the sample recording little phase modulations which are transformed into intensity one on a screen plane at a z distance from the sample plane. This plane is imaged on a CCD sensor through a lens which provides the magnification we need to analyse the desired q vectors.

3. Dynamical processing

In order to calculate the static power spectrum from a sequence of Shadowgraph images a background image is needed to subtract from all images. Two common ways of simulating the background image are either to average all images or to subtract each image to the previous one. In the latter scheme a time-dependent power spectrum is actually calculated which can be demonstrated to be:

$$S_2(\vec{q},\Delta t) = 2S_1(\vec{q}) - 2C(\vec{q},\Delta t)$$

in which $S_2(\vec{q},\Delta t)$ is the time-dependent spectrum, $S_1(\vec{q})$ is the conventional static power spectrum, while $C(\vec{q},\Delta t)$ is the temporal correlation function. The temporal correlation function can be easily calculated by subtracting the time-dependent spectrum to the conventional static power spectrum.

4. Data analysis

We analysed the above mentioned sample and measured its correlation functions over a wide range of q vectors ranging from the unconventional low value of 30 cm^{-1} to 400 cm^{-1}.
Correlation functions of GDF appeared to be exponential decays within two decades with time constants τ depending on q vector.
The dependence of τ against q is consistent with the theoretical prediction and both the $q_{roll\ off}$ value and the coefficient diffusion can be derived from this measurement.

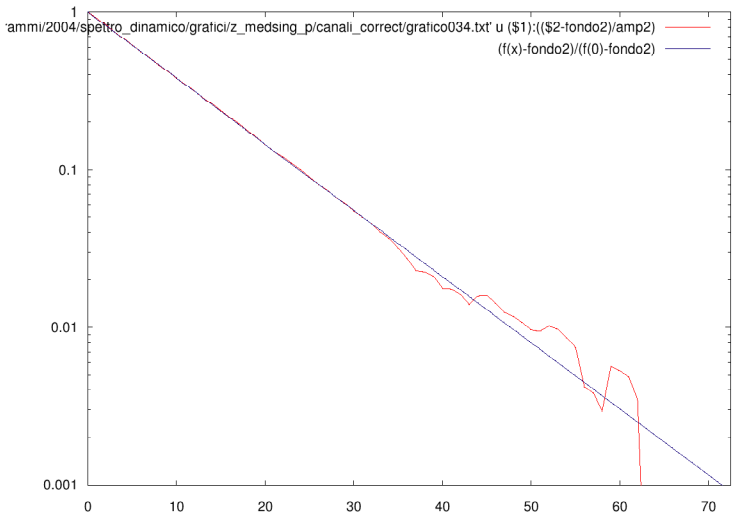

Fig.1. Exponential decay of GDF and corresponding fitting function.

[1] Law, Gammon and Sengers, "Light-scattering observations of long-range correlations in a nonequilibrium liquid," PRL **60**, 1554-1557 (1988).
[2] Vailati and Giglio, Giant fluctuations in a free diffusion process, Nature **390**, 262-265 (1997).
[3] Brogioli, Vailati and Giglio, "Universal behaviour of nonequilibrium fluctuations in free diffusion processes," PRE **61**, R1-R4 (2000).
[4] Vailati and Giglio, "Nonequilibrium fluctuations in time-dependent diffusion processes," PRE **58**, 4361-4371 (1998).

Surface response functions for a thin-film between fluids with infinite boundaries and for a fluid-fluid interface between finite boundaries

William V. Meyer[1], J. Adin Mann, Jr.[2], and Gerard H. Wegdam[3]

[1]*NASA Glenn Research Center, National Center for Microgravity Research*
M.S. 110-3, 21000 Brookpark Road, Cleveland, OH 44135-3191, USA

[2]*University of Amsterdam, Van der Waals-Zeeman Institute, Valckenierstraat 65,*
NL-1018XE Amsterdam, The Netherlands

[3]*Case Western Reserve University, Department of Chemical Engineering*
10900 Euclid Avenue, Cleveland, OH 44106-7217, USA

Correspondence should be directed to WVM, Telephone: (216) 433-5011,
Email: William.V.Meyer@GRC.NASA.Gov

Abstract: A simplified surface response function is presented for interfaces with a thin-film between two fluids of infinite extent; and the newly derived results for the surface response function of a fluid-fluid interface between finite boundaries is presented.

Introduction

The previously published solution [1] of the surface response function (SRF) for the interfaces of a thin-film between two fluids of infinite extent has been further simplified and shown to reduce to the simple fluid-fluid interface solution when the film thickness goes to zero. This mathematical reduction of several hundred pages to a single page of equation components will be published in the full paper. This abstract, due to space limitations, presents the resulting 3-D parametric plot in Figure 1 of the power spectra that result from the surface response function that is plotted as a function of film thickness and frequency. For the conference presentation, a movie showing how this 3-D plot changes for different scattering angles, **q**, will be presented. This new SRF solution is now simple enough that a fast computer can use it to fit actual surface light scattering data, such as that which we have presented elsewhere [1 - 3]. This empirical data looks visually akin to the theory plots combined in Figure 1. When using the full thin-film SRF presented here for analyzing surface light scattering data (along with the instrument function we provide elsewhere [1, 3]), surface properties such as surface tension and viscosity are now directly manifested. And when solving the SRF; one no longer has to ask which root of the dispersion equation provides the correct answer. These solutions, which include both the normal and tangential interface components, work for underdamped, critically damped and overdamped systems. These developments can be used to characterize systems with liquid–vapor and liquid–liquid interfaces including spreading monolayers, whenever optical access for a laser beam is available.

Building on the ideas presented in Mann, et al. [4], Meyer has also derived a surface response function for a fluid-fluid interface between finite boundaries. The full analytical results, which reduce hundreds of pages of derivation to a page of results, due to space limitations, will be published in the full paper. The resulting 3-D parametric plot for a liquid-liquid interface is shown in Figure 2, and for a liquid-vapor interface in Figure 3. Notice how the pentane-water interface for Figures 2 and 3 look like that of the pentane-water (liquid-liquid) thin-film interface shown in Figure 1, with the curve for the liquid pentane-pentane vapor interface now absent and no longer visible in the power spectra. In Figures 2 and 3, each individual 3-D parametric plot shows the predicted power spectra as a function of fluid thickness (with respect to the solid boundary) and frequency. Again, movies for each of these SRFs that show how power spectra vary with the scattering angle, **q**, will be presented.

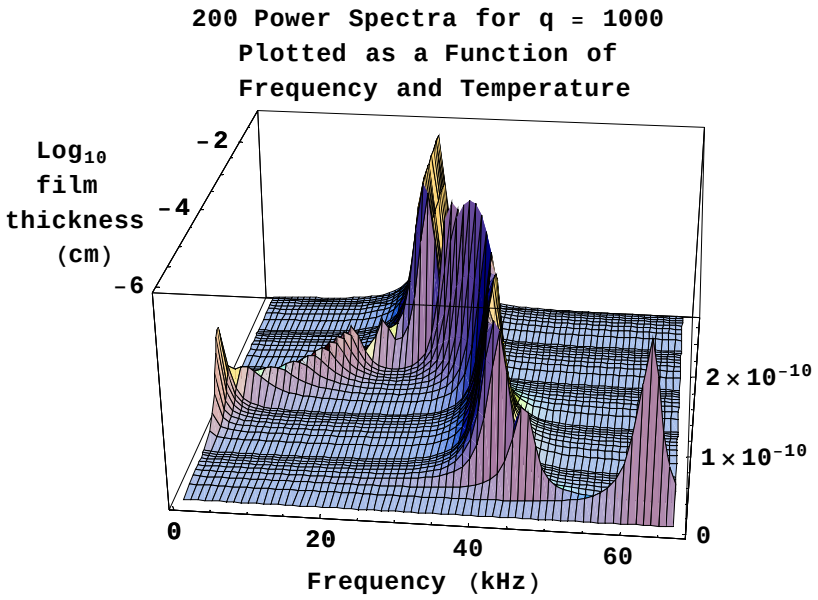

Figure 1. Calculated power spectra at the liquid-liquid water-pentane interface. The temperature in the calculation was held at 45°C and the lower (water) boundary was placed at infinity. A van der Waals term with a Hamaker coefficient of -4.5 x 10^{-22} J was used in the calculation and skews the power spectrum to the right as the film becomes very thin (i.e. ~10^{-6} cm).

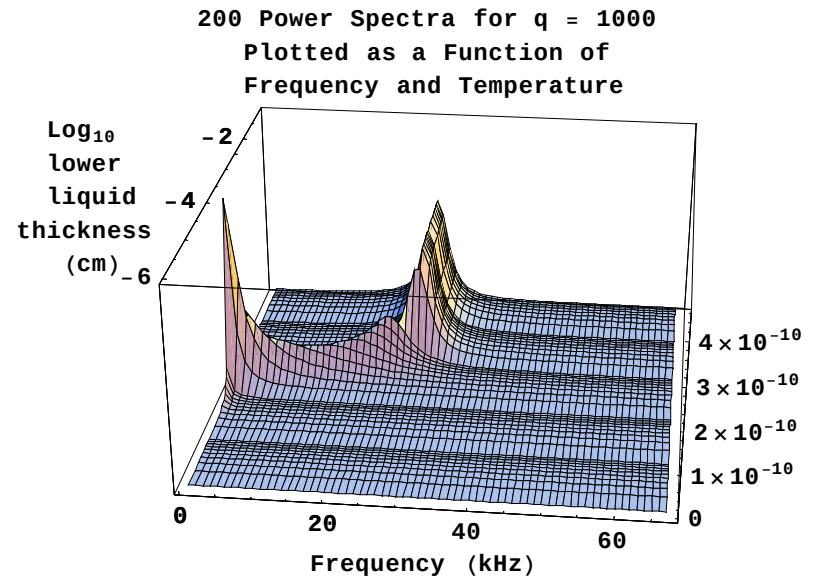

Figure 2. Calculated power spectra at the liquid-liquid water-pentane interface. The temperature in the calculation was held at 45°C and the lower (water) and upper (pentane) liquid layers are contained by a solid lower and upper boundary. The thickness of the lower and upper liquids combined is 0.09 cm and the thickness of the lower liquid layer is shown in the plot.

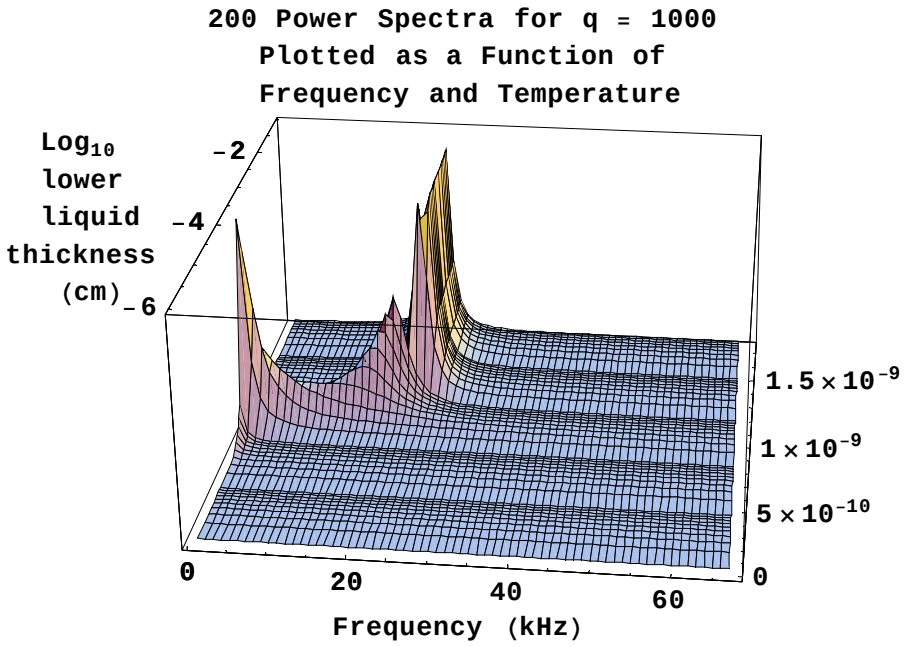

Figure 3. Calculated power spectra at the liquid-vapor pentane-pentane interface. The temperature in the calculation was held at 45°C and the lower and upper (pentane) liquid-vapor layers are contained by a solid lower and upper boundary. The thickness of the lower and upper fluids combined is 0.09 cm and the thickness of the lower liquid layer is shown in the plot.

References

[1] William V. Meyer, Gerard H. Wegdam, Denis Fenistein, J.Adin Mann, Jr., "Advances in surface-light-scattering instrumentation and analysis: noninvasive measuring of surface tension, viscosity, and other interfacial parameters," Appl. Opt. 40, 4113-4133 (2001).

[2] Denis Fenistein, Gerard H. Wegdam, William V. Meyer, and J. Adin Mann, Jr., "Capillary waves on an asymmetric liquid film of pentane on water", Appl. Opt. 40, 4134-4139 (2001).

[3] William Vernon Meyer, "Volume and Interface Studies of Complex Liquid Media," Ph.D. thesis (includes a 129 MB CDROM of derivations, a volume and surface light scattering data analysis program, data sets, 3-D plots, etc.), University of Amsterdam, The Netherlands, December 13, 2002.

[4] J. Adin Mann, Jr., Paul D. Crouser, and William V. Meyer, "Surface fluctuation spectroscopy by surface light scattering spectroscopy," Appl. Opt. 40, 4092-4112 (2001).

Session 7
Photon Scattering

WA 9:00–10:20
Tinbergen Room

Aristide Dogariu, *Chair*

Correlation Spectroscopy With Coherent X-Rays

Gerhard Grübel
Deutsches Elektronen-Synchrotron DESY, HASYLAB
Notkestrasse 85, 22607 Hamburg, Germany

X-ray photon correlation spectroscopy (XPCS) is a novel technique for the study of slow dynamics in disordered materials. It overcomes limitations of visible light scattering techniques such as multiple scattering or limitations in Q-range by using coherent X-rays from third generation synchrotron radiation sources. Applications to the static and dynamic behavior of complex fluids and to slow dynamics in hard condensed matter systems are reviewed.

Using Diffusing-Wave Spectroscopy to Study Intermittent Dynamics

Régis Sarcia and Pascal Hebraud
P.P.M.D. CNRS UMR 7615 ESPCI 10 rue Vauquelin 75231 Paris Cedex 05
regis.sarcia@espci.fr and pascal.hebraud@espci.fr

Abstract: A new scheme of diffusing-wave spectroscopy is used to study the intermittent dynamics that occurs when a concentrated suspension flocculates. Crackling events are detected and their statistical properties analyzed.

Many concentrated systems share common dynamical properties. Their dynamics exhibit two distinct characteristic times: the slowest is associated with the structural reorganization of the microscopic components. It generally increases when time flows: the system ages [1]. Moreover, recent experiments have shown that this slow relaxation time exhibits intermittent dynamics when the system ages [2] [3]. We are here interested in the dynamics of a concentrated colloidal suspension. In the case where inter-particles interactions become attractive, the system flocculates, and the intermittent dynamics effects are enhanced. We thus develop a new diffusing light scheme to analyze the statistical properties of these experiments. In the first part we present a multispeckle diffusing wave spectroscopy experiment in which fluctuations of diffused light are fully computed. We introduce a past-future representation in which intermittency naturally appears. Applying this technique to the flocculation of concentrated suspensions, we show the existence of crackling events, whose dynamics we characterize.

1. 2D-MSDWS

Diffusing-wave spectroscopy (DWS) is a dynamic light scattering technique that applies to very turbid systems. It has been used to monitor short time dynamics of the particles during coagulation [4]. These systems exhibit two distinct relaxation times. As expected, the amplitude of the faster one decreases while the suspension flocculates. Nevertheless, in order to understand the low frequency mechanical properties of the system, the long-time rearrangements that occur while the system is flocculating, need to be monitored. Standard DWS technique implies a running averaging over time and does not fulfill this task. Multispeckle DWS (MSDWS) may overcome this difficulty by averaging diffusing light over different speckles [5] [6]. In this technique, temporal correlation functions are computed, starting from a given speckle image, at some instant. It leads to a snapshot of the dynamics at a given time, but does not allow an accurate description of intermittent dynamics observed in concentrated colloidal dispersions. Recent advances have recently been proposed to analyze intermittent dynamics [3] [7]. The last one studies non-gaussian character of diffused electric field. It requires extensive averaging and is not available to our non-stationary system. The former one lies on the study of the fluctuations of the correlation of two images separated by a constant time lag, and, as discussed later in the text, does not allow to identify speckle images responsible for the heterogeneous dynamics. We thus introduce a new light scattering scheme, where temporal fluctuations are fully computed, and that we call 2-dimension multispeckle diffusing wave spectroscopy (2DMSDWS).

With this advance, we are able to describe the temporally heterogeneous dynamics of the particles, with a time resolution of 6Hz, and the spatial resolution of DWS ~10nm.

The turbid sample is enlightened with an enlarged LASER beam. A CCD camera records the entire speckle pattern, and the fluctuations of scattered intensity are averaged over the pixels of the CCD device. This spatial averaging allows one to have access to the instantaneous dynamics of the evolving system. Experiments are performed in the backscattering geometry. At the beginning of the experiment, whatever the suspension concentration, it is fluid, and the correlation function of diffused light is smoothly decreasing to zero. Then after some time, the evolution of the dynamics of the system becomes erratic: the speckle pattern does not evolve continuously from one configuration to another one, but abruptly changes. In order to quantify this dynamics, the correlation value of any two speckle patterns separated with any time interval τ is computed. The time resolution of our apparatus was 6Hz. We then construct the surface correlation. The value of the correlation between two images taken at t and t+τ:

$$c(t,\tau) = \frac{\langle I_p(t-\tau) I_p(t) \rangle_p}{\langle I_p(t-\tau) \rangle_p \langle I_p(t) \rangle_p} - 1$$

is the height of the surface (fig. 1a and b) $I_p(t)$ is the intensity collected on speckle p at time t, and $<...>_p$ is the average over the pixels. This is a future-past representation. Along the horizontal x-axis, one follows the flow of time, whereas along the vertical y-axis, one goes back into the past, from a given instant, and the usual correlation

function, as computed from MSDWS experiments, is read. For sufficiently long times t, when intermittent dynamics begins, some well defined lines of slope 1 and ∞ appear. Along these lines, the correlation value is anomalously low. The intersection of these lines and the x-axis points out the moment at which a crackling occurs.

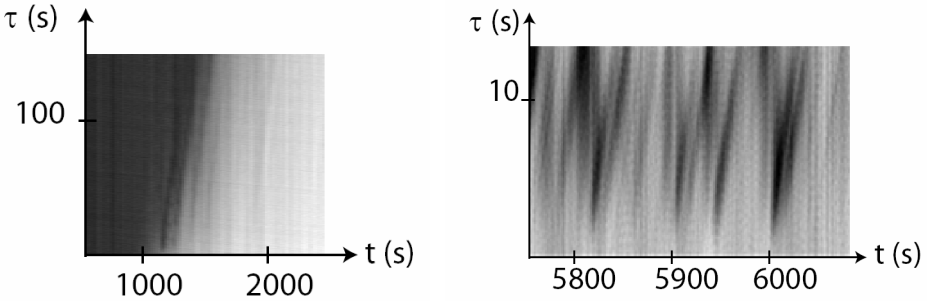

Fig. 1: Future-past correlation surfaces. Correlation increases from 0 to 0.5 from black to white.
a. Left: short time correlation surface, when the transition from a fluid to an elastic behavior occurs.
b. Right: Zoom of the correlation surface at longer times: Correlation losses points, in the (t,τ) plane. Lines are guides to the eye.

We use a concentrated suspension of alumina particles, whose mean diameter is 350 nm. An organic molecule, adsorbed on the particles surface, is used to stabilize the suspension at a high volume fraction, up to 54% [8]. The volume fraction of alumina particles is varied from 32 to 46%. Then, hydroxyaluminium diacetate powder is added to the suspension, at a concentration of 0.45 M. This powder is almost insoluble in water, but slowly decomposes to release acetate and dialuminium ions. The decomposition rate may be controlled by varying the temperature. At 45°C, the characteristic decomposition time, as measured by the salinity of the solution, is 20 minutes, but the diacetate salt continues to decompose for several hours. All the experiments presented here are performed at this temperature. Dynamics of the particles is monitored during five hours after the diacetate salt is added. The elastic modulus of the alumina suspension diverges at a time corresponding to the dissolution time of the diacetate powder, in 20 minutes. When the suspension flocculates, we do not observe any retraction of the system, neither water repulsion.

2. Statistical Analysis of the Intermittent Dynamics

We are now interested in the dynamics of the suspension after it acquires an elastic modulus, for times t longer than 3600s. Let us consider the value of the correlation of two distinct images separated by a constant time interval $c_\tau(t)=c(t,\tau)$ [3] (Fig. 2a). Once the transition to an elastic behavior occurs, these iso-time lag curves have a constant mean value, but are extremely noisy: anomalous correlation losses are observed. Thus, the probability distribution functions are asymmetric and exhibit long tails at low correlation values (Fig. 2b). Above gaussian fluctuations (due to "normal" motion of the scatterers and to noise of our apparatus), giant fluctuations are observed. We thus define a crack as a correlation loss larger than twice the width of the gaussian noise. This anomalous dynamics, identified by comparing two images, at t- τ and t, does not allow to determine which of these two images is responsible for this loss of correlation.

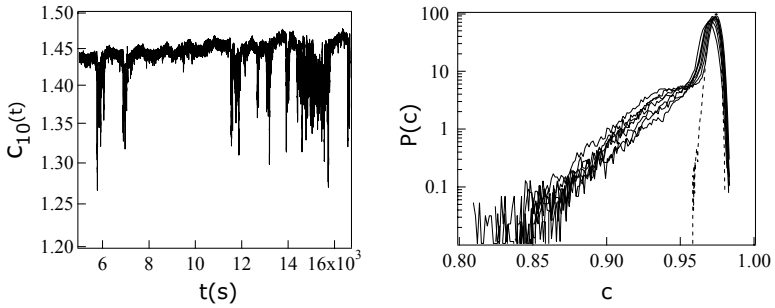

Fig. 2: a. Iso-time lag function, $c_\tau(t)$, for τ= 10 s, as a function of time, t >4000 s, i.e. after the increase of the elastic modulus.
b. probability density function of the iso-time lag curve, for different values of the lag time. When the time lag increases, the curves are shifted towards lower c-values. From right to left :τ = 10 s, τ = 14 s, τ = 18 s, τ = 20 s, τ = 24 s, τ = 27 s, τ = 33 s. Dashed curve is the probability density function obtained for a sample of identical optical properties, at 45° C, but without dynamics. It shows the gaussian noise of our apparatus.

In order to unambiguously identify the time at which crackles occur, we thus find all the anomalous correlation losses for every iso-time lag curve, repeating the previous procedure, and report the corresponding points in the (t, τ) plane. These points define two sub-sets of lines, of slope ∞ and 1 (Fig. 3a). The intersections of ∞ slope lines with the x-axis correspond to images responsible with correlation loss in the past, whereas lines of slope 1 define images where correlation loss occurs with future images. Thus, each time of the x-axis corresponding to an anomalous correlation loss both with future and past, defines a time when a crackle occurs. Crackling regions and arrested dynamics regions are identified this way. Let us now consider the statistical temporal properties of crackling.

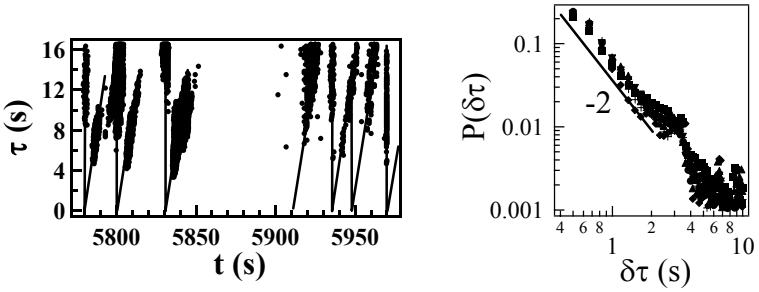

Fig 3. a. Left, in the 2D-MSDWS surface the intersections of the lines of slope 1 and ∞ define when a crackle occurs
b. Probability density function of the waiting time δτ between two cracks
for ϕ=32 % (●),34 % (■), 36 % (▲), 38 % (▼), 42 % (♦), and 44 % (+).

The distribution of waiting times τ between two crackling events is reported on Fig. 3b. At short times, δτ<3s, their distribution function obeys to a power-law function of slope -2. This non-Poissonian statistics implies that it exists short-time correlations between two successive crackles. At longer times, the probability distribution function exhibits a cut-off, but our statistical resolution prevents us from finding an analytical form of the tail of the density of probability of δτ.

Many disordered systems are known to crackle when slowly driven [9], from magnetic materials [10] to sheared bidimensional foams [11]. A common feature of these systems is a lack of characteristic time and size scale. It has been commonly observed that the duration of the events obey to a power law. In such systems, successive events appear to be uncorrelated [12]. Our diffusing light scattering technique allows us to study intermittent dynamics in very turbid systems.

3. References

[1] J.P. Bouchaud, "Aging in glassy systems: new experiments, simple models, and open questions," 'Soft and Fragile Matter: Nonequilibrium Dynamics, Metastability and Flow,', M.E. Cates and M.R. Evans, Eds., IOP Publishing (Bristol and Philadelphia), pp 285-304, (2000).

[2] L Buisson, L Bellon and S Ciliberto," Intermittency in ageing," J. Phys.: Condens. Matter 15, S1163-S1179 (2003).

[3] H. Bissig, S. Romer, L. Cipelletti, V. Trappe and P. Schurtenberger, "Intermittent dynamics and hyper-aging in dense colloidal gels," Physics Chemistry Communications, 6(5):21–23 (2003).

[4] H.M. Wyss, S. Romer, F. Scheffold, P. Schurtenberger and L.J. Gauckler, "Diffusing-Wave Spectroscopy of concentrated alumina suspensions during gelation," Journal of Colloid and Interface Science, 240, 1, 89-97 (2001).

[5] L. Cipelletti and D.A. Weitz, "Ultralow angle dynamic light scattering with a charge coupled device camera based multispeckle, multitau correlator," Review of Scientific Instruments, 70(8), 3214-3221 (1999).

[6] V. Viasnoff, F. Lequeux and D.J. Pine, "Multispeckle diffusing-wave spectroscopy :a tool to study slow relaxation and time-dependent dynamics," Review of Scientific Instruments, 73, 6, 2336-2344 (2002).

[7] P.A. Lemieux and D.J. Durian, "From Avalanches to Fluid Flow: A Continuous Picture of Grain Dynamics Down a Heap," Physical Review Letters, 85(20):4273- 4276 (2000).

[8] R. Laucournet, C. Pagnoux, T. Chartier, J.F. Baumard, "Coagulation method of aqueous concentrated alumina suspensions by thermal decomposition of hydroxyaluminum diacetate," Journal of the American Ceramic Society, 83(11):2661–2667 (2000).

[9] J.P. Sethna, K.A. Dahmen and Ch.R. Myers, "Crackling noise," nature, 410, 242-250 (2001).

[10] J.P. Sethna, K. Dahmen, S. Kartha, J. Krumhansl, B.W. Roberts and J.D. Shore, "Hysteresis and hierarchies : dynamics of disorder-drivenfirst-order phase-transformations," Physical Review Letters, 70, 21, 3347-3350 (1993).

[11] S. Tewari, D. Schiemann, D.J. Durian, C.M. Knobler, S.A. Langer and A.J. Liu , "Statistics of shear-induced rearrangements in a two-dimensional model foam," Physical Review E, 60(4), 4385-4396 (1999).

[12] R. Sanchez, D.E. Newmann and B.A. Carreras, "Waiting-time statistics of selforganized-criticality systems," Physical Review Letters, 88, 6, 068302 (2002).

Diffusing-Wavc Spcctroscopy as a Probc for Ncuronal Activity

J. Li,[1,2] G. Dietsche,[1] D. Iftime,[2] S. E. Skipetrov,[3]
B. Rockstroh,[2] G. Maret,[1] T. Elbert,[2] and T. Gisler[1]

[1] *Universität Konstanz, Fachbereich Physik, 78457 Konstanz, Germany*

[2] *Universität Konstanz, Fachbereich Psychologie, 78457 Konstanz, Germany*

[3] *Laboratoire de Physique et Modélisation des Milieux Condensés/CNRS, Université Joseph Fourier, 38042 Grenoble, France*

In contrast to photon-migration imaging which is playing an increasingly important role as an imaging technique for neurophysiology, experiments using diffusing-wave spectroscopy (DWS) [1, 2] for brain imaging have been scarce: aiming at mapping blood flow velocities in cortical vessels, Lohwasser et al. have tried to account for the effects of multiple light scattering in laser Doppler spectra from brain phantoms [3]. Using a CCD camera, Dunn et al. [4] mapped the cerebral blood flow with spatially resolved measurements of the speckle contrast from an exposed rat cortex. A recent experiment by Cheung et al. [5] on a semi-exposed mouse brain revealed that the field autocorrelation function shows a faster decay with a complex shape upon stimulation by increased CO_2 partial pressure. This suggests that using DWS to investigate functional brain activity in an entirely non-invasive way is likely to be complicated by the heterogenous optical and dynamical properties of the head consisting of scalp, skull, cerebrospinal fluid and white and gray matter. The scattering of light from subcellular organelles in cortical tissue should give rise to speckle fluctuations that are largely unrelated to blood flow. From isolated neural tissue it is known that neurosecretory release enhances the mobility of neurosynaptic vesicles [6–8], which might be detectable by DWS from cortical tissue entirely non-invasively.

In this contribution we present results of near-infrared DWS measurements on a group of volunteers to detect functional activation of the human motor cortex through intact scalp and skull. DWS experiments were performed using a diode laser operating at a wavelength $\lambda_0 = 802\,\mathrm{nm}$, using optical fibers (placed over the motor area C3) to illuminate and to collect multiply scattered light. Activation of the motor cortex was induced by a finger opposition task. DWS signals were recorded both for contralateral and ipsilateral stimulation. Effects of activation were evaluated by comparing the diffusion coefficients extracted from the measured field autocorrelation functions during stimulation and during rest peri-

ods for both contralateral (right-hand) and ipsilateral (left-hand) stimulation by one-tailed t-tests.

Fig. 1 shows the reduced intensity autocorrelation functions $(g^{(2)}(\tau) - 1)/\beta_{\rm coh}$ from a selected subject obtained from the left hemisphere (C3) during baseline and activation, respectively. The autocorrelation function recorded during contralateral stimulation shows a significantly faster decay than during the resting baseline period. Using the dynamic 3-layer model the fitting procedure yields a cortical diffusion coefficient $D_3 = 3.1 \times 10^{-9}{\rm cm}^2/{\rm s}$ during the resting period and $D_3 = 8.8 \times 10^{-9}{\rm cm}^2/{\rm s}$ during the stimulation period. The decay of the autocorrelation function at long times is dominated by the scalp diffusion coefficient D_1 which is found to increase with stimulation (see below). When measuring the autocorrelation function after the end of the motor task, the correlation functions were found to be identical with the baseline correlation functions before stimulation. Our analysis shows that the differences in D_3 and D_1 upon motor stimulation observed in the averaged autocorrelation functions are indeed significant.

When the stimulation is exerted by the left hand, ipsilateral to C3, the autocorrelation function recorded from C3 is found to decay significantly more slowly than for contralateral stimulation. This slower decay is mainly due to fact that the cortical diffusion coefficient for contralateral stimulation $D_3 = 8.8 \times 10^{-9}{\rm cm}^2/{\rm s}$ is larger than the one for ipsilateral stimulation, $D_3 = 6.3 \times 10^{-9}{\rm cm}^2/{\rm s}$.

An analysis of the sensitivity of the fitting procedure on uncertainties in the optical and dynamical parameters shows that within realistic bounds for the optical and dynamical tissue parameters the faster decay of the autocorrelation function during a motor task can be assigned to an increase in cortical diffusion coefficient due to cortical activation. The marked hemispheric asymmetry between the measured cortical diffusion coefficients in the C3 region for left- and for right-hand stimulation is consistent with the dominant activation of the contralateral motor and sensory regions by unimanual motor tasks. While our results suggest that near-infrared DWS can be used to non-invasively investigate subcellular dynamics in the cerebral cortex, it is presently not quite clear whether the observed enhanced dynamics is due to blood flow or to neural dynamics, or due to a combination of both.

---

[1] G. Maret and P. E. Wolf, Z. Phys. B **65**, 409 (1987).

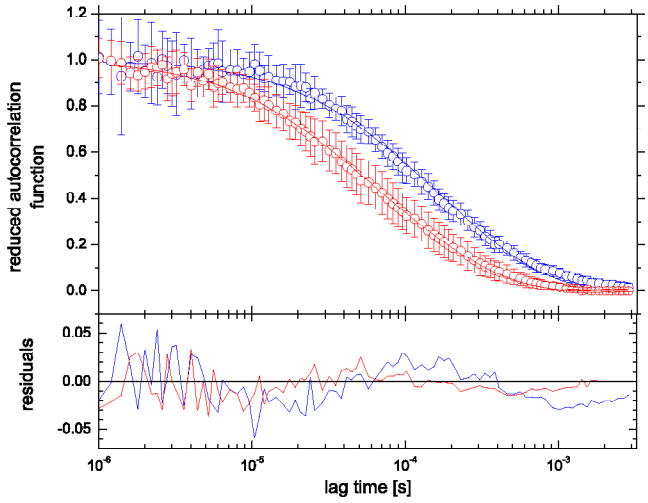

FIG. 1: Reduced intensity autocorrelation function $(g^{(2)}(\tau)-1)/\beta_{\rm coh}$ measured over the C3 area of the motor cortex of a right-handed subject for a source-receiver distance of 20 mm. The blue circles are the resting baseline data; the red circles are the data for contralateral stimulation. The error bars are standard deviations from 2 blocks of 10 runs each. Lines are fits of the analytical solution of the 3-layer correlation-diffusion equation [9] to the data. Best-fit values for diffusion coefficients D_1 and D_3 of scalp and cortex, respectively, are $D_1 = 2.3\times10^{-9}\mathrm{cm}^2/\mathrm{s}$ and $D_3 = 3.1\times10^{-9}\mathrm{cm}^2/\mathrm{s}$ for the resting baseline period and $D_1 = 4.0\times10^{-9}\mathrm{cm}^2/\mathrm{s}$ and $D_3 = 8.8\times10^{-9}\mathrm{cm}^2/\mathrm{s}$ for the stimulation period.

[2] D. J. Pine, D. A. Weitz, P. M. Chaikin, and E. Herbolzheimer, Phys. Rev. Lett. **60**, 1134 (1988).

[3] R. Lohwasser and G. Soelkner, Appl. Opt. **38**, 2128 (1999).

[4] A. K. Dunn, H. Bolay, M. A. Moskowitz, and D. A. Boas, J. Cereb. Blood Flow Metab. **21**, 195 (2001).

[5] C. Cheung, J. P. Culver, K. Takahashi, J. H. Greenberg, and A. G. Yodh, Phys. Med. Biol. **46**, 2053 (2001).

[6] D. B. Sattelle, D. J. Green, and K. H. Langley, Biol. Bull. **149**, 445 (1975).

[7] D. B. Sattelle, J. Exp. Biol. **139**, 233 (1988).

[8] D. Englert and C. Edwards, Proc. Natl. Acad. Sci. USA **74**, 5759 (1977).

[9] S. E. Skipetrov and R. Maynard, Phys. Lett. A **217**, 181 (1996).

Session 8
Photon Scattering

WB 10:40–11:40
Tinbergen Room

Roy Pike, *Chair*

A Fuzzy Simultaneous Measurement of Two Polarization Vector Components

Scott Roger Shepard
Department of Electrical Engineering, Kansas State University, Manhattan, KS shepard@ksu.edu

Abstract We derive a measurement associated with the angular momentum lowering operator, which describes a simultaneous (yet, realizable) measurement of two non-commuting spin vector components. Correlations between two such detectors are also discussed.

I. INTRODUCTION

Photon correlation measurements have a long history of providing experimental tests of a wide variety of fundamental issues in quantum theory, including: violations of local hidden variable (LHV) models [1]; violations of classical second order correlation functions [2]; the existence of optical squeezed-states [3]; etc., - to name just a few. We focus herein, primarily, upon the recent interest in the application of the quantum correlations which violate LHV models to the field of quantum encryption [4] and on a particular simultaneous measurement of non-commuting observables that might *ultimately* threaten the security of such encryption schemes. It is well known that quantum computers [5] threaten the security of traditional encryption schemes (e.g., those based upon the exponential increase of computational time versus the number of symbols in a password, etc.). It is also well known that quantum encryption [4] is intended to restore security by basing it upon the impossibility of simultaneous measurement of non-commuting observables (as opposed to basing it upon computational time). The related measurements have also been crucial in observing violations of LHV models [1],[6] (e.g., Bell's inequalities [6]) and it is interesting to revisit these issues within the modern context of measurements that *can* be associated with non-commuting observables [7](at least in a "fuzzy" sense as described below).

Although many of the Gedanken measurements were originally posed in the context of Stern-Gerlach detectors acting upon spin 1/2 particles [6], the actual experiments were implemented with photons [8](optical polarization being a two state phenomenon). Photonic polarization correlations can be effected via the conservation of angular momenta in a variety of atomic/electronic processes (such as the annihilation of an electron/positron pair in ground state positronium, producing polarization correlated photons at gamma ray frequencies, where analyzers are relatively inefficient, and in the photons emitted via atomic cascade transitions, where polarization beam splitter type detectors first [8] began to yield convincing evidence). Since the language of another fuzzy measurement with which we wish to compare is already expressed in the spin 1/2 context, we will also employ that language in the following (extensions to the corresponding optical implementations already being well established).

II. WHAT IS A FUZZY MEASUREMENT?

Here (for our purposes) this will amount to a set of non-orthogonal kets that resolve the identity operator for some Hilbert space H_s. It is fundamental that such a measurement really corresponds to a complete set of orthogonal kets defined on a larger Hilbert space (incorporating additional systems that must be involved in the measurement). It is only on the larger space that we have the standard quantum description of the measurement in terms of collapsible wavefunctions or sets of commuting observables. Naimark [9] showed that the fuzzy measurement statistics are obtained (from the standard rules on the larger space) when these additional systems are in some particular quantum state.

The classic example of such a measurement is the quantum theory of heterodyne detection [7], [10] which is associated with a measurement of the annihilation operator (and hence the two non-commuting field quadratures − analogous to position and momentum). The source of "fuzziness" in this measurement turns out to be the quantum fluctuations of the image band in its vacuum state.

III. A FUZZY SIMULTANEOUS MEASUREMENT OF $\hat{J}_x$ AND $\hat{J}_y$ FOR SPIN 1/2

Let $H_s <=> \{|+\rangle, |-\rangle\}$ where $\hat{J}_z|\pm\rangle = \pm\hbar/2|\pm\rangle$. We want to associate the measurement with $\hat{J}_- \equiv \hat{J}_x - i\hat{J}_y$, which is a lowering operator on H_s:

$$\hat{J}_-|+\rangle = \hbar|-\rangle, \quad \hat{J}_-|-\rangle = 0. \tag{1}$$

$\hat{J}_-$ has no eigenkets on H_s so we extend it to a larger space: $\hat{E} = \hat{M} + \hat{J}_-$ and look for

$$\hat{E}|E\rangle = e|E\rangle = e(|m\rangle + |e\rangle) \tag{2}$$

where $|e\rangle$ is on H_s and $|m\rangle$ is not on H_s. Focusing on the H_s part (so that we don't yet lock onto any particular extension $\hat{M}$) we have the "$\hat{J}_-$ condition":

$$\psi_+(e) = \frac{e}{\hbar}\psi_-(e) \tag{3}$$

where $|e\rangle \equiv \psi_+(e)|+\rangle + \psi_-(e)|-\rangle$. Since $\hat{J}_- = \hat{J}_x - i\hat{J}_y$ we also impose the condition:

$$e = \zeta(m_x - im_y) \tag{4}$$

where $m_x, m_y \, \epsilon\{-1/2, +1/2\}$. To describe a measurement, we require:

$$\sum_e |e\rangle\langle e| = \zeta_1 \hat{I} \tag{5}$$

where ζ_1 must be real and $\hat{I}$ is the identity operator for H_s. If we also impose normalization,

$$\langle e|e\rangle = 1 \quad (\forall e) \tag{6}$$

we obtain

$$|e\rangle = \frac{1}{\sqrt{2}}(e|+\rangle + |-\rangle) \quad e = \sqrt{2}\hbar(m_x - im_y) \tag{7}$$

and the fuzzy statistics via the probabilities

$$P(e) = \frac{|\langle e|\psi\rangle|^2}{2} \quad (\forall|\psi\rangle \ on \ H_s). \tag{8}$$

We note in passing that there are other ways to derive kets similar to these [11] but those methods arrive at a different set of phases for these kets. The phases obtained in our derivation (based upon association with $\hat{J}_x - i\hat{J}_y$)yield interesting properties in the complementary angle [12] measurements, e.g., equation (10) whereas other phases do not.

Let us begin with an example: spin up along $\bar{x}$, i.e., $|\psi\rangle = \frac{1}{\sqrt{2}}(|+\rangle + |-\rangle)$. The joint distribution for m_x and m_y in this case, $P(e) = \frac{1}{4}(1+\sqrt{2}m_x)$, is uniform in m_y and biased towards up in m_x. Thus, the marginal distribution in m_x, $P(\tilde{m}_x) \equiv \sum_{m_y} P(e)$ is not a delta function. This demonstrates that we cannot have as much precision in one spin component (obtained by going to the marginal distribution) when we first do a fuzzy simultaneous measurement of two spin components. If we only want information about a single spin component then we should measure that component only.

More generally however, we *do* find that the expected values obtained from the marginal distributions are proportional to the expected values obtained in the single component (Stern Gerlach) measurement, i.e., with

$$\langle\tilde{m}_x\rangle \equiv \sum_{\tilde{m}_x} \tilde{m}_x P(\tilde{m}_x) \quad \langle\tilde{m}_x\rangle \equiv \sum_{\tilde{m}_x} \tilde{m}_x P(\tilde{m}_x) \tag{9}$$

we find

$$\hbar\langle\tilde{m}_x\rangle = \langle\hat{J}_x\rangle/\sqrt{2} \quad \hbar\langle\tilde{m}_y\rangle = \langle\hat{J}_y\rangle/\sqrt{2}. \tag{10}$$

Another interesting property of this measurement is that the expected values from the marginal distributions obtained from the complementary two-angle measurement are proportional to the expected values obtained from the single-angle measurement [12], i.e., since complementarity implies a Fourier transform between wavefunctions we can form a two-angle representation via

$$\psi(\phi_x, \phi_y) \equiv \sum_{m_x}\sum_{m_y} \psi(e) e^{-im_x\phi_x} e^{-im_y\phi_y} \tag{11}$$

where $\psi(e) \equiv \langle e|\psi\rangle$. From this we can form marginal distributions

$$P(\tilde{\phi}_x) \equiv \int_{-\pi}^{\pi} |\psi(\phi_x, \phi_y)|^2 d\phi_y \tag{12}$$
$$P(\tilde{\phi}_y) \equiv \int_{-\pi}^{\pi} |\psi(\phi_x, \phi_y)|^2 d\phi_x$$

the expected values of which

$$\langle\tilde{\phi}_x\rangle \equiv \int_{-\pi}^{\pi} \tilde{\phi}_x P(\tilde{\phi}_x) \quad \langle\tilde{\phi}_y\rangle \equiv \int_{-\pi}^{\pi} \tilde{\phi}_y P(\tilde{\phi}_y) \tag{13}$$

have the property

$$\langle\tilde{\phi}_x\rangle = \langle\phi_x\rangle/\sqrt{2} \quad \langle\tilde{\phi}_y\rangle = \langle\phi_y\rangle/\sqrt{2} \tag{14}$$

where $\langle\phi_x\rangle$ and $\langle\phi_y\rangle$ are the expected values of the single-angle representations. In other words, $\langle\phi_x\rangle = \int_{-\pi}^{\pi} \phi_x P(\phi_x) d\phi_x$ with $P(\phi_x) = |\psi(\phi_x)|^2$ where $\psi(\phi_x) = \sum_{m_x} \psi_{m_x} e^{-im_x\phi_x}$ and $\psi_{m_x} = \langle m_x|\psi\rangle$ is the projection of our state onto the x-component spin basis $\hat{J}_x|m_x\rangle = \hbar m_x|m_x\rangle$ (likewise for the single-angle representation about the y-axis).

We throw away information by going to the marginal distributions. Moreover, we've seen how spin up along $\bar{x}$ leads to a "smeared out" marginal distribution in m_x when we first measure both $\bar{x}$ and $\bar{y}$ components in this simultaneous but fuzzy way. Nevertheless, equations (10) and (14) show that the expected values of these marginal distributions follow the expected values of their corresponding single-component (and/or single-angle) measurements.

IV. CORRELATIONS BETWEEN TWO e-DETECTORS FOR THE SPIN ZERO SINGLET

Consider two spin 1/2 particles (a and b) in the spin zero singlet state, i.e., $|\psi\rangle = \frac{1}{\sqrt{2}}(|+\rangle_a|-\rangle_b - |-\rangle_a|+\rangle_b)$. Particle a undergoes a fuzzy simultaneous measurement of its x and y spin components in e-detector a and particle b undergoes a similar measurement in e-detector b. Note that each of these is a four-state detector (in contrast to the Stern Gerlach case) where the four possible outcomes are the four quadrants (or four corners) of the complex e plane ($e = \sqrt{2}\hbar(m_x - im_y)$). The joint distribution for these two (four-state) detectors is $P(e^a, e^b) = \frac{1}{4\hbar}(\frac{1}{2})^3|e^a - e^b|^2$ for the spin zero singlet. Thus, the probability that both detectors give a "click" in the same corner is zero. This is reminiscent of the Stern Gerlach result that if both detectors measure along the same direction then they never are both up or both down. This perfectly (anti) correlated result carries over into the four-state detector case in the sense that P(same corner)=0. In the e-detector case however, we also have: P(opposite corners)=1/2; P(a left of b)=1/4; and P(b left of a)=1/4 (notice that the sixteen possibilities have reduced down to only four due to the rotational invariance of the spin zero singlet state).

In order to compare to the Stern Gerlach case, each detector could risk throwing away information by going to the marginals. For example, if detector a retains only m_x and detector b retains only m_y then we obtain

$$P(m_x^a, m_y^b) \equiv \sum_{m_y^a} \sum_{m_x^b} P(e^a, e^b) = 1/4 \tag{15}$$

i.e., the results are perfectly uncorrelated (like the Stern Gerlach case). If both detectors only retain m_x then we obtain the marginal distribution $P(m_x^a, m_x^b)$ defined similarly to the above. Here the perfect (anti) correlation gets"fuzzed out" in the sense that $P(m_x^a = -m_x^b) = 3/4$ instead of one. Recall however, that we did see a remnant of the perfect (anti) correlation in the *joint* distribution since P(same corner)=0.

If we rotate detector a's axies by ϕ with respect to detector b's axies we obtain the joint distribution $P(e_\phi^a, e^b) =$

$$\frac{1}{16}[1 - 2(m_\zeta^a m_x^b + m_\eta^a m_y^b)\cos(\phi) - 2(m_\zeta^a m_y^b - m_\eta^a m_x^b)\sin(\phi)] \tag{16}$$

where ζ and η are the rotated versions of x and y.

If again, we throw away information by going to the marginals, just to facilitate a comparison with the Stern Gerlach case, then we can derive

$$P(\eta+, y+) = \frac{1}{4}\left[1 - \frac{1}{2}\cos(\phi)\right] \tag{17}$$
$$P(\eta+, x+) = \frac{1}{4}\left[1 - \frac{1}{2}\sin(\phi)\right]$$

where $P(\eta+, y+)$ denotes the probability that particle a is up along η when ζ is ignored and particle b is up along y when x is ignored, etc. These differ from their Stern Gerlach counterparts only in the factors of 1/2 in front of the trigonometric functions. Since $P(x+, y+) = 1/4$, we find that these marginal probabilities do not violate the Bell's inequality [5], [6]

$$P(\eta+, y+) \leq P(\eta+, x+) + P(x+, y+) \tag{18}$$

for any value of the rotation angle ϕ.

It must be noted however, that the above Bell's inequality stems from a local hidden variable model that is based on the perfect (anti) correlation that occurs in the Stern Gerlach case, i.e., it is based on P(opposite)=1. In the e-detector case, we had P(same)=0 in the joint statistics, which is different. Thus, the local hidden variable model that equation (18) is based on is not really appropriate for the e-detector case. One might derive a local hidden variable model for the e-detectors. It would be especially interesting to do this for their joint statistics (rather than throwing away information that we've already measured by going to the marginals). Even so, the most interesting correlations should occur if we go beyond the fuzzy measurement statistics by working in a larger Hilbert space.

References

[1] R. A. Bertlmann and A. Zeiinger *Quantum [Un]speakables* (Springer, 2001); and references therein.
[2]R. Loudon *The Quantum Theory of Light* (Academic Press, 1983); and references therein; see also: P. Grangier, G. Roger, and A. Aspect, Europhys. Lett. **1**, 173-177 (1986).
[3]NASA CP-3135 *Workshop on Squeezed State and Uncertainty Relations*, D. Han, Y. S. Kim and W. W. Zachary ed(s)., College Park, MD (1991).
[4]SPIE-5128 *First International Symposium on Quantum Informatics*, Y. Ozhigov ed., Lipki, Russia (2002).
[5] NASA-QCQS'98 *Quantum Computing and Quantum Communications*, Colin P. Williams ed., Palm Springs, CA (1998).
[6] J. Bell, Physics **1**, 195-211 (1964).
[7]C. W. Helstrom *Quantum Detection and Estimation Theory* (Academic Press, 1976).
[8] A. Aspect, P. Grangier and G. Roger, Phys. Rev. Lett. **49**, 91-96 (1982).
[9] M. A. Naimark, Izv. Akad. Nauk SSSR, Ser.Mat. **4** 277-281 (1940).
[10]H. P. Yuen and J. H. Shapiro, IEEE Trans. Inform. Theory **IT-26** 78-86 (1980).
[11]P. Busch, "Some Realizable Joint Measurements of Complementary Observables, Found. Phys. **17** 905-937 (1987).
[12] S. R. Shepard,"A Quantum Theory of Angle," in *Fundamental Problems in Quantum Theory* (Annals of the New York Academy of Sciences, 1995), pp. 812-821.

Fractal Structure of Biotissues Polarization Properties

O.V. Angelsky, Ye.G. Ushenko, Yu.A. Ushenko and A.G. Ushenko
Correlation Optics Dept, Chernivtsi University, 2 Kotsyubinsky Str., Chernivtsi, 58012 Ukraine
Ushenko@itf.cv.ukrtel.net

Abstract. The interconnection between geometry of biotissue structure with their polarization properties has been studied. It has been shown that fractal character of polarization properties of physiologically normal biotissue transforms into a multifractal for a pathologically changed one.

1. Introduction

Measuring the Stokes vector of light scattered by biotissue (BT) and calculating the corresponding Mueller matrix enable to obtain the comprehensive (statistically averaged over bioobject's inhomogeneities) information on its polarization properties [1]. The analysis of such information is promising for the studying the macrostructure of various BTs for diagnostics of their physiological state. The techniques for non-invasive optical coherent tomography (OCT) and its novel branch, namely, polarization-sensitive OCT (PSOCT) based on measuring 2D depth-resolved Mueller matrix elements (Mueller-matrix images - MMI) with high space resolution (~ 1 μm) and high scanning speed [2-4] represent a very important direction of such diagnostics.

This paper presents the study of the interconnection between self-similar geometry of BT structure with the peculiarities of manifestation of their polarization properties, which are comprehensively described by the totality of Mueller matrix 2D elements.

The investigation is based on the following principles:

1. The geometry of BT architectonics possesses hierarchical self-similar thread-like structure with microfibrillae, fibrillae, fasciae, fibers, bundles as the "structural elements". Such elements are discrete and characterized by scale repeatability in the wide range of optical measures (from 1 μm to 10^3 μm). The planar and spatial twist-effects of transformation of orientations and scales of fibrillar components, being the analog of affine transformations, forming mathematical fractals, are the mechanisms of architectonic nets' growth.
2. As the optical objects, the structural elements of BT architectonics hierarchy possess the properties of optically uniaxial crystals, the direction of optical axes of which is determined by angular directions ρ(X,Y) of fibrillae packing relative to the plane of the analyzed layer of BT, while the value of birefringence (Δn) is determined by the properties of fibrillae substance. The scale self-similarity of their transverse geometrical measures ($d(X,Y)$) enables to assume the same self-similar changing the magnitude of phase-shift ($\delta(X,Y)=\left(2\pi/\lambda\right)\Delta n d(X,Y)$) between the orthogonal components of polarization at passing of optical radiation with wavelength λ through BT.
3. BT can be presented morphologically by two-component amorphous-crystalline structure [5]. That's why, the Mueller matrix of BT layer analyzed by PSOCT is determined by superposition of partial operators of its amorphous, $\{a_{ik}\}$, and crystalline $\{c_{ik}\}$ components

$$\{B\}=\begin{Vmatrix} 1 & 0 & 0 & 0 \\ 0 & c_{22}+a_{22} & c_{23} & c_{24} \\ 0 & c_{32} & c_{33}+a_{33} & c_{34} \\ 0 & c_{42} & c_{43} & c_{44}+a_{44} \end{Vmatrix}, \tag{1}$$

$$\begin{aligned} &a_{22}\approx a_{33}\approx a_{44}=e^{-\tau L}; \\ &c_{22}=\cos^2 2\rho+\sin^2 2\rho\cdot\cos\delta; c_{23}=c_{32}=\cos 2\rho\sin 2\rho(1-\cos\delta);\cdot \\ &c_{24}=-c_{42}=-\sin 2\rho\sin\delta; c_{33}=\sin^2 2\rho+\cos^2 2\rho\cos\delta; \\ &c_{34}=-c_{43}=\cos 2\rho\sin\delta; c_{44}=\cos\delta. \end{aligned} \tag{2}$$

Here τ is the extinction of radiation at the BT layer with thickness *L*.

It follows from Eqs. (1) and (2) that geometrical (orientation) $\rho(X,Y)$ and optical (phase) $\delta(X,Y)$ parameters of the BT's architectonic nets structural elements play the determining role in transforming the

polarization state of the probing beam. The impact of these two factors into formation of the totality of MMI $b_{ik}(X,Y)$ can be regarded as the result of multiplication of several spatially dependent fractal functions of various dimensions $F_{mn}[\rho(X,Y);\delta(X,Y)]$. Thus, one expects that coordinate dependencies $b_{ik}(X,Y)$ describing polarization properties of BT are either fractal or multifractal as well.

2. Objects Under Study

The optically thin ($\tau \le 0.1$) histological sections of normal and pathologically changed (due to psoriasis) human skin derma (SD) are investigated. The samples possess the following geometrical/optical parameters: the absorption coefficient μ_a = 2.2 cm^{-1}, the scattering coefficient μ_s = 185 cm^{-1}, the anisotropy parameter g = 0.82, the geometric thickness L = 30 μm.

3. Analysis and Discussion of Experimental Data

The results of study the coordinate distributions of the SD MMIs are presented in Figs. 1 to 2.

Figs. 1 and 2 show $b_{ik}(X,Y)$ (left columns) and the corresponding $P_j\{\log K_{X,Y}[b_{ik}(X,Y)], \log[d^{-1}(X,Y)]\}$, calculated for physiologically normal (Fig. 1) and pathologically changed (Fig. 2) samples of SD.

It can be seen from the data obtained that:

- MMI $b_{22,33}(X,Y)$ (Fig. 1a, 1c) of physiologically normal SDs are characterized by practically monofractal structure ($\{D^{(j)}[b_{ik}(X,Y)]\} \approx$ const) within the almost of three decades of the measures (2μm - 10^3μm) of architectonics structural elements;
- fractal dimensions of MMI $b_{22,33}(X,Y)$ (Fig. 1b, 1d)of SD do not coincide to each other ($D_{22} = 2{,}63; D_{33} = 2{,}46$);
- the structure of MMI element $b_{44}(X,Y)$ (Fig. 1e) of SD is multifractal : the fractal dimensions are characteristic of the two ranges (Fig. 1f) of collagen fibers sizes d ($D_{44}^{(2)}(2\mu m \div 8\mu m) = 2{,}11$ and $D_{44}^{(1)}(8\mu m \div 200\mu m) = 2{,}61$);
- the processes of pathological changes in SD structure are accompanied by the changes in their geometrical-optical properties, namely, fractal structure of MMI of the elements $b_{22,33}(X,Y)$ is transformed into multifractal one (Fig. 2a, 2c), while new additional fractal dimensions appear (Fig. 2b, $D_{22}^{(2)}(2\mu m \div 10\mu m) = 2{,}38$; $D_{22}^{(1)}(10\mu m \div 800\mu m) = 2{,}71$ and Fig. 2d, $D_{33}^{(2)}(2\mu m \div 10\mu m) = 2{,}09$; $D_{33}^{(1)}(10\mu m \div 800\mu m) = 2{,}58$);
- the fractal structure of MMI of element $b_{44}(X,Y)$ remains within the limits of small sizes of structural elements (Fig. 2e, 2f, - $D_{44}^{(2)}(2\mu m \div 20\mu m) = 2{,}18$).

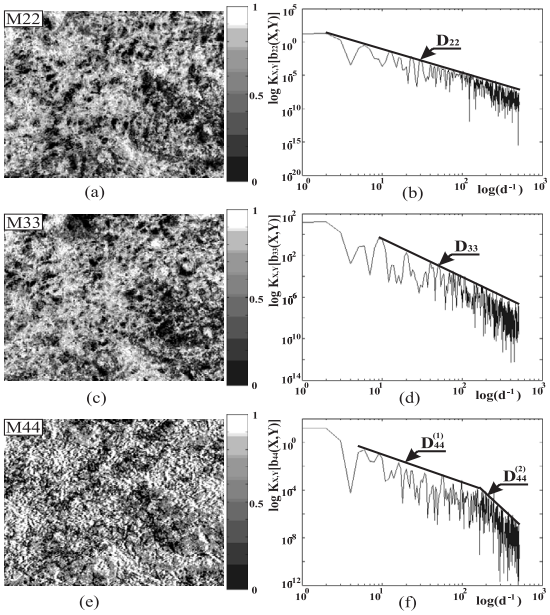

Fig. 1. Coordinate (a, c, e) and fractal (b, d, f) structure of MMI physiologically normal SD elements.
D – the areas of fractal structure of MMI, S - the areas of statistic structure of MMI.

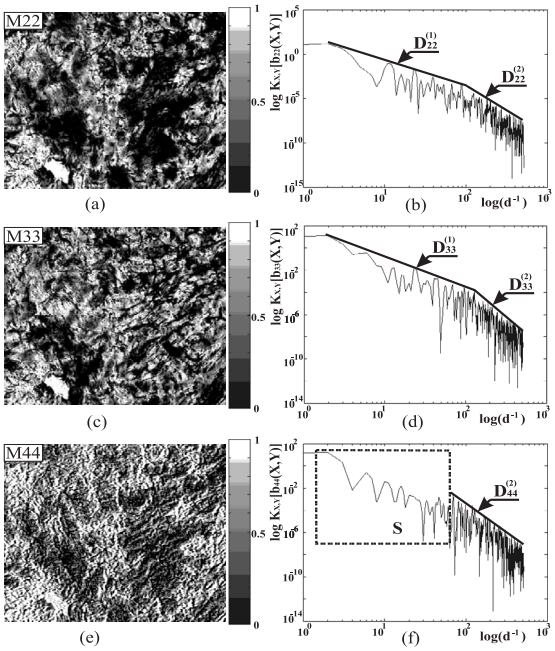

Fig. 2. Coordinate (a, c, e) and fractal (b, d, f) structure of MMI pathologically changed SD elements. The marcs are the same as in Figure 1.

Conclusions

It has been demonstrated that fractal geometric structure of architectonic nets of physiologically normal biotissues manifests itself in the fractal character of their polarization properties, described by the totality of 2D elements of Mueller matrices.

The processes of pathological changes of BT architectonics manifest themselves in the appearance of new fractal dimensions and forming multifractal structure of MMI of orientation Mueller matrix elements and destruction of large-scale fractal structure of phase elements MMI.

References

[1]. H. C. van de Hulst, Light Scattering by Small Particles Dover, New York, (1957).

[2]. G. Yao and L.-H. Wang, ‘‘Two-dimensional depth-resolved Mueller matrix characterization of biological tissue by optical coherence tomography, ’’ Opt. Lett. **24**, 537-539 (1999).

[3]. S.-L. Jiao, G. Yao, and L.-H. Wang, ‘‘Depth-resolved two-dimensional Stokes vectors of backscattered light and Mueller matrices of biologi-cal tissue measured with optical coherence tomography,” Appl. Optics, **39**, 6318-6324(2000).

[4]. S. Jiao and L.-H. Wang, ‘‘Two-dimensional depth-resolved Mueller matrix of biological tissue measured with double-beam polarization-sensitive optical coherence tomography,’’ Opt. Lett. **27** (2), 101–103 (2002).

[5]. A.G. Ushenko, “Stokes correlometry of biotissues,” Laser Physics, **10** (6), 1 – 7 (2000).

2-D Stokes-Correlometry of Biotissues Images in Pre-Clinic Diagnostics of Their Pre-Cancer States

O.V. Angelsky, Ye.G. Ushenko, Yu.A. Ushenko and A.G. Ushenko
Correlation Optics Dept, Chernivtsi University, 2 Kotsyubinsky Str., Chernivtsi, 58012 Ukraine
Ushenko@itf.cv.ukrtel.net

Abstract: This research is directed to combine the possibilities of polarization-sensitive OCT (PSOCT) of biotissue (BT) with correlation method of analysis of 2-D parameters of Stokes vector of object fields for early diagnostics of pre-tumour changes of connective tissue (CT).

1. Characteristics of the Objects of Investigation

Optically thin histological sections of physiologically normal and pathologically changed (dysplasia – pre-cancer state of CT diagnostics of which by means of traditional histo-chemical methods is extremely difficult) CT of cervix of the uterus with the following optical-geometric parameters: the absorption coefficient μ_a = 2.2 cm^{-1}, the scattering coefficient μ_s = 185 cm^{-1}, the anisotropy parameter g = 0.82, the geometric thickness L = 30 μm. Architectonic nets of such BT are formed by the totality of protein collagen bundles with the birefringence index $\Delta n(DS) \approx 1.5 \times 10^{-3}$.

Pathological changes of CT are morphologically accompanied with the formation of "growth directions" and the increase of the sizes of collagen fibers.

2. Analysis and Discussion of Experimental Data

The results of the investigation of the totality of 2DS$_i$ [1-3] of all types of CT images are presented in Fig. 1, 2.

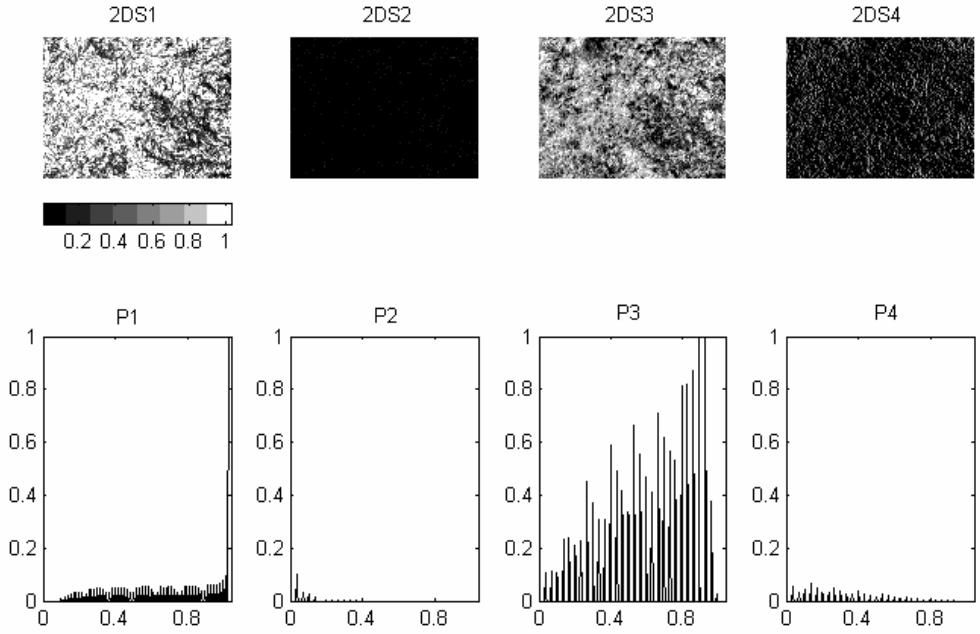

Fig. 1. 2-D structure of Stokes vector physiologically normal CT

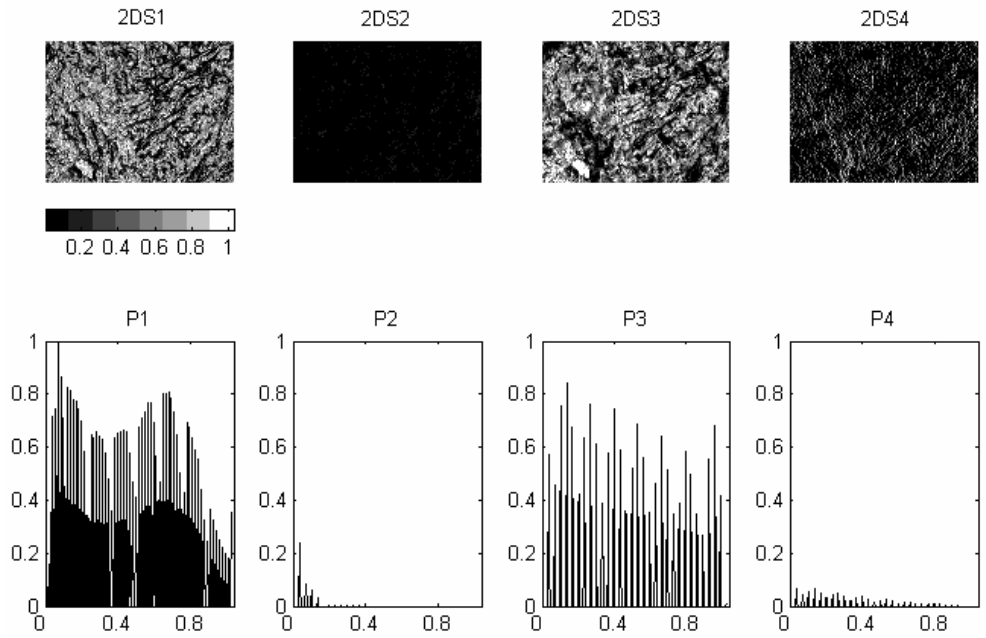

Fig. 2. 2-D structure of Stokes vector pathologically changed CT

Here, the $2DS_i$ (the upper row) and the corresponding probability distributions of Stokes vector parameters values $P_i\{S_i(X, Y)\}$ (lower row) are presented, which were found for physiologically normal (Fig. 1) and pathologically changed (Fig. 2) CT images.

From data obtained one can observe that:

- polarization structure of CT images is inhomogeneous – the totality of all $2DS_i$ has the wide range of change of relative values from 0.0 to 1.0.
- coordinate distributions of relative values of several $2DS_i$ have individual character.
- probability distributions $P_i\{S_i(X, Y)\}$ represent a "quasi-discrete" structure, consisting of continuous series of local extrema of $2DS_i$.
- comparative analysis of statistic structure of $2DS_i$ of normal and pathologically changed samples of CT proved that for BT images with pre-cancer dysplasia the relative value and the range of changes of ensemble of $2DS_2$ and $2DS_4$ parameters increase. The reverse trend is observed for coordinate distributions of the 3rd parameter of Stokes vector $2DS_3$. Quantitatively such differences of polarization characteristics of CT images of both types are illustrated in the comparative Table 1, in which the statistic moments of the 1st (M_s), second (D_s) and higher orders (A_S, E_S) of $2DS_{i=2,3,4}$ are compared.

Table 1. Point statistic characteristics of $2DS_i$ CT images Stokes vector elements

$2DS_{i=2,3,4}$	Normal (37 samples)		Pre-cancer -Dysplasia (36 samples)		
$2DS_{i=2}$	M_S	0.01	M_{SP}	0.08	$M_S<M_{SP}$
	D_S	0.0003	D_{SP}	0.02	$D_S<D_{SP}$
	A_S	4,56	A_{SP}	9,73	$A_S<A_{SP}$
	E_S	136,3	E_{SP}	174,5	$E_S<E_{SP}$
$2DS_{i=3}$	M_S	0.57	M_S	0.19	$M_S>M_{SP}$
	D_S	0.06	D_{SP}	0.01	$D_S>D_{SP}$
	A_S	60,7	A_{SP}	133,4	$A_S<A_{SP}$
	E_S	198,6	E_{SP}	256,7	$E_S<E_{SP}$
$2DS_{i=4}$	M_S	0,13	M_{SP}	0,23	$M_S<M_{SP}$
	D_S	0,04	D_{SP}	0,09	$D_S<D_{SP}$
	A_S	4,2	A_{SP}	4,9	$A_S<A_{SP}$
	E_S	282	E_{SP}	430,1	$E_S<E_{SP}$

Let's analyze the data, obtained from the point of view of suggested in this paper optical model of CT architectonics.

The formation of new "growth directions" and scaling of CT collagen fibers sizes at the appearance of pre-tumor state is optically shown increasing of "Phase-shifting" ability ($\delta(X, Y)$) of architectonic net substance. That's why the relative values of Stokes vector parameters ($S_i \Rightarrow \begin{cases} \sin\delta \\ 1-\cos\delta \end{cases}$) increase for the images of such samples and decrease for such ($S_i \Rightarrow \cos\delta$). That's why either increase of average ($M_{S2,4}$) and dispersion ($D_{S2,4}$) ensemble of relative values or decrease of ($M_{S3,}$ D_{S3}) for their coordinate distributions are observed.

The interconnection between the CT physiological state and the asymmetry (A_s) and excess (E_s) of 2-D distributions of Stokes vector parameters of corresponding images appears to be more distinct. In this case the orientation structure of architectonic nets determines the values of the corresponding statistic moments. The appearance of new growth directions is accompanied by the extension of the set of values of ($M_{S3,}$ D_{S3}) in the plane of CT sample.

Conclusions

1. The totality of diagnostically urgent properties, determining the interconnection between statistic and correlation characteristics of $2DS_i$ parameters of BT images and their physiological state.
2. Processes of pathological changes of BT architectonics show in:
   - the change of values of the 1st ($M_{S2,4.}$) and 2nd ($D_{S2,4}$) statistic moments of $2DS_i$ ($M_{S3,}$ - increase; D_{S3} - decrease);
   - the increase by one order of the 3rd and 4th statistic moments of Stokes vector parameters.

References

[1]. G. Yao and L.-H. Wang, ''Two-dimensional depth-resolved Mueller matrix characterization of biological tissue by optical coherence tomography," Opt. Lett. **24**, 537-539 (1999).

[2]. S.-L. Jiao, G. Yao, and L.-H. Wang, ''Depth-resolved two-dimensional Stokes vectors of backscattered light and Mueller matrices of biological tissue measured with optical coherence tomography,'' Appl. Optics, **39**, 6318-6324(2000).

[3]. S. Jiao and L.-H. Wang, ''Two-dimensional depth-resolved Mueller matrix of biological tissue measured with double-beam polarization-sensitive optical coherence tomography,'' Opt. Lett. **27** (2), 101–103 (2002).

Session 9
Correlation in Optical Fields

WC 13:30–14:30
Tinbergen Room

Robert Brown, *Chair*

Higher-Order Correlations in Speckle Fields

A. Dogariu and J. Ellis
School of Optics, CREOL,
University of Central Florida, Orlando, Florida

Abstract: We show that the joint probability distribution of polarization information and the complex degree of mutual polarization can be used to differentiate between different highly scattering media which depolarize the light in a global sense.

It is now well established that polarization can provide additional information pertinent to material discrimination in active sensing[1]. However, in highly scattering, highly depolarizing geometries, this information is often lost due to the globally unpolarized nature of the light.

In order to fully describe this situation one has to carefully address the information about the polarization properties of radiation. Traditionally, the polarization properties of light in a particular point in space are fully described by the polarization tensor (also known as the coherency matrix). This formalism is sufficient to describe situations where there is no variation of the field characteristics from point to point. Starting from the concepts of coherence and polarization, we have recently generalized the conventional degree of polarization introducing a two-point parameter, the complex degree of mutual polarization, which is defined in terms of measurable quantities. The magnitude of complex degree of mutual polarization is a measure of the similarity between the states of polarization in two different points in space and can therefore be used to describe higher-order statistical properties of vector fields[2].

In most previous treatments, Gaussian statistics are often invoked due to the high number of scattering centers contributing to the measured intensities. For realistic media, this imposes a rather strong restriction which makes the material characterization or discrimination a complicated task[3]. Our experiments, however, suggest that higher-order vector correlations could potentially offer in-depth information about the underlying optical fields[4] and relate to material characteristics.

In practice, a number of measurable distributions, including intensity, phase difference, ellipticity, and states of polarization can be derived from the statistics of random complex fields. Every point in a globally depolarized field, whether this is a point in space, time, or a member of an ensemble, can be considered as resulting from the summation of a large number of underlying fields. The probability distribution of these underlying fields will determine the state of polarization at that particular point and it is the object of our study. Under certain conditions, it is possible that the underlying fields are locally unpolarized, in which case no information about them can be retrieved beyond the intensity statistics. It is also possible that the underlying fields are locally polarized, in which case the resulting distribution of polarization states can be studied on the surface of the Poincare sphere. In the case when a globally depolarized field is composed of locally polarized states, one can differentiate between various types of globally unpolarized light, and, therefore, infer additional information about the underlying random fields.

---

[1] A. P. Bates, K. I. Hopcraft, and E. Jakeman, "Non-Gaussian fluctuations of Stokes parameters in scattering by small particles," Waves in Random Media **8** 235-253 (1998).
[2] J. Ellis and A. Dogariu, *Complex degree of mutual polarization,* Opt. Lett. 29, 920 (2004).
[3] S. M. Cohen, D. Eliyahu, I. Freund, and M. Kaveh, "*Vector statistics of multiply scattered waves in random systems*," Phys. Rev. A **43**, 5748-5751 (1991).
[4] J. Ellis and A. Dogariu, "*Differentiation of globally depolarized complex random fields*", J. Opt Soc. Am. A21, (2004), in press.

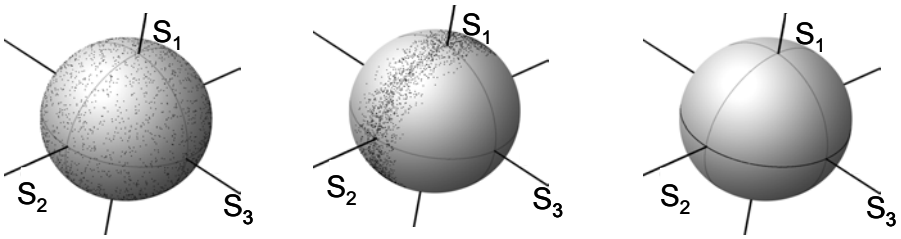

Figure 1. Distribution of states of polarization resulting from coupling between the distributions of underlying fields. The joint distributions are displayed on the Observational Polarization Sphere and are physically accessible through intensity measurements for spatially resolved speckle fields.

Depending on the invariances of their statistical properties, we have demonstrated three types of unpolarized light, classified as type I, II and type III unpolarized light. While the various cases are not all invariant to the introduction of arbitrary retardances, the unpolarized nature of the light is preserved under any rotation of the Poincare sphere due to the polar symmetry of the distributions. The first situation exactly replicates the case of underlying Gaussian fields in all measurable quantities and is of type I, while the examples of type II and III unpolarized light can be distinguished via the measurements of the Stokes Vector element correlations. Specifically, the six cross-correlations of the Stokes vector elements serve to distinguish between the three cases of globally unpolarized fields.

Experimentally, we examined a specific imaging geometry in which the assumption of Gaussian statistics is no longer valid and we have analyzed the fourth-order moments of the joint probability distribution of polarization information in the resulting speckle field. We have also developed a dipole scattering model, and have shown that this can be used to distinguish material parameters such as the local polarizability tensor and the preferential orientation of the scattering centers.

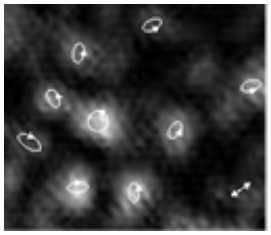

Figure 2. Experimentally recorded intensity distribution and the corresponding polarization ellipses. This field is globally unpolarized.

We will present experimental data where the second-order statistics of the electric field (intensity and average state of polarization) can not discriminate between the underlying scattering media (highly diffusive media such as porous materials, paints or compressed powders). In these cases, forth-order statistics available through the joint probability distributions, and spatial correlations such as intensity correlation and the CDMP provide the additional information necessary to discern between various types of materials.

In conclusion, we demonstrate that different types of globally unpolarized light can be distinguished on the basis of Stokes vector element correlations. We would like to emphasize that the primary reason for using these Stokes vector element correlations is that they can be obtained through simple intensity measurements. Our results strongly suggest that these polarization measurements will have applicability in characterizing the properties of dense scattering media where intensity information yields little or no information.

Coupling of Correlated Entangled Photons Into Single-Mode Optical Fibers

R. Andrews
Department of Physics, Faculty of Agriculture and Natural Sciences, The University of the West Indies, St. Augustine, Republic of Trinidad and Tobago, W.I.
randrews@fans.uwi.tt

E. R. Pike and Sarben Sarkar
Department of Physics, King's College London, Strand, London WC2R 2LS, UK.
roy.pike@kcl.ac.uk, sarben.sarkar@kcl.ac.uk

Abstract: We present a multimode theory that describes the coupling of single photons generated by collinear Type-I parametric down-conversion into single-mode optical fibers. An expression for the fiber diameter which maximizes the coupling is obtained.

1. Introduction

The optical process of spontaneous parametric down-conversion (SPDC) involves the virtual absorption and spontaneous splitting of an incident (pump) photon in a transparent nonlinear crystal producing two correlated lower-frequency (signal and idler) photons [1]. The pairs of photons can be entangled in a multi-parameter space of frequency, momentum and polarization. In type-I SPDC the photons are frequency-entangled and the signal and idler photons have parallel polarizations orthogonal to the pump polarization. Entangled photons have been used to demonstrate quantum nonlocality [2], quantum teleportation [3] and, more recently, quantum information processing [4] and quantum cryptography [5]. One of the challenges in recent practical schemes such as quantum cryptography and quantum communication is to maximize the efficiency of coupling of single photons into single-mode optical fibers. Several models and experiments have been developed to predict and measure the coupling efficiencies of down-converted light into single-mode fibers [6,7]. In this contribution we present a detailed theoretical model describing single-photon mode coupling in the simple situation of collinear type-I down-conversion. The pair photon count rate is calculated and an analytic expression which determines the condition for optimum single-photon coupling in single-mode optical fibers is obtained in terms of experimental parameters.

2. Amplitude for Pair Detection in Single-Mode Fibers

The amplitude for detecting photon pairs at conjugate space-time points $(\vec{r}_1,t_1)$ and $(\vec{r}_2,t_2)$ is defined by

$$A^{(2)} = \left\langle \vec{E}_H^{+}(\vec{r}_1,t_1)\vec{E}_H^{+}(\vec{r}_2,t_2)\right\rangle \tag{1}$$

where t_1 and t_2 are detection times of signal and idler photons and $\vec{E}_H(\vec{r}_i,t)$ are the Heisenberg electric field operators [8]. In the steady state the right-hand-side of (1) can be expressed as

$$\int d^3r_3\int d^3k_1\int d^3k_2 U^{*}_{\vec{k}_1\lambda_1}(\vec{r}_3)U^{*}_{\vec{k}_2\lambda_2}(\vec{r}_3)U_{\vec{k}_0\lambda_0}(\vec{r}_3)f_p(\vec{r}_3)\left(\frac{\hbar\omega_{k_0}}{2\varepsilon_0}\right)^{\frac{1}{2}}\left(\frac{\hbar\omega_{k_1}}{2\varepsilon_0}\right)^{\frac{1}{2}}\left(\frac{\hbar\omega_{k_2}}{2\varepsilon_0}\right)^{\frac{1}{2}}$$
$$\times\left\langle \alpha_{k_0},0\left|\vec{E}_I^{(+)}(\vec{r}_2,t_2)\vec{E}_I^{(+)}(\vec{r}_1,t_1)\right|\alpha_{k_0},k_1,k_2\right\rangle\delta(\omega_{k_1}-\omega_{k_2}-\omega_{k_0}) \tag{2}$$

$\vec{E}_I(\vec{r}_i,t)$ are the interaction-picture electric field operators at some arbitrary but specified detection points $\vec{r}_1$ and $\vec{r}_2$ and $f_p(\vec{r}_3)$ is a function which describes the shape of the pump in the transverse direction; $U_{\vec{k}_i\lambda_i}(\vec{r}_3)$ are plane-wave modes describing the electromagnetic field in free space with $\vec{k}_1,\vec{k}_2$ as the wave vectors of the signal and idler photons, $\vec{k}_0$ is the wave vector of the incident pump photon and λ_i are polarization indices. (As in our

previous studies we have not introduced the effects of a change in the linear refractive index between the crystal and its surroundings. The incorporation of this difference does not qualitatively change our conclusions.) The initial state of the electromagnetic field $\left|0,\alpha_{k_0}\right\rangle$, consists of a coherent state with wave-vector k_0 (the monochromatic pump beam) with other modes in the vacuum state $\left|0\right\rangle$. We take the quantized electric field in the fiber as

$$\vec{E}^{+}(\vec{r},t)=i\sum_{\lambda\lambda'}\int d^3k'\int d^3k\left(\frac{\hbar\omega_k}{2\varepsilon_0}\right)^{1/2}\vec{\varepsilon}_{\vec{k}\lambda}\beta_{\vec{k}'\lambda',\vec{k}\lambda}U^{f}_{\vec{k}\lambda}(\vec{r})e^{-i\omega t}a_{\vec{k}\lambda} \tag{3}$$

where the coupling coefficient $\beta_{\vec{k}'\lambda',\vec{k}\lambda}$ is a projection onto the appropriate fiber mode and is defined as

$$\beta_{\vec{k}'\lambda',\vec{k}\lambda}=\int dxdyU^{in}_{\vec{k}'\lambda'}(x,y)U^{f*}_{\vec{k}\lambda}(x,y) \tag{4}$$

$U^{in}_{\vec{k}'\lambda'}(\vec{r})$ are spatial modes incident on the fiber and $U^{f}_{\vec{k}\lambda}(\vec{r})$ are the fiber modes. For single-mode fibers we assume a spatial mode profile that is independent of $\vec{k}$ and λ. We may therefore suppress the fiber mode indices in (4) to simplify the notation. After performing the integration over the volume of the crystal and evaluating the expectation value Eqn. (2) simplifies to

$$\int d^3k_1\int d^3k_2\tilde{f}_p\left(\vec{k}_{1t}+\vec{k}_{2t}\right)\mathrm{sinc}\left(\Delta_{\mathrm{k}_{1z}\mathrm{k}_{2z}}\frac{d}{2}\right)\beta_{k_1\lambda_1}\beta_{k_2\lambda_2}U^{f}(\vec{r}_1)U^{f}(\vec{r}_2)$$

$$\times\left(\frac{\hbar\omega_{k_1}}{2\varepsilon_0}\right)^{1/2}\left(\frac{\hbar\omega_{k_2}}{2\varepsilon_0}\right)^{1/2}e^{-i\omega_{k_1}t_1}e^{-i\omega_{k_2}t_2}\delta\left(\omega_{k_0}-\omega_{k_1}-\omega_{k_2}\right) \tag{5}$$

where *d* is the length of the crystal, $\Delta_{k_{1z}k_{2z}}=k_0-k_{1z}-k_{2z}$ and the signal/idler wave vectors are defined as $\vec{k}_i=\hat{x}k_{ix}+\hat{y}k_{iy}+\hat{z}k_{iz}$ where *i* = 1,2 denote signal,idler modes and k_{ix},k_{iy},k_{iz} are components of the wave vector along the x,y,z directions respectively. $\tilde{f}_p(\vec{k})$ is the two-dimensional Fourier transform of $f_p(\vec{r})$ which is assumed Gaussian. For degenerate signal and idler photons emitted at a cone angle θ^* to the pump and for frequencies close to the degenerate frequency, the sinc function in (5) can be approximated to unity in a first-order analysis.

3. Two-Photon Count Rate in Single-Mode Fibers

Consider the situation in which the fiber is in the focal plane of the lens, i.e., $d'=f$. We assume that Gaussian frequency filters are used to select nearly-degenerate photons. Then for $k^2\omega_0^4<<f^2$ and to first-order in the dispersion of the crystal, the two-photon amplitude in (5) approximates to

$$A^{(2)}\propto\int_{-\infty}^{\infty}e^{-i\tau x-\frac{x^2}{\Delta^2}}\left(1-e^{(a+bx)}\right)^2dx \tag{6}$$

where

$$a=\left(-\frac{k^{*2}\omega_0^2}{2f^2}-i\frac{k^{*3}\omega_0^4}{2f^3}\right)R^2,\quad b=\left(-\frac{k^*\omega_0^2v}{f^2}-i\frac{3}{2}\frac{vk^{*2}\omega_0^4}{2f^3}\right)R^2 \tag{7}$$

τ is the time difference between the detection of signal and idler photons, k^* is the degenerate phase-matched wave number, *v* is the first order dispersion coefficient of the crystal and Δ is the bandwidth of the down-converted light reaching the fibers. In this calculation we have taken a hard circular aperture of radius *R* at the imaging lens but

the calculation can also be made for a gaussian input profile. To obtain the count rate we take the modulus square of the integral in (8) and integrate over all τ . To a good approximation we obtain

$$\left|A^{(2)}\right|^2 \propto \left(1-4e^{-y}+6e^{-2y}-4e^{-3y}+e^{-4y}\right) \tag{8}$$

where $y = k^{*2}\omega_0^2 R^2 / 2f^2$. This approaches a maximum when $y \geq 4.4$. This gives the fiber radius $\omega_0 \geq 1.5 f\lambda / \pi R$ for optimal coupling. For a fiber diameter equal to the Rayleigh width of the diffraction pattern of the aperture, i.e., $\omega_0 = f\lambda / \pi R$, the two-photon count rate in the fiber is only 56% of the maximum.

4. Conclusion

We have presented, from a first-principles calculation, a fully quantized multimode theory to describe the coupling of correlated single photons generated by collinear Type-I SPDC into single-mode optical fibers. We have thus produced a practical recipe to maximize the coupling of these single photons into optical fibers. As pointed out earlier this is important for quantum cryptography and quantum communication applications. For the type-I collinear down-conversion studied here, we find no significant dependence of the coupling on the transverse width of the pump beam and crystal length which have been obtained for non-collinear geometries. The important parameters for the collinear case are simply the photon wavelength, the focal length of the lens and the fiber diameter.

5. References

[1] D.C. Burnham and D.L. Weinberg, "Observation of simultaneity in parametric production of optical photon pairs," Phys. Rev. Lett. **25**, 84-87 (1970).

[2] P.G. Kwiat, K. Mattle, H. Weinfurter, A. Zeilinger, A.V. Sergienko, and Y. H. Shih, Phys. Rev. Lett. **75**, 4337-4341 (1995).

[3] L. Vaidman, "Teleportation of quantum states," Phys. Rev. A **49**, 1473-1476 (1994).

[4] J-W Pan, D. Bouwmeester, H. Weinfurter and A. Zeilinger, "Experimental entanglement swapping: Entangling photons that never interacted," Phys. Rev. Lett. **80**, 3891-3894 (1998).

[5] A. K. Ekert, J. G. Rarity, P. R. Tapster, and G. M. Palma, "Practical quantum cryptography based on two-photon interferometry," Phys. Rev. Lett. **69** (9), pp. 1293-1295 (1992).

[6] C. Kurtsiefer, M. Oberparleiter, and H. Weinfurter, "High-efficiency entangled photon pair collection in type-II parametric fluorescence," Phys. Rev. A **64**, pp 023802 (2001).

[7] F.A. Bovino, P. Varisco, A.M. Colla, G. Castagnoli, G.D. Giuseppe, and A.V. Sergienko, "Effective fiber coupling of entangled photons for quantum communication," Optics Communications **227**, pp 343-348 (2003).

[8] R. Andrews, E.R. Pike and Sarben Sarkar, "Photon correlations and interference in type-I optical parametric down-conversion," J. Opt. B: Quantum semiclass. Opt. **1**, 588-597 (1999).

Spatial Properties of a Superposed Speckle Field and Its Application to the Fabrication of Random Laser Media

Takashi Okamoto, Hiroyuki Gotou, Tatsuya Yonemori, and Yasuaki Kawabata

Department of Systems Innovation and Informatics, Kyushu Institute of Technology
680-4, Kawazu, Iizuka, Fukuoka 820-8502, Japan
Phone: +81 948 29 7725, Fax: +81 948 29 7725, E-mail: okamoto@ces.kyutech.ac.jp

Abstract: The statistical properties of a three-dimensional laser speckle field produced by three scattered waves superposed with one another are studied theoretically. It is shown that the spatial anisotropy of intensity distributions still remains even when the three speckle fields are interfered with one another. Superposed fractal speckles and their binarized intensity are also investigated in terms of spatial self-similarity. A new method for fabricating random laser media with the use of photopolymers is proposed, and a preliminary experiment is performed.

1. Introduction

When a random gain medium is excited with energy larger than a critical value, laserlike emission with narrow spectral peaks is observed in the pumped region of the medium. This type of light emission systems is now called random lasers [1], and a number of experiments have been conducted using various kinds of disordered materials. For example, particle suspensions that contain dye solutions, polymers with scatterers and dyes, and semiconductor powders are typical disordered media for observing isotropic random laser emissions. Although most of the studies concerning random lasers employ small particles as scatterers, it is important to study other scattering systems that will exhibit different lasing properties from those of conventional random lasers.

From this point of view, we have paid attention to photopolymers. Recently, photopolymers that can be cured by ultraviolet or visible light are used for fabricating three-dimensional (3D) prototypes and nanometer-scale photonic crystals. In this study, we propose an alternative method to make a disordered medium by illuminating transparent photopolymers with laser speckle patterns. If the high intensity regions in the speckles are cured and the other regions remain in a liquid phase, the resultant object after removing the liquid polymer has a 3D random structure. Since the speckle size in the direction parallel to the optical axis is much larger than that in the transverse directions, we employ three speckle beams propagating in the direction perpendicular to one another. In this paper, we first derive the analytical expressions for the statistical properties of crossed speckle fields, and then verify the theoretical results by means of computer simulations. In the simulations, binarized fractal speckles are also analyzed to examine the possibility of realizing fractal random media. Finally, results for a preliminary experiment of fabricating photopolymer random media are presented.

2. Theory

Figure 1 depicts the optical geometry used for analyzing the superposed speckle field. Three transparent diffusers (diffuser1, 2, and 3) are placed at the ξη, η' ζ', and ζ"ξ" planes, and the ξ', η", and ζ axes are crossed at one point and form, respectively, the x, y, and z axes in the observation space. Diffuser1, 2, and 3 are illuminated normally by linearly polarized light beams with polarization direction cosines of ($2^{-1/2}$, $2^{-1/2}$, 0), (0, $2^{-1/2}$, $2^{-1/2}$), and ($2^{-1/2}$, 0, $2^{-1/2}$), respectively. We show here the final expressions for the probability density function of the intensity and the normalized autocorrelation function of the intensity fluctuations, which are given, respectively, by

$$p_I(I) = -\left(\frac{12I}{\langle I\rangle^2} + \frac{8}{3\langle I\rangle}\right)\exp\left(-\frac{6I}{\langle I\rangle}\right) + \frac{8}{3\langle I\rangle}\exp\left(-\frac{3I}{2\langle I\rangle}\right),$$

$$\gamma_{\Delta I}(\Delta\mathbf{x}) = \frac{1}{6}\left(\left|\gamma_{A_x}\right|^2 + \left|\gamma_{A_y}\right|^2 + \left|\gamma_{A_z}\right|^2 + \left|\gamma_{A_1}\right|^2 + \left|\gamma_{A_2}\right|^2 + \left|\gamma_{A_3}\right|^2\right),$$

where $\langle I \rangle$ is the average intensity, $\Delta\mathbf{x}$ is the distance between two points in the observation space, γ_{Ax}, γ_{Ay}, γ_{Az} are the normalized autocorrelation function of the complex amplitudes for the x, y, and z polarization components, respectively, and γ_{A1}, γ_{A2}, and γ_{A3} are the normalized autocorrelation function of the complex amplitudes coming from diffuser1, 2, and 3, respectively.

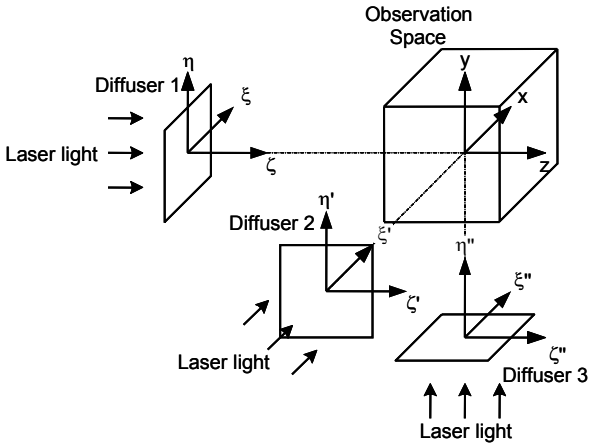

Fig. 1. Schematic diagram for producing a superposed speckle field.

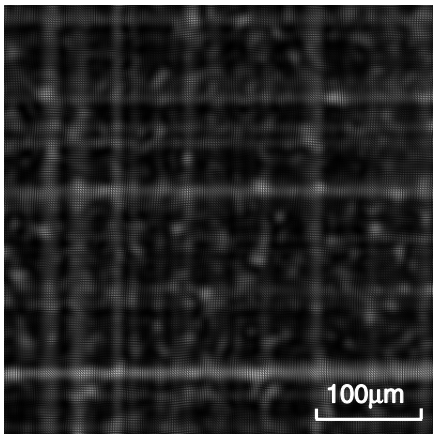

Fig. 2. Intensity distribution across the *xy* plane. All diffusers are 100 mm away from the origin of the observation space.

3. Simulation

We generate numerically the superposed speckle field by means of a Huygens-Fresnel elementary wave calculation [2] to verify the theoretical results. An example of the *xy* plane cross section of the intensity distribution is shown in Fig. 2, where a Gaussian beam with a wavelength of 632.8 nm and a diameter of 5 mm is used for illumination. The corresponding autocorrelation functions evaluated from the theory and the simulation are plotted in Fig. 3. We can see from Fig. 2 that each speckle grain has a periodic structure arising from the interference between scattered waves propagating in orthogonal directions. This structure gives periodic fluctuations in the autocorrelation function in Fig. 3. It should be noted that there still remains a long-range correlation component that represents speckle grains elongated along the optical axis. The long-range correlation can be seen in Fig. 2 as a cross-stitch pattern. Although the simulation curve shown in Fig. 3 is obtained by one particular realization of the speckle field, the correlation function is almost reproduced by the theory.

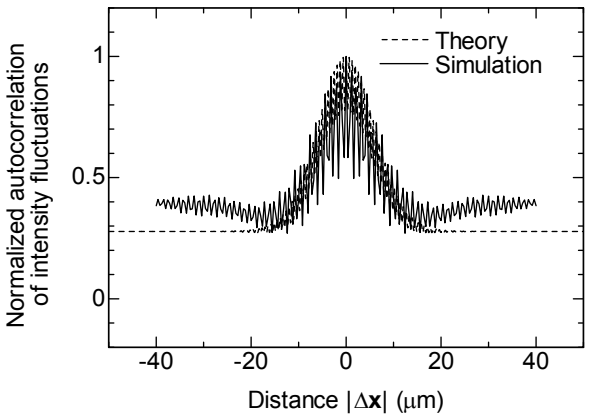

Fig. 3. Autocorrelation function of intensity fluctuations plotted along the x direction. The theoretical curves taken along the x, y and z directions are the same.

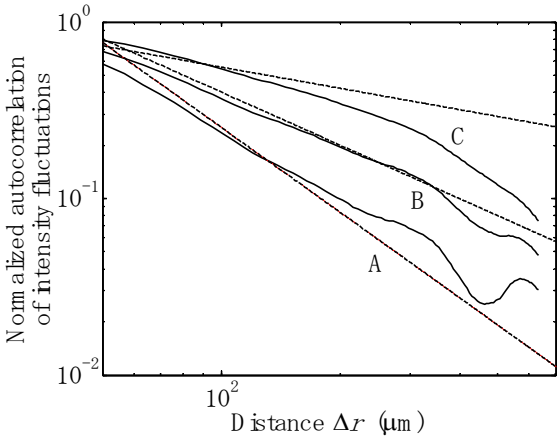

Fig. 4. Autocorrelation function of intensity fluctuations for a fractal speckle field. The dimensions of random fractal objects are 1.2 (A), 1.5 (B), and 1.8 (C).

It has been shown that regular and irregular fractal structures enhance optical gain and emissions [3,4]. According to a method proposed by Uozumi et al. [5], we generated numerically three fractal speckle waves propagating in orthogonal directions by employing an illuminating beam with a power law intensity distribution. The resultant fields were then superposed incoherently. Figure 4 shows the autocorrelation function of fractal speckles averaged over all directions of solid angles. Three curves in Fig. 4 are the results obtained using three different dimensions of random fractal objects that are necessary to produce the power law illumination in actual experiments. The theoretical lines are derived under the assumption that fractal speckles are distributed homogeneously in 3D space. Although there are discrepancies between theory and simulation, we confirm that fractality exists in the superposed speckle field because of the power-law behavior of the intensity correlation. In order to examine whether the fractality still remains after binarization of the speckle intensity, the autocorrelation functions were calculated with different threshold intensities. The result reveals that the fractal properties exist in binarized speckle distributions, and that the fractal dimension is changed with the threshold intensity.

4. Experiment

We carried out an experiment to capture and store 3D speckle structures in photopolymers. An adhesive (OPTOKLEB OPM55, Adell corp.) that can be cured by visible light was used because of the ease of treatment. The photopolymer in a cuvette was exposed for 3 minutes to a speckle field arising from a single diffuser that was illuminated by an argon-ion laser beam (λ=488 nm). The cuvette was then bathed in methanol to wash out the liquid monomers. Microscope images of fabricated random media are shown in Fig. 5. A simple diffraction experiment implies that a randomly distributed cylinder-like structure is formed inside the photopolymer. Further experiments on multiple light scattering, such as coherent backscattering measurements, will be needed to assure that the polymer media fabricated with the proposed method can serve as a host medium for random lasers.

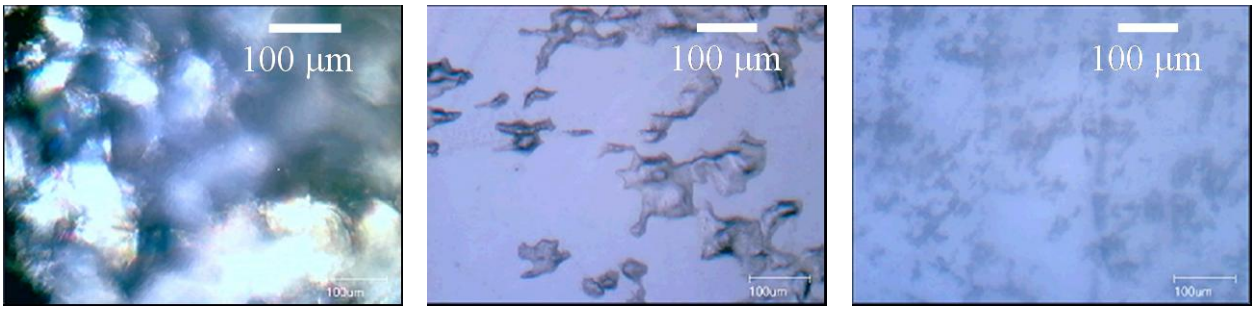

(a) (b) (c)

Fig. 5. Photographs of the surface of photopolymer cured by a single speckle beam of visible light. The average speckle diameters are (a) 350 μm, (b) 150 μm, and (c) 20 μm.

5. Conclusion

We have studied the statistical properties of the 3D light scattering field that is produced by interference of different speckle fields. The superposed field has a random intensity distribution in a macroscopic scale, but it has a periodic spatial structure in a microscopic scale. We have also confirmed that a superposition of fractal speckle fields results in a random fractal distribution of the intensity in 3D space, even if the intensity is binarized with a certain threshold value. A preliminary experiment has shown that one can capture and reserve the high intensity regions of a speckle field by means of a photopolymerization technique.

6. References

[1] H. Cao, "Random lasers with coherent feedback," in *Optical properties of nanostructured random media,* V. M. Shalaev, ed. (Springer, Berlin, 2002), pp. 303-328.

[2] E. Kolenovic, W. Osten, and W. Juptner, "Non-linear speckle phase changes in the image plane caused by out of plane displacement," Opt. Commun. **171,** 333-344 (1999).

[3] T. Okamoto, "Light amplification by multilayers with fractal gain structures," Proc. SPIE **3749**, 122-123 (1999).

[4] W. Kim, V. P. Safonov, V. M. Shalaev, and R. L. Armstrong, "Fractals in microcavities: giant coupled, multiplicative enhancement of optical responses," Phys. Rev. Lett. **82**, 4811–4814 (1999).

[5] J. Uozumi, M. Ibrahim, and T. Asakura, "Fractal speckles," Opt. Commun. **156,** 350-358 (1998).

Session 10
Correlation in Optical Fields

WD 14:50–15:30
Tinbergen Room

William Meyer, *Chair*

On the Prospects of Diagnostic of Wave Dislocation Obtained in Light

O.V. Angelsky, A.P. Maksimyak, and P.P. Maksimyak
Correlation Optics Dept, Chernivtsi University, 2 Kotsyubinsky Str., Chernivtsi, 58012 Ukraine
Oleg@optical.chernovtsy.ua

Abstract: The possibility of application of edge and screw dislocations of the field, obtained in polychromatic light for diagnostics of different phase-inhomogeneous structures, including nano-structures has been considered.

The paper deals with the investigation of singularity in the field of optical coherent and partially coherent radiation, diffracting on the phase-inhomogeneous structures of micrometer and sub-micrometer ranges.

The possibilities of diagnostic application of such formations of the field have been analyzed.

On this purpose the peculiarities of forming the edge and screw dislocations of the field, diffracted on the elementary structures like phase step, cylindrical straight and spherical lenses have been studied. The investigation has been carried out both in monochromatic and in polychromatic light, formed by the combination of three colors: red, green, blue, RGB={1,1,1}.

It was found that in the case of polychromatic radiation, the main diagnostic feature of the field amplitude zero is the formation of the so-called flower with colored petals joint in the center, i.e. application of the so-called chromascope [1]. The necessary condition providing the formation of the amplitude zero is achieving the central point by all the colored petals, i.e. joining of all the petals in one central point (the core). Depending on the object structure, causing the formation of the amplitude zeroes of the field, the form of the flower can change from radial-symmetric (ideally) to asymmetric one.

The flower under consideration is the diagnostic analogue of the famous interference forklet for the case of monochromatic radiation [2].

In the case of forming the edge dislocation of wave-front the picture of color distribution is sufficiently different both in its form and in the sequence and regularity of the colored bands order.

The regularities of forming the amplitude zeroes of the field, diffracting at the phase steps of different height at the width of the step less than the wavelength of the visible light. It is shown that the amplitude zeroes for different spectral components of the visible light occur at various heights of phase steps. This effect can be used as a diagnostic one for the height estimation of phase relief of diffraction structures of sub-micrometer cross-section, obtained in the processes of growth or spraying.

It was found that the structure of the field of monochromatic radiation formed after passing of the cylindrical lens is quite corresponding to assumptions, given in the article [3], i.e. there are caustics in the field, in the vicinity of which the amplitude zeroes of the field are formed. The peculiarities of the distribution of these zeroes are determined by both the aperture conditions of the experiment and the wavelength of the radiation used.

In particular, it was found that the singularities are not formed while illuminating with the beam with the Gaussian intensity distribution inside the conical pyramid of the focused beams behind the cylindrical lens. It is also shown that depending on the aperture size of the illuminating beam the zone of the formation of singularities is changed. Thus, at the diameter of the beam less than 50 μm, it is the zone nearby the surface of the cylinder, and, at the diameter more than 50 μm it is in the vicinity of the focus. The dependence of probability of singularities appearance on the radius of the cylinder surface is observed in the zone of conical pyramid of the focused beams behind the lens.

While studying the picture of the field distribution in polychromatic radiation the effect of self-similarity in the distribution of amplitude zeroes in axial and transversal directions have been observed (Fig. 1). This is particularly well shown while using the polychromatic radiation. The quite distinctly repeated field distribution is recorded, that is shown both in the strict order of colors between the places of zero loci and in the color gamma in the vicinity of amplitude zeroes.

It is possible to consider the investigated distributions the fractal ones. Besides, it is pointed out that the level of fractal distribution of the amplitude zeroes depends on the radius of the cylindrical lens surface. The level of fractality increases with the increase of the size of the object. The longitudinal scale of fractality of distribution is proportional (f/a), and the cross one – $(f/a)^2$, where a – the lens size, f - its focus distance, i.e. the scaling is characterized by self-affinness. Fig. 2 presents the dependence of the fractal level in the field on the size of the lens.

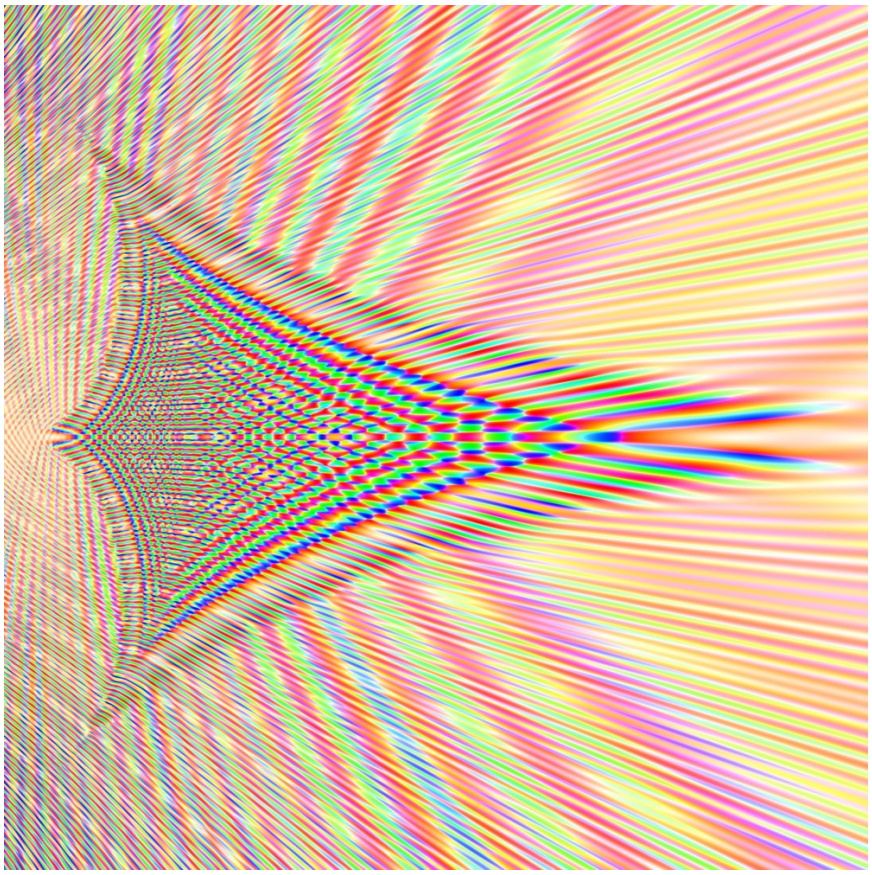

Fig. 1. Diffraction pattern for cylindrical lens with diameter 100 μm after chromascope.

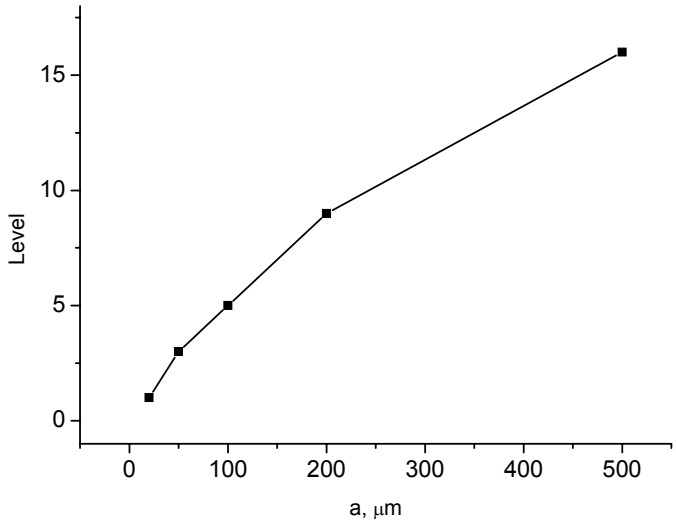

Fig. 2. Dependence of the fractal level in the field on the size of the lens.

References

[1]. M.V. Berry, "Exploring the colours of dark light," New Journal of Physics **4**, 74.1–74.14(2002).

[2]. N.B. Baranova, A.V. Mamayev, N.F. Pilipetsky, V.V. Shkunov, and B.Ya. Zeldovich, "Wavefront dislocations: topological limitations for adaptive systems with phase conjugation," JOSA A **73**, 525-528 (1983).

[3]. J.F. Nye, "Evolution from a Fraunghofer to a Pearcey diffraction pattern," J. Opt. A: Pure Appl. Opt. **5** 495-502 (2003).

The Role of Caustics in Formation of Network of Amplitude Zeroes for Partially Developed Speckle Field

O.V. Angelsky,[1] P.P. Maksimyak,[1] A.P. Maksimyak,[1] S.G. Hanson,[2] and Yu.A. Ushenko[1]
[1] Correlation Optics Dept, Chernivtsi University, 2 Kotsyubinsky Str., Chernivtsi, 58012 Ukraine
[2] Optics and Fluid Dynamics dept., RISØ National Laboratory, P.O. Box 49, DK-4000 Roskilde, Denmark.
Oleg@optical.chernovtsy.ua

Abstract: The topology of a partially developed speckle field is studied using interference techniques. It has been shown that formation of interference forklets in the field gives evidence of changes in the field topology, being the diagnostic sign of transition from a planar Fraunhofer diffraction pattern to a three-dimensional pattern of a diffraction catastrophe.

1. Introduction

Among the problems that are solved successfully within the concept of singular optical, one must emphasize:

- the techniques for generation of isolated singularities (also called wave front dislocations, vortices, or amplitude zeroes) in the field [1, 2];
- the topology of the network of amplitude zeroes for the speckle field at the model (qualitative) level [3-5];
- the optical techniques for diagnostics of singularities for the field [6, 7];
- the use of singularities for the field in solving application problems, such as manipulating small particles (i.e. optical traps and tweezers) [8, 9].

The interest in the study of local amplitude and phase structures of the field in the vicinity of singularities, not only for monochromatic radiation field but also for polychromatic fields, has considerably increased recently [3, 10-12]. Papers [13, 14] devoted to the study of the scenario and mechanisms of nucleation and evolution of singularities in the vicinity of caustics have appeared.

Despite for reasons of fundamental nature, such investigations are stimulated by problems in applied diagnostic. As a matter of fact, the successful solving of diagnostic problems by determination of statistical or fractal parameters of the objects *via* analysis of large areas of the scattered radiation field (networks of vortices) is hampered without knowing the mechanisms of nucleation of amplitude zeroes. Actually, the extensive diagnostic usage of the networks of stable structure, such as amplitude zeroes, is a matter of interest for the nearest future. Besides, initial successful attempts to use a totality of these structural formations for the field in diagnostic problems have just been reported [15]. At last, knowledge of the structural amplitude and phase parameters of the field at micro- and nanoscale (subwavelength) levels is of undoubted importance for solving the problems of nanotechnology [16, 17].

Nucleation of amplitude zeroes for the coherent radiation field takes place only if a phase variance of inhomogeneities of the rough surface (with which the beam interacts) exceeds unity. In this case, partial signals with phase differences exceeding π take part in formation of the scattered field, and, as a consequence, amplitude zeroes are nucleated [18]. A rough surface with such height parameters can be considered as the generating source for singularities. The areas of sharp focusing of partial signals (caustics) also take part in the development of singularities for the speckle field. That is why the interest in local amplitude and phase structures of the field is evident [19].

The purpose of this paper is to study and demonstrate the mechanisms of nucleation and evolution of singularities for a coherent radiation field scattered by a surface with large inhomogeneities, at the zone, in which partial signals are focused, i.e. in the vicinity of caustics.

2. Interference study of the scattered field structure

To determine the loci of amplitude zeroes for the field, we use the interference technique [6], which is now of the widest use for detection of optical wave front singularities. Amplitude zeroes are revealed by typical interference forklets (or bifurcations of interference fringes). Besides, we determine the loci of amplitude zeroes by solving the system of equations:

$$\begin{cases} \mathrm{Re}\left[A(x,y)\right]=0, \\ \mathrm{Im}\left[A(x,y)\right]=0. \end{cases} \qquad (1)$$

using the software approved in [15].

The amplitude and phase of the field resulting from diffraction of a plane wave at the phase relief of a rough surface can be calculated by the double Rayleigh-Sommerfeld diffraction integral [20]:

$$U(\xi,\zeta) = \frac{z}{i\lambda}\int\int \frac{A(x,y)}{R^2(x,y,z,\xi,\zeta)} \times \exp\{-ik[R(x,y,z,\xi,\zeta)(n-1)h(x,y)]\}dxdy \quad . \tag{2}$$

where $A(x,y)$ is the aperture function that corresponds to the amplitude transmittance of a rough surface (see Fig. 2), $R(x, y; \xi, \zeta, z) = [z^2 + (x - \xi)^2 + (y - \zeta)^2]^{1/2}$ is the distance between the surface point and the observation point, z is the distance between the plane of the object to the observation plane, and x, y; ξ, ζ are the rectangular Cartesian coordinates at the object plane and the observation plane, respectively. Eq. (2) is applicable to the field calculations at an arbitrary distance z.

The field is computed at various distances from the object. Subsequently, a coherent reference wave is imposed on the computed field to analyze the field based on the interference pattern. The period of this is chosen to be several times less than the speckle size. Thus, one can determine the loci of field singularities and estimate the phase distributions of the field in the vicinity of the amplitude zeroes.

Whereas the area of caustics (zones of sharp focusing) is determined by the relation between the phase variance and the correlations length of inhomogeneities of a rough surface, partial signals corresponding to various scales of the surface inhomogeneities can be focused at different distances. The distribution of the corresponding zones of focusing along the $Z-$ coordinate is governed by the distribution of the ratio of the inhomogeneities phase variance to the associated correlation lengths. As a result, one expects relatively smooth distribution of such zones along the $Z-$ coordinate for a random rough surface, in contrast to the case of fractal rough surface, where such distribution exhibits pronounced maxima [15].

As the observation plane is removed further from the caustics zone, a "planar" diffraction pattern is transformed into a three-dimensional one, i.e. into diffraction catastrophe, according to the classification introduced in [14]. Strictly speaking, the mechanism of formation of singularities involving cross-interference of partial beams is initiated at this stage. This stage is of special interest in the study of the mechanisms for evolution of singularities by the analysis of local phase distributions into vicinity of caustics of different forms.

Further, we have applied the interference technique for diagnostics of phase saddles in the field. To reveal such specific areas of the field phase structure, we use the quasi-coaxial superposition of the coherent reference beam. In this case, a complex phase distribution of the tested area of the field is transformed into a corresponding intensity distribution that is different for two orthogonal directions: from maximum through minimum to maximum, and from minimum through maximum to minimum. To provide reliable control, we also investigated an interference pattern arising from off-axis interference of two beams. The absence of interference forklets in the previously found areas of the loci of the phase saddles confirms the reliability of the suggested technique.

Within the framework of interference investigation, the effect of so-called clustering of amplitude zeroes becomes clear. This effect manifests itself in the appearance of areas of the field, where the spatial density of amplitude zeroes considerably exceeds the average density [15]. The main prerequisite for this effect is that caustics take part in the formation of the field or, in other words, a "planar" diffraction pattern is transformed into a three-dimensional pattern of diffraction catastrophe. In the present case of interest, the caustics zones play the role of the centers of nucleation and evolution of singularities as the observation plane moves away from the object. The structure of clusters matches the form of the caustics.

3. Structure of the field in the vicinity of caustics

Note that the approach introduced here allows us not only to look for a scenario of evolution of considerable fragments of a field, picking up some interesting peculiarities of this process, but also to investigate the mechanisms of evolution of separate groups of singularities in the vicinity of caustics of various form, similar to the approach revealed in [13, 14]. Visual analysis of the computed fragments of a field based on the study of both intensity distribution and interference patterns at caustics zones permits us to pick up small areas of a field, whose structure corresponds (in terms of the catastrophe theory) to the fold, cusp, swallowtail, and so on. Using this possibility, we now investigate the main observable elementary events causing transformation of the field topology, i.e. we look for the field evolution from the caustic zone to a far field. Our simulation, being as close as possible to a real experimental situation, provides discrete analysis of the field at various distances Z from the object. In this case, analysis of the field evolution along the Z-coordinate is performed via comparison of the successive set of

interference patterns registered at discrete planes. So, we compare the patterns illustrating the coordinate distributions of the point of crossing of three-dimensional lines of zero amplitude with the corresponding planes.

The topology of the field changes, which is evident from the nucleating screw dislocations, detected interferometrically as forklets. Generally, the considered mechanism corresponds to the one described theoretically in [13], where the passing to a three-dimensional diffraction pattern is accompanied by the appearance of the corresponding "switches" of arch-like form. Thus, the main principle that governs the evolution of the lines of amplitude zeroes is confirmed. Each change in the topology of dislocation on $z = 0$ nucleates a new arch on the $z > 0$ side.

Thus, in the evolution of the dislocations from their birth to annihilation one can observe that, as the observation plane is removed from the point of birth of amplitude zeroes creating the so-called dipole, the following happens:

- amplitude zeroes can deflect, being at the common plane, which is perpendicular to the observation plane;
- the pair of amplitude zeroes constituting a dipole, pushing apart, performs rotation or through-and-back motion on a break trajectory, if the motion is projected to the plane of observation;
- both the amplitude zeroes of opposite signs constituting one dipole and the amplitude zeroes of opposite signs of different dipoles can annihilate;
- the appearance of interference forklets in the field behind the caustics zone is the diagnostic sign of passing from a "planar" Fraunhofer diffraction pattern to a three-dimensional one, i.e. of the change of the field topology.

4. Conclusion

In summary, we have proposed to use the interference approach for investigating the scenario of development of singularities in the coherent field scattered by a rough surface with large inhomogeneities, as a function of the distance to the observation plane. This approach, based on computer simulations, provides results, which are close to the results of laboratory experiments. We have demonstrated the feasibility for study of the mechanisms and peculiarities of the development of complex speckle fields and their amplitude and phase structure at various scale levels and at various registration zones. We have applied interference techniques to diagnose phase saddles for the optical field. Known mechanisms and scenario for formation of partially developed speckle fields with inherent singularities have been confirmed and demonstrated. The mechanisms of transformation of a developed speckle field structure resulting in changes of topology have been investigated.

We confirmed that caustics are inalienable components in the scenario for formation of networks of amplitude zeroes for coherent field scattered by a rough surface with large inhomogeneities. It has been shown that caustics are the centers of formation of clusters of amplitude zeroes for a partially developed speckle field.

References

[1]. N.R. Heckenberg, R. McDuff, C.P. Smith, and A.G. White, "Generation of optical phase singularities by computer-generated holograms," Opt. Lett. – 1992. – V.**17**. – P. 221-223.

[2]. O. Angelsky, R. Besaha, and I. Mokhun, "Appearance of wave front dislocations under interference among beams with simple wave fronts," Optica Aplicata. – 1997. – Vol. **XXVII**. – №4. - P. 273-278.

[3]. J.F. Nye and M. Berry, "Dislocations in wave trains," Proc. R. Soc. Lond. – 1974. – A. **336**. – P. 165-190.

[4]. I. Freund, N. Shvartsman and V. Freilikher, "Optical dislocation networks in highly random media," Opt. Comm. – 1993. – V. **101**. – P. 247-264.

[5]. I. Freund and N. Shvartsman, "Wave-field phase singularities: The sign principle," Physical Review. – 1994. – V. **50**. – № 6. – P. 5164-5172.

[6]. N.B. Baranova, B.Ya. Zeldovich, A.V. Mamayev, N.F. Pilipetsky, and V.V. Shkunov, "Dislocation of the wavefront of a speckle-inhomogeneous field (theory and experiment)," JETP. – 1981. – V. **33**. – P. 1789-1797.

[7]. N.B. Baranova, A.V. Mamayev, N.F. Pilipetsky, V.V. Shkunov, and B.Ya. Zeldovich, "Wavefront dislocations: topological limitations for adaptive systems with phase conjugation," J. Opt. Soc. Am. – 1983. – A **73**. – P. 525-528.

[8]. H. He, N.R. Heckenberg, and Rubinsztein-Dunlop, "Optical particle trapping with higher-order doughnut beams produced using high efficiency computer generated holograms," J. Mod. Opt. **42** (1), 217-223 (1995).

[9]. N.B. Simpson, J.L. Allen, and M.J. Padgett, "Optical tweezers and optical spanners with Laguerre-Gaussian modes," J. Mod. Opt. **43** (12), 2485-2491 (1996).

[10]. M. Mujat and A. Dogariu, "Polarimetric and Spectral changes in Random Electromagnetic Fields," Opt. Lett., **28** (22), 2153-2155 (2003).

[11]. G. Popescu and A. Dogariu, "Spectral anomalies at wave-front dislocations," Phys. Rev. Lett. **88**, 183902 (2002).

[12]. V.K. Polyanskii, O.V. Angelsky, and P.V. Polyanskii, "Scattering-induced spectral changes as a singular optical effect," Optica Applicata. – 2003. – Vol.**32**. – No.4. – P. 843-848.

[13]. J.F. Nye, "From Airy rings to the elliptic umbilic diffraction catastrophe," J. Opt. A: Pure Appl. Opt. **5**, 503-510 (2003).

J.F. Nye, D.R. Haws and R.A. Smith, "Use of diffraction gratings with curved lines to study the optical catastrophes D_6^+ and D_6^-," Journal of Modern Optics **34**, 407-427 (1987).

[14]. J.F. Nye, “Evolution from a Fraunhofer to a Pearcey diffraction pattern,” J. Opt. A: Pure Appl. Opt. **5**, 495-502 (2003).
[15]. O.V. Angelsky, D.N. Burkovets, P.P. Maksimyak and S.G. Hanson, “Applicability of the singular-optics concept for diagnostics of random and fractal rough surfaces,” Appl. Opt. **42**, 4529-4540 (2003).
[16]. A. Apostol and A. Dogariu “Coherence properties of Optical Near Fields,” Optics and Photonics News, V.**14**, #12, 22 (2003).
[17]. H.F. Schouten, T.D. Visser, G. Gbur, D. Lenstra, and H. Blok, “Phase singularities and Enhanced Transmission at a Subwavelength slit,” Optics and Photonics News, V.**14**, #12, 23 (2003).
[18]. S.M. Rytov, Ju.A. Kravtsov, and V.I. Tatarsky, *Principles of Statistical Radiophysics* (Springer-Verlag, Berlin 1989).
[19]. O.V. Angelsky, S.G. Hanson, and P.P. Maksimyak, *Use of Optical Correlation Techniques for Characterizing Scattering Objects and Media*, Vol. PM71 of SPIE Press Monograph Series (SPIE Press, Bellingham, Wash., 1999).
[20]. O.V. Angelsky, P.P. Maksimyak, V.V. Ryukhtin, and S.G. Hanson, “New feasibilities for characterizing rough surfaces by optical-correlation techniques,” Appl. Opt. **40**, 5693-5707 (2001).

Poster Session

WE

Monday, August 16	10:20–10:40
	12:20–13:50
	15:10–15:30
Tuesday, August 17	10:50–11:10
	12:50–13:30
Wednesday, August 18	10:20–10:40
	11:40–13:30
	14:30–14:50

Tinbergen Room

Estimation of Optical-Geometrical Parameters of Nonspherical Particles in Polarized Light

L.I. Podkamen, A.D. Arkhelyuk, and O.O. Arkhelyuk
Department of Correlation Optics; Chernivtsi National University, 2 Kotsyubinsky Str., 58012 Chernivtsi, Ukraine
arkhelyuk@itf.cv.ukrtel.net

Abstract

The experimental investigation results of the influence of the shape, size and orientation degree of nonspherical particles of the model pattern on the change regularities of normalized components of scattering and extinction matrixes are presented. The component of light field and experimental situations which are most advisable for the estimation of particles optical-geometrical parameters is obtained.

Change regularities of the energetic and polarizing characteristics of the light crossed through the light beam depending on its optical-geometrical parameters can be fully described using the vector-parametrical principle of light beams and their linear transformation as a matrix:

$$S_i(\lambda,\varphi) = \frac{1}{R^2}\sum_{k=1}^{4} F_{ik}(\lambda,\varphi) S_k(\lambda) V(\varphi)$$

where $i = 1, 2, 3, 4$; F_{ik} – matrix of first rang, which characterizes the media properties; S_i и S_k – Stocks parameters of scattered and crossing beams accordingly; λ – wavelength; φ – scattering angle; $V(\varphi)$ – the value of photometrical particle of the scattering volume and R – distance from the scattering volume centre to observation point.

As a model system of nonspherical particles of the specified form and different size were used optically thin layers of nondeveloped photoemulsion no. 1–3 which contain $AgBr$ crystals with octahedron form and size parameters, given in table1:

Table 1

No.	$\overline{\alpha}$	σ	c_V
1	0,5	0,137	27%
2	1,2	0,412	35,2%
3	3,0	1,36	46%

In table 1 $\overline{\alpha} = \dfrac{\sum d \cdot n}{\sum n}$ is the average diameter of particles, where n – number of particles with diameter d, σ – average square declination, $c_V = \dfrac{\sigma}{\overline{\alpha}} \cdot 100\%$ – relative dispersion.

The refraction index of $AgBr$ particles is equivalent to 1.5 concerning to gelatin using radiation with $\lambda = 0.633\ \mu m$.

The analysis of experimentally defined regularities of angle cross of normalized nonzero $f_{ik} = F_{ik} / F_{11}$ components of scattering matrix showed that:

1. f_{22} component, which for the spherical particles system is equivalent to 1 in all range of scattering angles φ, has the identical value of its minimum $f_{22}^{\min} \approx 0.62$ in all three model patterns at scattering angles $\varphi \approx 100^\circ$. Obviously that the main parameter which determines the declination of research particles from spherical is the maximum value $\Delta = 1 - f_{22}^{\min}$.

2. The determination of particles size is more advisable as a value of scattering angle φ at which f_{33} component is

equivalent to 0. With the increase of particles diameter scattering angle displaces to the larger values. In our case for the particles with $\overline{d}_1 = 0.5\ \mu m$ is $\varphi_1 = 98^\circ$, and for the particles with $\overline{d}_2 = 3.0\ \mu m$ is $\varphi_2 = 122^\circ$.

On the basis of obtained functional dependencies $f_{ik} = f(\lambda)$ we can determine polarization characteristics of light field of model patterns using the following quantities:

$$p_j = \pm \frac{\sqrt{(f_{21} \pm f_{2j})^2 + (f_{31} \pm f_{3j})^2}}{1 + f_{1j}} \tag{2}$$

$$g_j = \frac{f_{41} \pm f_{4j}}{1 + f_{1j}} \tag{3}$$

$$r_j = \frac{\sqrt{(f_{21} \pm f_{2j})^2 + (f_{31} + f_{3j})^2 + (f_{41} + f_{4j})^2}}{1 \pm f_{1j}} \tag{4}$$

where p_j, g_j, r_j – degree of polarization, ellipticity and degree of scattered light heterogeneity accordingly; ($\pm$) marks relate to appropriate irradiating beams $c \pm S_j$, where $j = 2, 3, 4$.

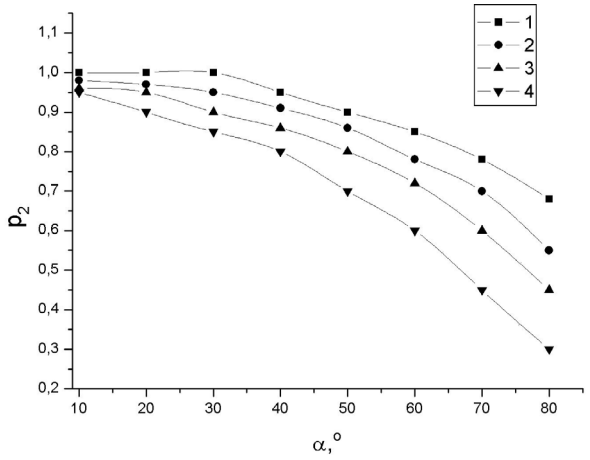

Fig. 2. Dependencies of p_2 and g_4 from α for photolayers:
1 – p_2 at $d = 0.5\ \mu m$; 2 – g_4 at $d = 0.5\ \mu m$;
3 – p_2 at $d = 3\ \mu m$; 4 – g_4 at $d = 3\ \mu m$

Experimentally determined dependencies of p_2 and g_4 of scattered radiation for two nonspherical particles systems with $\overline{d}_1 = 0.5\ \mu m$ and $\overline{d}_2 = 3.0\ \mu m$ are presented on the fig.1 (curves 1, 2 and curves 3, 4 accordingly).

According to fig. 1 the increase of particles size is accompanied by the consecutive decrease of p_2 and g_4 at the same scattering angle φ. Besides, for the layer which contains larger particles (curves 3, 4) are marked more sharp differences between p_2 and g_4 in comparison with analogical differences at the scattering on the particles with $\overline{d}_1 = 0.5\ \mu m$ (curves 1, 2). Thus, the increase of nonspherical particles size in the media results in the lesser stability with the increase of scattering angle of light beams which are polarized elliptically. If the polarization degree p_2 slightly changes during the increase of size parameter of nonspherical particles then g_4 (ellipticity of the scattered light at the circularly polarized irradiating beam) decreases in two times on the particles with $d \approx 3.0\ \mu m$ concerning to g_4 for particles with $d \approx 0.5\ \mu m$ ($\alpha = 80^\circ$).

Theoretically p_2 and g_4, calculated by (2), (3) at different scattering angle φ coincide with experimentally defined values with error less than 10%.

For the estimation of presence and orientation degree of nonspherical particles dispersion system the investigation results of extinction matrix of the model layer of $\gamma - Fe_2O_3$ particles which are oriented in the magnetic field of specified tension and fixed on the thin optical glass by epoxy [2] are used. The Stokes-parameters of radiation crossed through the model layer is defined by [3]:

$$\overline{S}_i = \left[\overline{F}_1 - \varepsilon_{ij}(z)dz\right] \cdot \overline{S}_j \qquad (*)$$

where $\overline{S}_i$, $\overline{S}_j$ – Stokes vectors of the radiation crossing and falling on the dz layer of radiation accordingly; $\overline{F}_1$ – single 4×4 matrix; $\overline{\varepsilon}_{ij}(z)$ – extinction matrix.

For the optically thin media at such condition

$$\varepsilon_{ii}(z - z_0) << 1 \qquad (5)$$

regularity (*) looks like:

$$\overline{S}_i(z) = \left[\overline{F}_1 - (z - z_0)\overline{\varepsilon}_{ij}\right] \cdot \overline{S}_j \qquad (6)$$

The investigation of the influence of the orientation degree $\gamma - Fe_2O_3$ particles of the model patterns shows the presence of essential dependence of f_{ij} components of extinction matrix $\overline{\varepsilon}_{ij}(z)$ from B and from the angle θ of the particles primary orientation concerning to the fixed referention plane position. Only one f_{44} component doesn't depends on θ and is defined by B. f_{44} values at different B of model layers are given in table 2.

Table 2.

B	0,018	0,056	0,378	0,57	0,69	0,79	0,86	0,998
f_{44}	1	0,99	0,91	0,80	0,72	0,68	0,49	0

On the basis of table 2 on the fig. 2 we can show the functional dependence $f_{44} = f(B)$ using such equation:

$$B = \sqrt{1 - f_{44}^2} \qquad (7)$$

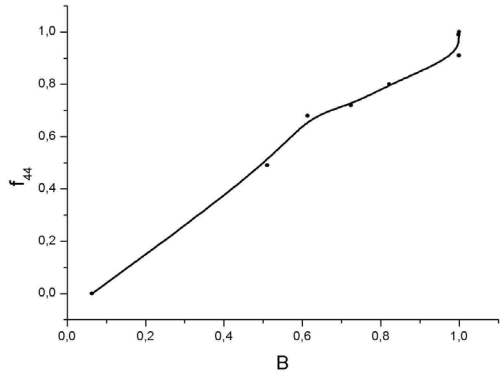

Fig. 2. $f_{44} = f(B)$ dependence.

Thus, investigation results of Mueller matrixes of nonspherical particles systems and of the polarization characteristics of scattered beams which are presented in this work can be used for the estimation of the form, size and orientation degree of particles systems.

References

[1] A.P. Ivanov, Scattering and absorption of light in natural and artificial dispersion mediums (Minsk, 1991).

[2] L.I. Podkamen, M.L. Kirsh, O.V. Pishak, P.M. Grygoryshyn, "Polarization investigation of biological objects and form elements of blood," in Success of modern biology, Vol. 119, No.2, 190-196 (1999).

[3] B.V. Kaul, D.N. Romanov, "Estimation of the influence of cylindrical ice particles on the extinction matrix," in Journ. of Opt. of Atm. and Ocean, Vol. 10, No.12, 1485 (1997).

A PCS Study of Correlations and Fluctuations in the Laser Speckle Pattern

Sándor Balog,[1] Juan José Sáenz,[2] and Frank Scheffold[1]
[1]Physics Department, University of Fribourg, CH-1700 Fribourg, Switzerland
[2]Departamento de Física de la Materia Condensada, Universidad Autónoma de Madrid, E-28049 Madrid, Spain
Sandor.Balog@unifr.ch

Abstract: Fluctuations and Correlations in the transmission speckle pattern are analyzed with PCS for the case of finite sized random media.

1. Introduction

Laser light scattered from a disordered medium shows the typical granularity intensity pattern called speckle. In the classical picture the scattered optical fields are randomly distributed so that the speckle spots are uncorrelated and the intensity distribution obeys so called Rayleigh-statistics $P(I) = I/\langle I\rangle \exp\left(-I/\langle I\rangle\right)$ [1].

In this picture the spatially averaged transmitted intensity $\langle I\rangle$ is constant in both solid and liquid samples, therefore independent of the system configuration. However if the scattering is strong and the scattering volume is laterally confined long-range correlations between speckles build up and $\langle I\rangle$ fluctuates as the system configuration or the optical wavelength changes. In a more formal way the scattering of coherent waves can be described by transmission coefficients T_{ab} where the incident light mode is labeled a and the scattered light mode b. Hence $\langle I\rangle \equiv I_0 \sum_b T_{ab}$ for an incident laser intensity I_0. In their pioneering work Feng et al. [2] calculated the correlation function of the transmission coefficients $C_{aba'b'} \equiv \langle \delta T_{ab} \delta T_{a'b'} \rangle$ using diagrammatic techniques.

$$C_{aba'b'} = C^{(1)}_{aba'b'} + C^{(3)}_{aba'b'} + C^{(3)}_{aba'b'} \tag{1}$$

Eq. 1 has stimulated many experimental and theoretical studies both in optics and electronics. Particular interest has been raised by the fact that high order correlations are closely linked to universal conductance fluctuation (CUFF) and transport properties of electrons in macroscopic wires [3].

In a light scattering experiment $C_{aba'b'}$ can be measured directly as sketched in Fig. 1 by collecting data from different samples or equivalently by variation of a phase shift introducing parameter such as the laser wavelength [4], a magnetic field for Faraday active media [5] or time in the case of a liquid sample. In particular for the last case photon correlation spectroscopy is used as an extremely powerful tool as shown in ref. [6].

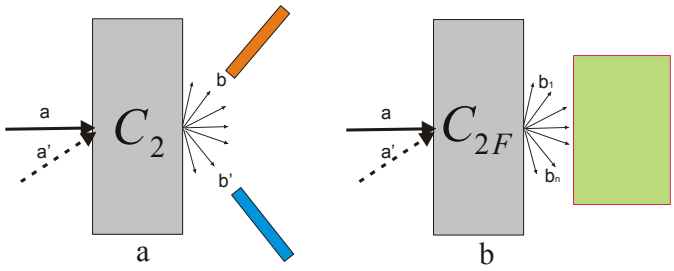

Fig. 1. Representation of an optical experiment where laser light is transmitted through a disordered slab. Incident wave modes are denoted a, a' and the scattered modes b, b'. For C_2 $a = a'$ such that a) Cross correlating the intensity scattered to b and b' yields information about speckle correlations, b) Analyzing the angular-averaged intensity as a functions of sample configuration provides information about transmittance fluctuations.

The amplitudes of the different contributions were found to scale with the Landauer dimensionless conductance $g \equiv \sum_{a,b} T_{a,b}$ [7-9].

$$C_{aba'b'} = C_1 \delta_{aa'} \delta_{bb'} + \frac{2}{3g} C_2 (\delta_{aa'} + \delta_{bb'}) + \frac{2}{15g^2} C_3 \tag{2}$$

Depending on the transport process considered different contributions are dominant, C_1 is the dominant term when $a = a'$ and $b = b'$, C_2 dominates when $a = a'$ and $b \neq b'$, finally C_3 dominates when $a \neq a'$ and $b \neq b'$.

2. Correlations and Fluctuations

Deep in the diffusive regime ($1 \ll g \ll N$) correlations and fluctuations are closely related. For example the intensity fluctuations C_{2F} of the transmittance T_a are given as follow: $C_{2F} \equiv \mathrm{var}\{T_a\} / \langle T_a \rangle^2 \approx 2/3g \approx C_2$. Although physically different it was frequently concluded that correlations C_2 and fluctuations C_{2F} are equivalent. However recently is has been shown that important differences appear when the size of the random medium is finite [10]. In optics this interesting regime extends from a distance L comparable to the transport mean free path l^* up to the limit of diffuse transport $L \gg l^*$. For finite but still fully random media ($L < 10l^*$) the physics of correlation and fluctuations are then found pronouncedly different. Ref. [10] gives a detailed theoretical account of both correlations (C_2, C_3) and fluctuations in finite sized random media. For waveguides the following relations have been found (with $g = N/(1+s)$, $N = 1/(8k^2\omega^2)$, $k \equiv 2\pi n/\lambda$ and $s \equiv 3L/4l^*$)

$$C_{2F} \cong \frac{s^2}{g(1+s)^3}\left(\frac{2}{3}s+1\right) \tag{3}$$

$$C_2 \cong \frac{2}{3g}\frac{1}{(1+s)^3}\left(s^3-3s-\frac{3}{2}\right) \tag{4}$$

However the theoretical assumption of waveguide geometries is usually not realized in optical experiments and typically a beam of width ω with Gaussian profile is impinged on a sample. In this case the beam waist is defined by the distance between the e^{-1} points of the transverse intensity distribution at the sample surface

$$I(r) = \frac{2}{\omega^2\sqrt{\pi}}\exp\left(\frac{-4r^2}{\omega^2}\right) \tag{5}$$

The width of the beam strongly influences the amplitude of C_{2F} since the photon cloud broadens on its way through the sample. If the sample is large ($\omega \ll L$) only a region of the order of the beam size really contributes to C_{2F}. It was found both theoretically and experimentally that in the diffusive regime C_{2F}^{-1} increases linearly with the incident beam spot width and does not depend on the sample thickness L [11].

$$\frac{1}{C_{2F}} = \frac{8}{15}k^2 l^* \omega \tag{6}$$

Comparison of Eqs. (4) and (7) and in turn defines an effective layer thickness L_{eff} where the scattering volume is small and contributions to C_{2F} are built up [10].

$$L_{eff} = \frac{3}{10}\omega \tag{7}$$

This maps the problem of a Gaussian beam profile to the case of a waveguide with identical C_{2F}. We note that in the diffusive regime the existence of such typical length scales has been indeed observed in experiment [12].

We make the ad-hoc assumption that this scaling argument still holds for $\omega \approx l^*$. From Eq. (8) and Eq.(4) we can then derive an approximate expression for C_{2F} covering the full range of length scales ($\omega \approx l^* \rightarrow \omega \gg l^*$).

$$\frac{1}{C_{2F}} \cong \frac{200}{81}\left(k \cdot l^*\right)^2 \frac{\left(1+\frac{9\omega}{40l^*}\right)^2}{1+\frac{3\omega}{20l^*}} \tag{8}$$

This relation can be directly compared to optical experiments (Fig. 1-b). From measurements of the correlation function of the total transmitted intensity C_{2F}^{-1} has been determined as a function of the incident beam width (as previously described in [6]), Fig. (2).

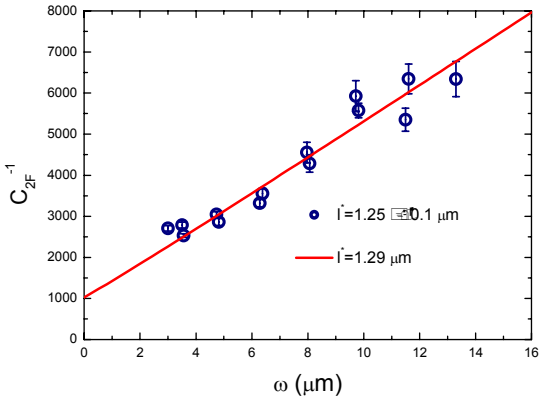

Fig. 2. The inverse amplitude C_{2F}^{-1} for fluctuation of the transmitted intensity for highly focused Gaussian laser beam and a sample thickness of $L \approx 500\mu m$. The sample used is a suspension ($\approx 9\%$,volume fraction) of commercially available TiO_2 particles in water ($n = 1.33$). The solid line is calculated from Eq. (10) with l^* the only adjustable parameter. The independently determined value of l^* is given in the legend (symbol). The data has been obtained as described in Ref. [6]. Note that the measured C_{2F} has been multiplied by a factor 2.2 to account for total internal reflection [6].

3. Conclusions and Outlook

The results shown in Figure 2 compare well with previous measurements (ref. [6]). Furthermore using the new Eq.(9) we are now able to quantitatively describe the data even for $\omega \to l^*$. Using PCS as a powerful tool we thus obtain a sound picture how fluctuation properties of transmitted laser light change dramatically if the sample size is finite.

Measurements are currently underway to access for the first time directly C_2 and to elaborate the important differences we expect between correlations and fluctuations in random wave transport.

4. Acknowledgment

Fruitful discussions with Georg Maret and Antonio Gracia-Martin are gratefully acknowledged.

5. References

[1] J. W. Goodman, *Statistical Properties of Laser Speckle Patterns*, in Laser Speckle and Related Phenomena, J. C. Dainty, Editor. Springer-Verlag, New York Tokio, 1984.
[2] S. Feng, C. Kane, P. A. Lee and A. D. Stone, *Correlations and Fluctuations of Coherent Wave Transmission through Disordered Media*, Physical Review Letters 61 (7), 834 (1988).
[3] F. Scheffold and G. Maret, *Universal Conductance Fluctuations of Light*, Physical Review Letters 81 (26), 5800 (1998).
[4] M. P. V. Albada, J. F. D. Boer and A. Lagendijk, *Observation of Long-Range Correlation in the Transport of Coherent Light Random Medium*, Physical Review Letters 64 (23), 2787 (1990).
[5] F. A. Erbacher, R. Lenke and G. Maret, *Multiple Light Scattering in Magneto-Optically Active Media*, Europhysics Letters 21, 551 (1993).
[6] F. Scheffold, W. Härtl, G. Maret and E. Matijevic, *Observation of long-range correlations in temporal intensity fluctuations of light*, Physical Review B 56 (17), 10942 (1997).
[7] P. A. Mello and A. D. Stone, *Maximum-entropy model for quantum-mechanical interference effects in metallic conductors*, Physical Review B 44 (8), 3559 (1991).
[8] P. S. (Ed.), *Waves and Imaging through Complex Media*. Kluwer Academic Publisher, Dordrecht, 1999.
[9] P. A. Mello, E. Akkermans and B. Shapiro, *Macroscopic Approach to Correlations in the Electronic Transmission and Reflection from Disordered Conductors*, Physical Review Letters 61 (4), 459 (1988).
[10] A. Garcia-Martin, F. Scheffold, M. N. Vesperinas and J. J. Sáenz, *Finite-Size Effects on Intensity Correlations in Random Media*, Physical Review Letters 88 (14), 143901 (2002).
[11] R. Pnini and B. Shapiro, *Fluctuations in transmission of waves through disordered slabs*, Physical Review B 39 (10), 6986 (1989).
[12] F. Scheffold and G. Maret, *pages 413 - 434 in ref. [8]*.

Measurement of the Dispersity of Multicomponent Mixtures of Monodisperse Latexes by the Dynamic Light Scattering Method

M. S. Dioujeva and V. V. Klyubin
St. Petersburg State Marine Technical University, ul. Lotsmanskaya 3, St. Petersburg 190008 Russia

At present, the methods of optical and electron microscopy, sedimentation, measuring of light scattering indicatrix, dynamic light scattering (DLS), etc., are used to determine the sizes of micron and submicron particles [1-3]. All aforementioned methods have their advantages and disadvantages. This work deals with the study of the potentialities of dynamic light scattering method for measuring the sizes of colloidal particles in samples characterized by wide distributions and consisting of several narrow-disperse components (fractions). An attempt was made to analyze the errors encountered in such measurements.

This study continues a series of works devoted to the analysis of the potentialities of a mathematical apparatus used to process experimental data of the DLS method. Concepts underlying the software packages used for processing the autocorrelation function of fluctuations in the current induced by a scattered light in a photodetector were described in the first work of this series [4]. In the same work, the authors analyzed the influence of errors in registering the correlation function on the optimal value of the regularization parameter used for the restoration of the particle size distribution. In the second work [5], the CONTIN [6] and KLUB [4] software packages used for processing experimental data were compared.

It is known that the DLS method makes it possible to measure with a sufficient accuracy the average sizes of narrow-disperse colloids [7]; however, in the case of mixtures of such samples, the situation is somewhat complicated. The matter is that, during DLS measurements, the analyzed signal is the scattered light intensity, which, for small particles, greatly depends on their sizes. For samples whose particle sizes are different by at least an order of magnitude, the contribution of small particles to the total scattering can be lost because of photodetector noises [8]. In addition, distortions relevant to the mathematical processing of the obtained information are inherent in the DLS method. The distributions resulted from the solution of the inverse problem by the regularization method appear to always be wider than real distributions. In the long run, a measured particle size distribution always differs from a real distribution. In order to analyze the distortions inherent in the DLS method, we used several colloidal dispersions with known distributions (a set of monodisperse latexes) and their mixtures in different combinations. This work consists of two parts: the experimental measurement of the dispersity of real colloids and computer-assisted calculations, which made it possible to compare the measured distributions with the actual ones and to determine the character of distortions arising in such measurements.

Experimental data were processed using the CONTIN and KLUB software packages. The measurements were performed with a "Coulter N4" instrument (Coultronics, France) operating as a correlator of the dynamic light scattering. Dispersities of all samples were measured by the DLS and electron microscopy methods (with a Tesla 245 transmission electron microscope). The mean particle sizes measured by the electron microscopy and DLS methods are in quite good

agreement. Measurements of parameters of the initial monodisperse latexes are necessary to calculate the dispersities of the samples prepared by mixing several such latexes. Two- and three-component mixtures of different latexes were studied. For the preparation of mixed samples, initial latexes were diluted to concentrations at which the intensities of the light scattered at 90o were equal for all dispersions. Then, equal volumes of diluted latexes were poured into one cell, thus obtaining mixtures of monodisperse latexes in different combinations. Distributions of scattered light intensities over the particle sizes for single latexes and their mixtures were calculated using particle size distributions measured with the electron microscope. Then, corresponding mass distributions were calculated from the intensity distributions of the mixtures. "Ideal" distributions were thus obtained, and actually measured distributions were compared with them.

Processing of the correlation functions using the CONTIN and KLUB software packages yielded close results, except for the cases, when the CONTIN package yielded false components in the region of small sizes. This peculiarity of the CONTIN software package to yield false peaks was observed earlier [5, 9]. The analysis demonstrates that the software packages used to process the correlation function of the scattered light cannot resolve single components of particle mixture whose sizes are different by less than two times. Note that the resolution of the DLS method depends not only on the ratio between particle sizes of single fractions, but also on the absolute particle sizes of these fractions and the concentration ratio of particles with different sizes. For the region of Rayleigh particles with diameters smaller than 200 nm, under optimal conditions, it is possible to resolve components of a bimodal distribution, even when the diameter ratio is only slightly larger than two. Closely located components can be resolved, when their particle sizes are different by at least three times.

Measurements of a mixture of three latexes with the ratio between the mean particle sizes equal to 1 : 2 : 4, in practice did not yield the data on the pattern of the particle size distribution. All three mixture components are merged into one component in the restored distribution.

As the performed study demonstrated, the restoration of the distributions consisting of a large number of narrow components is quite difficult task. Actually, this problem can be solved for a bimodal distribution, when the particle sizes of two fractions are different by at least three times.

References

1. Collins, E.A., Davidson, J.A., and Damiels, C.A., J. Paint Technol., 1975, vol. 47, p. 35.
2. Ruska, E., Usp. Fiz. Nauk, 1988, vol. 154, no. 2, p. 243.
3. Shifrin, K.S., Light Scattering in Turbid Media, Moscow: GITTL, 1951.
4. Klyubin, V.V. and Tumanova, S.A., Kolloidn. Zh., 1995, vol. 57, no. 3, p. 354.
5. Bungov, V.N. and Klyubin, V.V., Kolloidn. Zh., 2000, vol. 62, no. 2, p. 218.
6. Provencher, S.W., J. Chem. Phys., 1976, vol. 64, no. 7, p. 2772.
7. Klyubin, V.V., Kruglova, L.A., Sakharova, N.A., and Tallier, Yu.A., Kolloidn. Zh., 1990, vol. 52, no. 3, p. 470.
8. Klyubin, V.V., Kruglova, L.A., and Sokolov, V.N., Kolloidn. Zh., 1990, vol. 52, no. 2, p. 358.
9. Bashirova, V.S., Kamkha, M.A., Pusep, A.Yu., and Fedorenko, S.G., Kolloidn. Zh., 1993, vol. 55, no. 1, p. 10.

The Investigation of Chaos in the Field of Optical Radiation Scattered by Liquid Crystals

M.S. Gavrylyak, V.S. Lomanets and P.P. Maksimyak
Correlation Optics Department, Chernivtsi University, 2 Kotsyubinsky Str., Chernivtsi, 58012 Ukraine
pmaksimyak@itf.cv.ukrtel.net

Abstract: This paper represents the results of investigating chaos in the field of optical radiation scattered by nematic liquid crystal during phase transition liquid – liquid crystal and liquid crystal – liquid. It has been shown that Lyapunov's maxim index of time intensity dependency is greater than zero, i.e. there is some chaos in the system.

They often use phase transition liquid – liquid crystal or liquid crystal – liquid in the technology taking into account the fact that optical substance properties change during transition process. This process is limited in time and it belongs to the class of transition processes, which are described by the theory of chaotic and stochastic oscillations. Therefore, the investigation of this process is considered to be urgent [1].

We have researched chaos in the field of optical radiation scattered by nematic liquid crystal during phase transition liquid – liquid crystal and liquid crystal – liquid. We have used Lyapunov's maxim index of time intensity dependency of scattered radiation field. The positive value of Lyapunov's maxim index proves the probability of chaos availability in the system, and this index value characterizes the degree of randomicity [2].

Lyapunov's indices characterize the average speed of exponential divergence of close phase trajectories. If d_0 is the initial distance between two initial dots of phase trajectories, the distance between trajectories outgoing from these dots at time t will be the following one:

$$d(t) = d_0 e^{\lambda t}. \quad (1)$$

The value λ is called as Lyapunov's index. Each dynamic system is characterized by the spectrum of Lyapunov's indices λ_i (i=1,2,…,n),, where n – differential equations' quantity, which are necessary for describing the system. The availability of the positive value of Lyapunov's index can be the proof of chaos existence in the system when having the experimental data obtained during the investigation of dynamic systems. In general, the chaotic system is characterized by the divergence of phase trajectories at some directions and their convergence at others. It means that there are either positive or negative Lyapunov's indices in the chaotic system.

For calculating Lyapunov's maxim index and using theoretical conclusion in paper [3] there has been elaborated the algorithm and program of calculating Lyapunov's maxim index. This algorithm has been used as the basis for making the program having used the language Delphi. The modeled signal – Xenon's reflection has been used for testing this program. We gained the value λ_1, which nearly coincides with the theoretical one λ_1.

Liquid crystal N28 was used as the investigation object, which was placed into a specially designed plate of changeable thickness. Phase transition in the crystal was gained due to temperature change of liquid crystal.

Fig. 1 represents time intensity distribution of radiation field scattered at the angle of 6 degree in the plate of 50 mcm thickness.

Fig. 2 demonstrates the dependency of calculated Lyapunov's indices of phase transition process liquid – liquid crystal on thickness. Lyapunov's index is positive for all thickness sizes.

Thus, the scattering of optical radiation by nematic liquid crystal during phase transition liquid – liquid crystal is of the chaotic character. Moreover, the degree of randomicity increases with the growth of plate thickness of liquid crystal.

References

1. De Jene, P.J., Physics of Liquid Crystals. Ed. By Sosnin A.S. – Moscow: Mir, (1977) (in Russian).
2. Neumark, Yu. I., and Landa, P.S., Stochastic and Chaotic Oscillations. Moscow, Nauka, (1987) (in Russian).
3. Rosenstein M.T., Collins J.J., and Luca Carlo J. De. *A practical method for calculating largest Lyapunov exponents from small data sets* (MA 02215, Boston University, 1992).

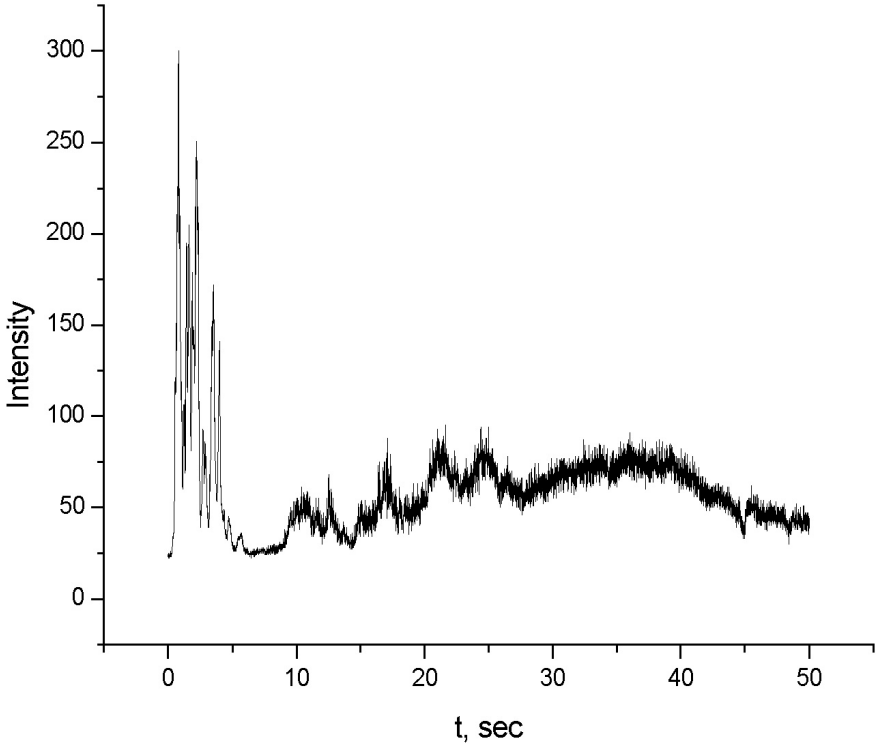
Intensity
300
250
200
150
100
50
0
0
10
20
30
40
50
t, sec

Fig. 1

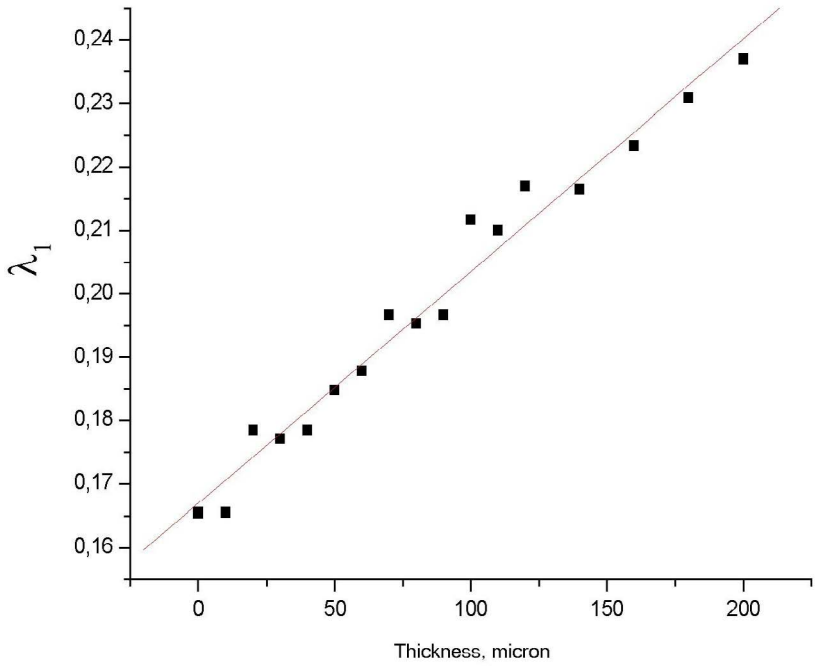
λ_1
0,24
0,23
0,22
0,21
0,20
0,19
0,18
0,17
0,16
0
50
100
150
200
Thickness, micron

Fig. 2

ESA Research Announcement of Opportunity in Life and Physical Sciences

Frank Molster
ESTEC/ESA, Keplerlaan 1, 2201 AZ Noordwijk, The Netherlands
e-mail address: frank.molster@esa.int

Abstract: ESA will announce a new research opportunity in the areas of Life and Physical Sciences. In the area of physical Sciences, Research projects for the full range of Physical Sciences with relation to the absence of gravity are invited for submission. The deadline for submission will be the 30-th of September 2004. More information can be found at http://www.spaceflight.esa.int/users/file.cfm?filename=coord-ao-lra

Author Index

REPORT DOCUMENTATION PAGE

Form Approved
OMB No. 0704-0188

1. AGENCY USE ONLY (*Leave blank*)	2. REPORT DATE	3. REPORT TYPE AND DATES COVERED
	August 2004	Conference Publication

4. TITLE AND SUBTITLE

2004 Photon Correlation and Scattering Conference

5. FUNDING NUMBERS

WBS–22–101–58–09

6. AUTHOR(S)

William Meyer, Anthony Smart, Gerard Wegdam, Aristide Dogariu, and Bradley Carpenter, editors

7. PERFORMING ORGANIZATION NAME(S) AND ADDRESS(ES)

National Aeronautics and Space Administration
John H. Glenn Research Center at Lewis Field
Cleveland, Ohio 44135–3191

8. PERFORMING ORGANIZATION REPORT NUMBER

E–14715

9. SPONSORING/MONITORING AGENCY NAME(S) AND ADDRESS(ES)

National Aeronautics and Space Administration
Washington, DC 20546–0001

10. SPONSORING/MONITORING AGENCY REPORT NUMBER

NASA CP—2004-213207

11. SUPPLEMENTARY NOTES

Proceedings of the 2004 Photon Correlation and Scattering Conference cosponsored by ESA, OSA, NASA Glenn Research Center, NCMR, the University of Amsterdam, and the Van der Waals-Zeeman Institute, Amsterdam, The Netherlands, August 16–18, 2004. Responsible person, Bhim Singh, organization code 6712, 216–433–5396.

12a. DISTRIBUTION/AVAILABILITY STATEMENT

Unclassified - Unlimited
Subject Categories: 35, 23, 74, and 34 Distribution: Nonstandard

Available electronically at http://gltrs.grc.nasa.gov

This publication is available from the NASA Center for AeroSpace Information, 301–621–0390.

12b. DISTRIBUTION CODE

13. ABSTRACT ***(Maximum 200 words)***

The Photon Correlation and Scattering (PCS) meeting welcomes all who are interested in the art and science of photon correlation and its application to optical scattering. The meeting is intended to enhance interactions between theory, applications, instrument design, and participants.

14. SUBJECT TERMS

Photon correlation spectroscopy; Scattering; Light scattering; Surface scattering; Multiple scattering; Diffusing wave spectroscopy; Near field scattering; Particle sizing; Photonic materials; Complex fluids; Biophotonics; PCS; DWS

15. NUMBER OF PAGES

123

16. PRICE CODE

17. SECURITY CLASSIFICATION OF REPORT	18. SECURITY CLASSIFICATION OF THIS PAGE	19. SECURITY CLASSIFICATION OF ABSTRACT	20. LIMITATION OF ABSTRACT
Unclassified	Unclassified	Unclassified	